THESIS ON MECHANICAL ENGINEERING E112

Chemical Vapour Deposition of Graphene Coating onto Ceramic Nanofibers Substrates and Applications Thereof

ROMAN IVANOV

TTÜ
PRESS

TALLINN UNIVERSITY OF TECHNOLOGY
SCHOOL OF ENGINEERING
Department of Mechanical and Industrial Engineering

This dissertation was accepted for the defence of the degree of Doctor of Philosophy in Engineering on November 10, 2017.

Supervisor: Prof. Irina Hussainova
School of Engineering, Department of Mechanical and Industrial Engineering, Tallinn University of Technology.

Opponents: Dmitrii Semenenko
Vice president, Science and Innovation Development, R&D Institute of Carbon Materials, Roselectronics.
Research associate, Materials Science Department, Moscow State University.

Dr. Kaupo Kukli
Research Professor, Institute of Physics, University of Tartu.

Defence of the thesis: December 12, 2017, at 12:00, Tallinn University of Technology, room U05-216.

Declaration:
Hereby I declare that this doctoral thesis, my original investigation and achievement, submitted for the doctoral degree at Tallinn University of Technology has not been submitted for doctoral or equivalent academic degree.

European Union
European Regional
Development Fund

Investing
in your future

ISSN 1406-4758
ISBN 978-9949-83-187-6 (publication)
ISBN 978-9949-83-188-3 (PDF)

MEHHANOTEHNIKA E112

Grafeenpinde keemiline aursadestus keraamilistele nanokiududele ja nende kasutus

ROMAN IVANOV

TTÜ KIRJASTUS

TABLE OF CONTENTS

LIST OF PUBLICATIONS

The work of this thesis is based on the following publications, which are referred in the text by the Roman numerals I–V:

I **Ivanov, R.**, Mikli, V., Kübarsepp, J., Hussainova, I., Direct CVD growth of foliated graphene closed shells on alumina nanofibers. — *Key Engineering Materials*, 2016, 674, 77–80, doi:10.4028/www.scientific.net/KEM.674.77

II Hussainova, I., **Ivanov, R.**, Stamatin, S.N., Anoshkin, I.V., Skou, E.M., Nasibulin, A.G., A few-layered graphene on alumina nanofibers for electrochemical energy conversion. — *Carbon*, 2015, 88, 157–164, doi:10.1016/j.carbon.2015.03.004

III Stamatin, S. N., Hussainova, I., **Ivanov, R.**, Colavita, P. E., Quantifying graphitic edge exposure in graphene based materials and its role in oxygen reduction reactions. — *ACS Catalysis*, 2016, 6, 5215–5221, doi:10.1021/acscatal.6b00945

IV **Ivanov, R.**, Hussainova, I., Aghayan, M., Drozdova, M., Pérez-Coll, D., Rodríguez, M. A., Rubio-Marcosc, F., Graphene-encapsulated Aluminium Oxide Nanofibers as a Novel Type of Nanofillers for Electroconductive Ceramics. — *Journal of the European Ceramic Society*, 2015, 35(14), 4017–4021, doi:10.1016/j.jeurceramsoc.2015.06.011

V Kazantseva, J., **Ivanov, R.**, Gasik, M., Neuman, T., Hussainova, I., Graphene-augmented nanofiber scaffolds demonstrate new features in cells behaviour. — *Scientific Reports*, 2016, 6, 30150, doi:10.1038/srep30150

AUTHOR'S CONTRIBUTIONS TO THE PUBLICATIONS

Contribution to the papers:

I	Design of the CVD set-up; Deposition of the graphene coatings onto a network of ceramic nanofibers being under consideration; Thorough characterization of the produced materials; Analysing the results; Drafting the manuscript.
II	Design the CVD procedure; Optimization of the process parameters; Making experiments on controlled carbon deposition; Spectroscopy; Results analysing; Drafting the manuscript.
III	Performing parametric tests on the CVD process; Deposition of the designed amount of graphene layers onto the substrate; Characterization of the materials; Analysis of the results.
IV	Preparation and analysing of the graphenated nano-fillers; Spectroscopy; Tests on dispersion of the fillers; Analysis of the results.
V	Design and producing of bio-scaffolds; Fluorescent microscopy; Tests on biocompatibility; Analysis of the results; Drafting the manuscript.

ABBREVIATIONS

AA — Ascorbic Acid, $C_6H_8O_6$
ANF — Alumina NanoFiber
ANFC — Alumina NanoFibers coated by Carbon
BET — Brunauer-Emmett-Teller (surface area analysis)
CNT — Carbon NanoTube
CV — Cyclic Voltammetry
CVD — Chemical Vapour Depositon
DA — Dopamine, $C_8H_{11}NO_2$
DPV — Differential Pulse Voltammetry
EDX — Energy-Dispersive X-ray (spectroscopy)
EFTEM — Energy Filtered Transmission Electron Microscopy
ESA — Electrochemical Surface Area
ESCA — Specific Electrochemical Surface Area
GAIN — Graphene Augmented Inorganic Nanofibers
GCE — Glassy Carbon Electrode
GO — Graphene Oxide
GRM — Graphene Related Materials
HOPG — Highly Ordered Pyrolytic Graphite
HR-SEM — High Resolution Scanning Electron Microscopy
HR-TEM — High Resolution Transmission Electron Microscopy
IR — Infrared
MSC — Mesenchymal Stem Cells
MWCNT — Multi-Walled Carbon NanoTube
RBM — Radial Breathing Mode
RGO — Reduced Graphene Oxide
SCCNF — Stacked-Cup Carbon NanoFibers
SCE — Saturated Calomel Electrode
SEM — Scanning Electron Microscopy
SWCNT — Single Wall Carbon NanoTube
TEM — Transmission Electron Microscopy
UA — Uric Acid, $C_5H_4N_4O_3$
XPS — X-ray Photoelectron Spectroscopy

INTRODUCTION

Discovery of fullerenes in 1985 opens a new era in carbon science stimulating the exponential growth of research and resulting in many unprecedented inventions and novel applications of different carbon structures ranging from carbon nanotubes, graphene and graphene-like materials up to complex hybrids. Still, there are a huge number of exciting challenges and one of the major challenges is development and optimization of 3D architectures for highly demanding applications related to the global environment protection, bio-technology and energy storage.

Graphene, one of the youngest inventions among nanocarbon materials, is a two-dimensional single layer of sp^2-bonded carbon atoms arranged in a honeycomb shaped hexagonal lattice representing the basic building block for three-dimensional graphite, one-dimensional nanotubes, or zero-dimensional fullerenes. Graphene possesses a wide variety of extraordinary properties including enormously high mechanical strength, outstanding charge carrier mobility, high optical transparency, flexibility, *etc.*, which makes this material a promising candidate to be used in highly demanding nowadays applications such as IT-technologies, electronic gadgets, structural composites, bio-sensors, flexible displays, supercapacitors, solar cells, and so forth.

Both industry and governments provide considerable funding in development of novel devices and materials based on graphene exceptional properties, which should help in accelerating the rate of commercialization of the recent innovations. However, there is a series of obstacle to be overcame on the way to realization of a full potential of graphene for practical applications. One of the greatest challenges is a controllable growth of graphene films on a dielectric substrate and in a reproducible manner. Despite of recent progress, many of the promising applications of 2D nanocarbons are hindered either by technological difficulties in the production scale-up and integration into the multicomponent devices or require substantial research to prove their feasibility [1].

In this work, the simple and scalable process of chemical vapour deposition of graphene on the mesoporous substrate of ceramic nanofibers has been demonstrated. The study focuses on the elaboration of novel hybrid materials based on the high-tech Estonian product — alumina nanofibers of an aspect ratio of 10^7. Multifunctional hybrids are developed to overcome the limitations of the existing materials for tough and electroconductive ceramic-matrix materials; highly sensitive sensors of biological liquids; electrochemical energy conversion;

and scaffolds for bio-applications. It should be emphasized that the material solution relays on highly innovative developments of the Estonian industrial partners, which is complemented by new methods of material functionalization developed in TUT.

Developed material was used in number of studies and results were represented in 11 articles, this thesis is based on five of them. Also two patents were applied ”A ceramic composite material with funcionally graded properties” [I] and ”Self-aligned fibrous scaffold for highly anisotropic cell cultures” [H]. Progress and results related to the hybrid materials was approbated four times on international conferences. Moreover, studies related to graphenated hybrids are expanded and may lead in the near future to practical implementations.

1 REVIEW OF THE LITERATURE

1.1 Graphene

The explosive interest in a two-dimensional sheet of sp^2-hybridized carbon stems from extraordinary mechanical, structural, thermal, electrical, and electronic properties, and, therefore, from a potential it may provide for future advanced and sometimes unexpected commercial applications as two-dimensional crystals were believed to be thermodynamically unstable until 2004, when one layer of atoms was extracted from graphite by micromechanical cleavage.

By definition, graphene is "a single-atom-thick sheet of hexagonally arranged sp^2-bonded carbon atoms that is not an integral part of a carbon material, but is freely suspended or adhered on a foreign substrate" [2], Fig. 1.1. A single-layer graphene represents a single two-dimensional sheet of well-arranged carbon atoms with outstanding charge carrier mobility (electron mobility is estimated to be up to 15,000 $cm^2V^{-1}s^{-1}$ [3]) and exceptional stiffness (Modulus of elasticity is predicted to be up to 1.0 Tpa [4]). Recently, graphene was proved as a bio-compatible material that may be successfully used by bio-engineering and sensorics [5].

However, because an up-scalable production of a defect-free single-layer graphene is a great challenge up to now, the multi-layered graphene consisting of a small number of graphene sheets is widely used. Properties of a few-layered stacks of graphene sheets are somewhat distinguishing from properties of an "ideal" graphene. For example, an assembly becomes increasingly metallic showing excellent possibility for functionalization and/or decoration with nanoparticles required for the specific application.

Utilization of carbon nanostructures for a wide variety of applications requires a procedure for preparation of different objects depending on their specific needs. Most of the possible applications require growth of high quality graphene on a suitable substrate assuming precise control over the structure. This particular task is still a great challenge.

1.2 Synthesis of graphene

For complete realization of the practical potential of graphene, the obstacles, such as lack of defect-free graphene and reliable reproducible method for

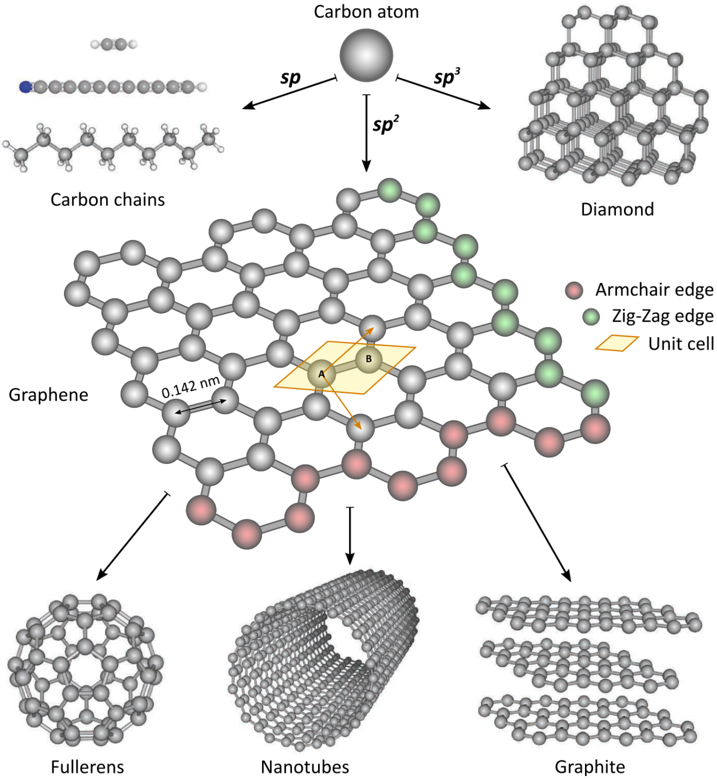

Figure 1.1 Structure of graphene, its derivatives and other carbon allotropes (adapted from [6]).

cost-effective and environmentally friendly fabrication of graphenated structures, have to be overcame. In this section, the commonly used methods for graphene synthesis are summarized. Despite of a wide variety of approaches, the methods can be broadly categorized as either bottom-up or top-down.

Fig. 1.2 shows the conventional methods of graphene preparation along with their key features and possible applications [7].

1.2.1 Top-down approach

As graphite presents the stacked layers of weakly bonded graphene sheets, it seems to be easy to produce graphene from a high purity graphite bulk. The main idea is breaking the Wan-der-Waals bonds applying mechanical or chemical energy to separate out stacked graphene sheets. Among the methods, exfoliation and cleavage are the most exploited ones.

Exfoliation represents a repeated peeling process. A commercially available highly oriented pyrolytic graphite (HOPG) sheet is subjected to extensive etching in oxygen plasma [8]. Different modifications of the original process allow production of large enough (∼10 μm) and flat graphene flakes of HOPG bonded

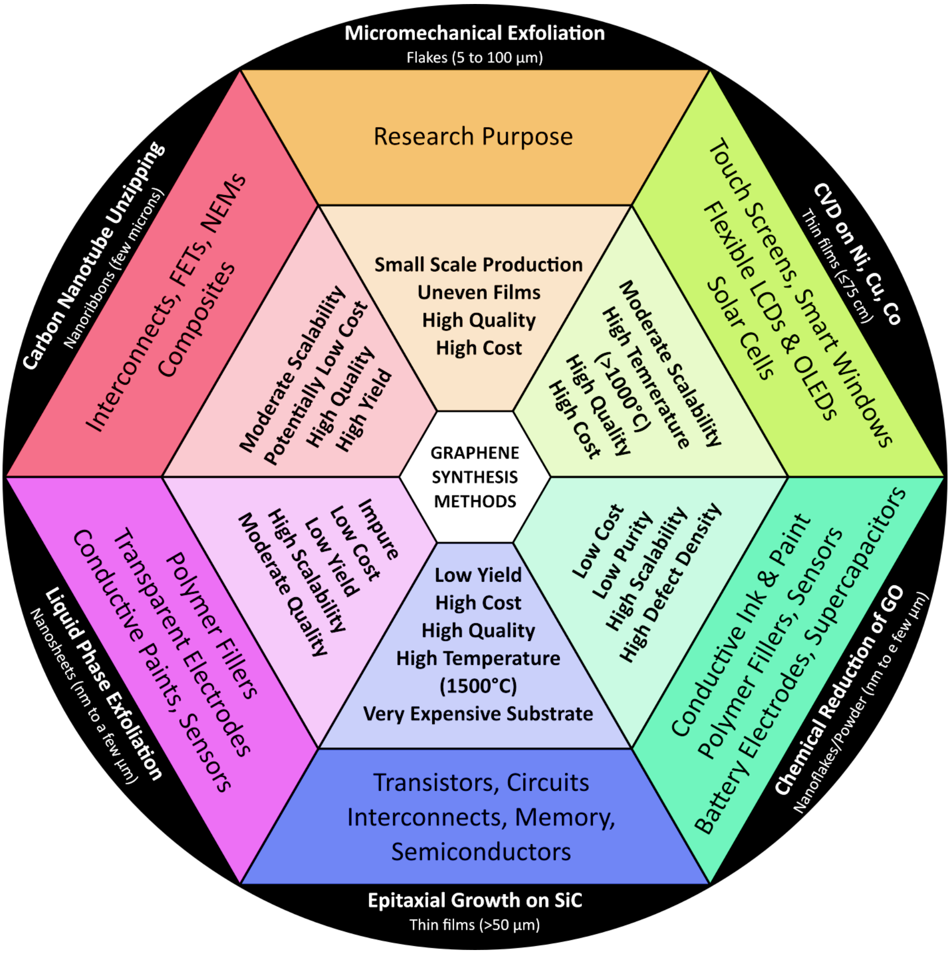

Figure 1.2 Approaches to make graphene (adapted from [7]).

to Si substrate followed by their exfoliation [9]. Millimeter-sized (mm-sized) several layers of graphene can be produced by bonding bulk graphite to borosilicate glass substrate [10].

Exfoliation is also possible in liquid phase playing with hydrophobicity of graphite oxide (GO) using ultrasonication in specially prepared suspensions with an attempt to reduce GO films [11]. To decrease the presence of residual oxygen in the exfoliated structures, method of dispersion and exfoliation of graphite in N-methyl-pyrrolidone was developed [12]. The solvent-graphene interaction in a suspension of similar surface energy is a key of success of the approach. A rod-coating technique [13] for the large scale production of reduced-graphene oxide (RGO) films combines the rod–coating technique with simultaneous reduction of oxides [14].

Among recent key developments, a mechanical exfoliation technique based on a controlled ball milling of graphite in a liquid medium; a microwave-assisted exfoliation based on intercalation and exfoliation of single sheets with the help of gases; and a continuous rubbing of graphite slabs against a rotating ceramic substrate in a solvent, can be named.

Although exfoliation techniques have the potential for the cost-effective and large scale production of graphene, there are several limitation factors, such as incomplete oxygen reduction, presence of impurities and defects causing by application of either aggressive solvents or mechanical loads.

1.2.2 Bottom-up approach

The bottom-up synthesis routes, which were developed quite recently [15] have the potential for production of carbon nanostructures at an affordable cost, are currently extensively used for graphene manufacturing.

One of the well-developed approaches is a thermal decomposition of silicon on the surface of 6H-SiC [16]. It has been shown that graphitic layers can be developed either on Si or carbon faces of a SiC wafer by sublimating Si atoms providing a graphitized surface [17] for further graphene layers growth. Epitaxially grown single or few-layer films may also have been synthesized on a Ni thin film deposited on a SiC substrate at relatively low temperatures of 750 °C [18] and atmospheric pressure [19]. However, the methods suffer from lack of control of layers' thickness and poor repeatability. Moreover, a microstructural analysis reveals that graphene grown on SiC(0001) and SiC($000\bar{1}$) surface planes has different structures. Several other substrates were studied to obtain the graphene monolayers. For example, single crystal Ru(0001) allows graphene growth under a ultra-high vacuum (4×10^{-11} Torr) [20] exploiting thermal decomposition of ethylene adsorbed on the surface or segregation of carbon. Following the similar procedures, graphene can be synthesized on many other single crystals of transition metal, including Ir, Ni, Co, Pt, *etc.* [21].

One of the very attractive options is utilization of greenhouse pollutant gases and recyclable minerals for graphene production. The process involves highly exothermic oxidation-reduction reaction between CO_2 gas and magnesium resulting in development of magnesium oxide and graphene. The process utilizes a highly exothermic reaction between CO_2 and magnesium permitting considerable reduction in energy consumption. Moreover, MgO and magnesium aluminate spinel nanopowders coated by multi-layered graphene may be simultaneously produced along with graphene.

Among the wide variety of bottom-up chemical routes available for graphene synthesis, an arc-discharge method [22] exploiting evaporation of pure graphite electrodes in different gases (air, CO_2, H_2, He, Ar, NH_3, *etc.*) has several important advantages as the produced graphene is of a high purity and crystallinity and, additionally, can easily be doped by nitrogen or other species required for a specific application [23].

An another approach to produce graphene from MWCNTs by process of their unzipping by ultra-sonication in an organic solvent [24] or using high strain rate deformation at 150 K [25] has recently gained a significant attention at research community. However, a reduced degree of control on size and morphology of the final product and its high cost are serious disadvantages of the processing method.

Currently, more than a dozen methods are proposed for graphene preparation. A synthesis route using chemical vapor deposition (CVD) has found a wide application as being the most prospective one due its possibility to produce defect-free graphene of a large size [26].

1.2.3 Chemical vapor deposition of graphene

Among other processing routs to produce graphene, deposition on transition metal substrates (Cu, Ni, *etc.*) is considered as the most promising relatively inexpensive approach of using different gas species which are fed into a hot reactor in the attempt to decompose hydrocarbon precursors to carbon radicals at the substrate surface [26]. During the reaction, the chosen metal works as a catalyst to decrease the energy barrier for the reaction to occur and determines the mechanism of graphene growth [27–29].

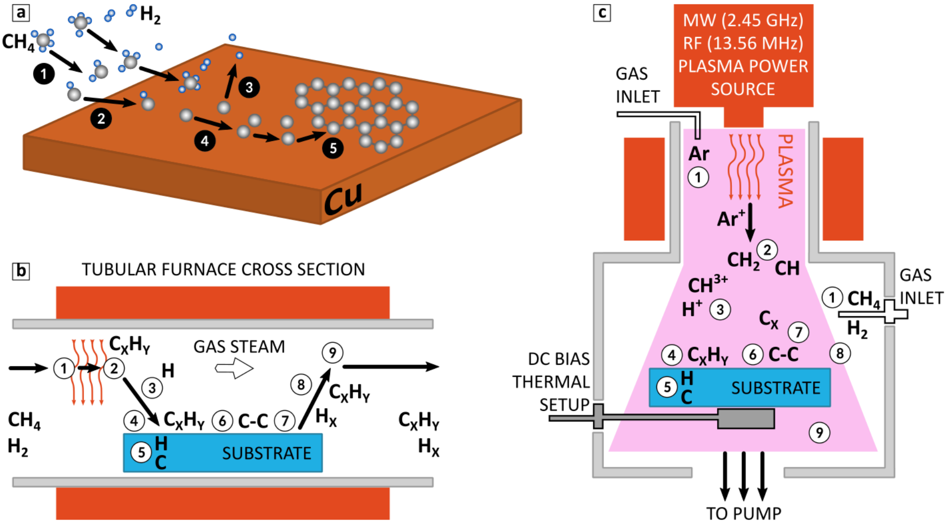

Figure 1.3 a) Growth kinetics in CVD-produced graphene on Cu, ❶ *– decomposition,* ❷ *– adsorption,* ❸ *– dehydrogenation,* ❹ *– surface migration and* ❺ *– attach and growth. Schematic of b) thermal CVD, and c) plasma-assisted CVD (precursor -* CH_4/H_2 *gas mixtures).* ① *– Transport of reactants by forced convection.* ② *– Thermal (b) or plasma (c) activation.* ③ *– Gas stream.* ④ *– Adsorption of reactants on the substrate surface.* ⑤ *– Dissolution and bulk diffusion of precursor.* ⑥ *– Thermal activation of film growth.* ⑦ *– Desorption of by-products.* ⑧ *– Transport of by-products by diffusion to the main gas stream.* ⑨ *– Transport of by-products by forced convection. (adapted from [30]).*

For example, a polycrystalline annealed Ni, Co or Ru substrate is exposed to H_2/CH_4 gas mixture to decompose hydrocarbon and to dissolve carbon into the substrate to form a solid solution. During following cooling down, the carbon atoms diffuse out from the sub-surface regions and precipitate on metal surface to form the graphene film. However, due to a low solubility of carbon in copper, graphene development on Cu is a surface-mediated self-limiting process. The kinetic of the processes is illustrated in Fig. 1.3a.

The main principals of both thermal CVD and plasma-assisted CVD processes are schematically shown in Fig. 1.3b-c.

Fast cooling rate is found to be a critical thermodynamical parameter responsible for suppressing the formation of many-layered graphene bulks [31]. Among other factors, a processing temperature and pressure, precursors flow rates, and an exposure time have a profound effect on the final product [32].

The main disadvantage of the CVD procedure is that the complete process typically requires transfer of the film from the support to the required dielectric substrate [33]. Therefore, the process is complicated by extensive energy consumption and scarifying of an underlying metal layer.

Method of the direct CVD growth of few-layered graphene on insulating substrates is of urgent need and represent the further challenge for research community. A recently developed method for the direct CVD of a single- or few-layer graphene film onto the dielectric surfaces via *in situ* graphene growth on non-conducting surfaces with the help of a controlled metal evaporation from the covering metal foil during the catalytic growth [34], although presented an interesting approach, requires a high quality sacrificial copper layer and precisely controllable parameters of the process.

The comparative analysis of different methods is given in Table 1.1 adapted from [35].

1.3 Graphenated structures

The overall possible graphene applications together with its limitations and method to produce the materials of the needed quality are summarized in Fig. 1.2. The progress is essentially driven by production of different graphene form and especially graphenated nanostructures with specific properties appropriate for the highly demanding applications. It is unlikely that graphene will soon be extensively used in high-performance electronics due to the absence of a large sheets of the ideal structures. However, many other, less stringent, applications of the graphenated nanocarbons or graphene related materials (GRM) are continuously being developed. Applications that could benefit from GRMs include flexible electronics, fuel cells and membranes, water splitting and hydrogen production, batteries with efficient anodes and cathodes, supercapacitors with high energy density, and solar cells [36]. For example, the system of intrinsically bonded CNT and graphene produced using plasma-enhanced CVD technique [37,38] is demonstrated to be successfully used for supercapacitors [39,40], lithium ion batteries [41], transparent conductive electrodes [42], neural stimulation electrodes [43] and carbon nanotube field

Table 1.1 Methods of graphene fabrication and possible applications of the graphene produced [35].

Method	**Crystallite size (μm)**	**Sample size (mm)**	**Charge carrier mobility (at ambient temperature) (cm^{2}V^{-1}s^{-1})**	**Applications**
Mechanical exfoliation	$> 1\,000$	> 1	$> 2 \times 10^5$ and $> 10^6$ (at low temperature)	Research
Chemical exfoliation	≤ 0.1	Infinite as a layer of overlapping flakes	100 (for a layer of overlapping flakes)	Coatings, paint/ink, composites, transparent conductive layers, energy storage, bioapplications
Chemical exfoliation via graphene oxide	~ 100	Infinite as a layer of overlapping flakes	100 (for a layer of overlapping flakes)	Coatings, paint/ink, composites, transparent conductive layers, energy storage, bioapplications
CVD	1 000	$\sim 1\,000$	10 000	Photonics, nanoelectronics, transparent conductive layers, sensors, bioapplications
SiC	50	100	10 000	High-frequency transistors and other electronic devices

effect transistors [44]. Many of this applications require high charge density at the nano-scale. Moreover, the structure of GRM can provide a controllable level of chemical interaction giving the specific functionalities for the devices under consideration.

A morphological classification of wide variety of available carbon nanostructures providing insight into the dimensional organization of peculiar graphenated structures, proposed in [45], is shown in Fig. 1.4. The corners of a triangle represent one-dimensional carbons; two-dimensional nanosheets; and three-dimensional graphenated nanostructures, which are of the greatest interest for future possible applications where charge densities are of primary importance.

The 3D architecture of nanostructures is currently represented by activated carbons and, recently developed graphenated-CNTs [37, 48]. Graphene nanoplatelets [49] have a high density of the exposed graphene edges, and, therefore, a high surface charge density as compared to SWCNT and MWCNT, but they are generally planar and unlikely be organized in a 3D network. This fact limits their ability to maximize charge density. Aligned CNTs make available a well-organized, high surface area 3D nano-structure, but expose primarily basal planes, which does not allow full exploitation of the potential of the ordered networks. The graphenated CNTs are somewhat transition from aligned bamboo-textured with graphene foliates grown on their surfaces and supposingly derived from stress-enhanced defects along [48]. However, the triangle has an unoccupied corner, that may denote structures yet to be identified. Conceptually, this symbolized the ultra-high density of dangling bonds, efficiently organized

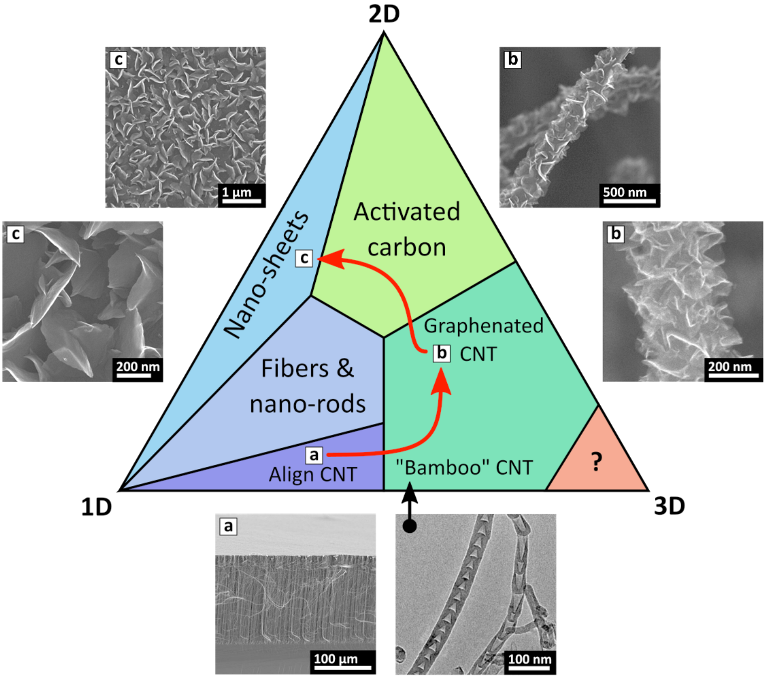

Figure 1.4 Triangle of graphenated structures: (a) aligned CNTs; (b) graphenated CNTs; (c) nanosheets or free standing graphene nanowalls (adapted from [46, 47]).

into a 3D geometry maximizing the charge density per unit area [45]. Therefore, the reliable procedure to produce foliated fuzzy graphenated structures and control over their properties is of the primary importance for progress in carbon-related areas, which may enable a range of materials features starting with the optimized energy/power densities, durability, and ending by the potentially reducing cost and minimal environmental impact. New product should be commercially viable and substantially surpass the performance of the existing materials at comparable manufacturing costs. Development of such kind of microstructures is one of the main tasks of the present work.

1.4 Objectives

One of the foreseeing game-changing breakthroughs is the development of a method of graphene growth on arbitrary surfaces at atmospheric pressure, relatively low temperatures by environmentally friendly procedure. Such rout enables to avoid the complex and cost-consuming transfer step and stimulate integration of graphenated structures with other materials to serve the specific needs as well as improve compatibility with nowadays technologies.

The main *motivation* of the work is urgent requirement in a simple and cost-effective procedure for direct growth of graphene of tailored and well-controllable morphology on dielectric materials. Moreover, the development of hybrid multifunctional materials is emerging as a relatively new and highly interdisciplinary field. The *focus* of the proposed project is related to hierarchically structured multifunctional graphenated hybrids based on the high-tech Estonian product – metal oxide nanofibers of a great aspect ratio. The research direction is *motivated* by the fact that in many cases the development of top-end products has reached limits set by the limited capabilities of the currently existing materials; as well as by the urgent need in a knowledge-based design, development and processing of industrially applicable materials for energy technology, healthcare and transportation. New horizons of products performance are directly connected with an intense need for innovative materials and processing routes to perform multiple functions.

The *overall objective* of the research is the development, optimization and production of multifunctional graphenated hybrids being beyond reach with conventional incremental materials development.

The *technological goals* of the study are:

- To design and work out the set-up for graphene deposition onto a ceramic fibrous substrate using the cost-effective CVD process;
- To develop a procedure for controlled carbon deposition aimed at production of graphenated nanostructures of different morphologies starting with the few-layer graphene coatings and ending by highly foliated graphene with a high edge densities;
- To perform a parametric study of the process to understand the main factors affecting microstructural features;
- To study the role of graphitic edges in oxygen electrochemistry;
- To test the produced graphenated structures for their possible use as a scaffold for regenerative medicine;
- To test the produced graphenated structures for electrochemical energy conversion;
- To test the produced graphenated structures as the candidates for electroconductive fillers to ceramic composites for added functionality.

As the *fundamental* advantage of a graphenated nanostructure is the electroconductivity combined with a tailorable surface area, a framework of the hybrid nanofibers coupled with the specified density of the graphene edges may serve many different tasks and find wide applications. The *aim* is to provide an active technological route for nano-structured hybrids through a variety of options, and make recommendations of those most likely to bring benefits by testing and analysing of their performance.

2 EXPERIMENTAL PROCEDURE AND MATERIALS

2.1 Ceramic nanofibers network

A ceramic nanofibers network, produced by a recently developed process of controlled liquid phase oxidation of an aluminium melt [50], was chosen as a substrate for carbon deposition. The network represents a mesoporous complex structure consisting of highly-aligned self-assembled nanofibers with a single nanofiber diameter ranged from 5 up to 50 nm and a narrow distribution of nanofibers diameters throughout one block. The typical aspect ratio is up to 10^7, Fig. 2.1e. The overall structure of the substrate and porosity distribution throughout the network of fibers of 7 nm in diameter are demonstrated in Fig. 2.1 [51].

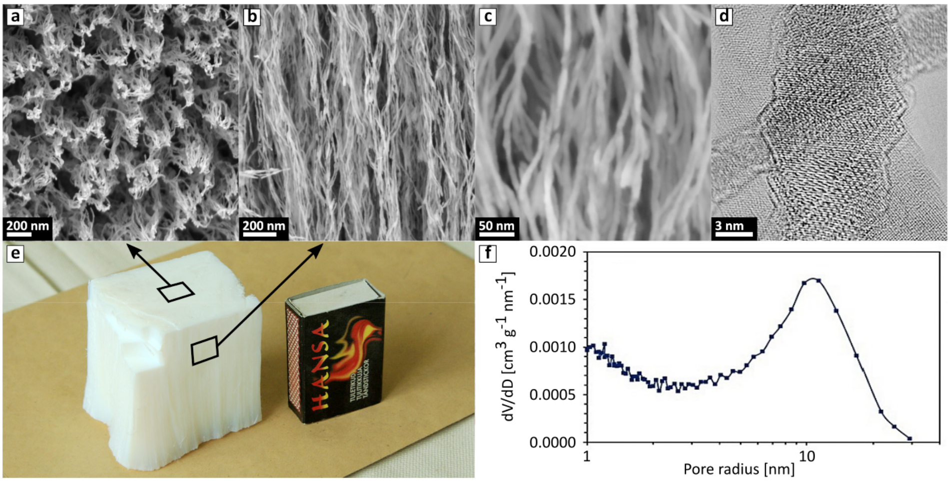

Figure 2.1 SEM micrographs of side (a) and top (b) of the network of alumina nanofibers. HR-SEM images at highest magnification (c). HR-TEM image of separated nanofibers (d). Optical photograph of the block of ceramic (γ-alumina) nanofibers (e). And differential pore size distribution in the network determined with the help of nitrogen adsorption (f). Adapted from [Paper II] and [51].

The specific surface area measured by BET method is ranged from 142 up to 175 m^2g^{-1} depending on fibers diameter. The as-produced fibers mostly composed of partially hydrated (2–6 wt.%) gamma-alumina phase that can be converted into alfa alumina by heat treatment at temperatures exceeded 1250 °C [52].

TEM and SEM studies show that a single nanofiber may have variations in diameter of approximately 0.5–1.5 nm, demonstrating sometimes twinnings or breakage. Nanofibers are well-aligned and hold together by weak hydrogen forces.

Differential scanning calorimetry performed in [52] combined with HR-TEM observations of specific ”zig-zag” surface structural features, Fig. 2.1d, revealed possible unsaturated Al^{3+} linked to three oxygen atoms. The cation Al^{3+} binds to hydroxyl OH^-, and protons form hydrogen bonds localized on the neighbouring Al–O–Al bridge resulting in formation of both terminal OH-groups and bridging groups indicated by the IR spectra in [52]. Therefore, the nanofibers in the network are hold together by weak hydrogen forces that can easily be broken in liquid solutions.

2.2 Laboratory CVD set-up

For carbon deposition onto the mesoporous substrate of ceramic nanofibers, a custom made thermal ”hot-wall” chemical vapour deposition setup has been worked out. The schematic representation of the device is shown in Fig. 2.2.

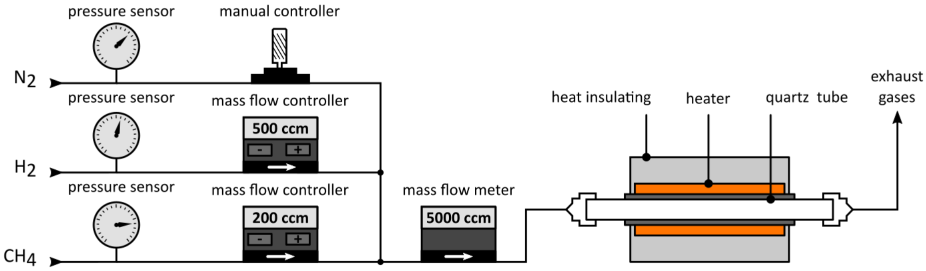

Figure 2.2 Schematic diagram of laboratory setup.

The laboratory installation includes a four-channel gas system with input pressure gauges (*Swagelok*), digital flow controllers (*ALICAT*) for two channels (methane and hydrogen), manual low flow metering valves for two other channels (nitrogen and argon) and one common flow-meter. The main part of the set-up, a processing reactor, is a quartz tube with a length of 150 mm, an inner diameter of 10 mm, and a wall thickness of 1.5 mm placed in specially designed tube furnace (*MEYER-vastus*) settled to continuously work at maximum 1000°C. The mass flow-meter allows measurement of up to 5 litres per minute (l/m) and mass flow controllers — up to 500 cm^3min^{-1} for H_2 and up to 200 cm^3min^{-1} for CH_4. The setup is mounted inside a fume hood so that all exhaust gases or any leakages can be immediately removed. Ultra-pure hydrogen 99.999 vol% (UN 1049, 5.0), methane 99.5 vol% (UN 1971, 2.5) and technical nitrogen 99.5 vol%

(UN 1066) were supplied from gas cylinders located in a separate room. In case of a high content of hydrogen, the exhaust gases were after-burned with the help of an alcohol burner.

2.3 Characterization

Weight of a deposited coating was determined by the ELTRA 84 analytical balances located in close proximity to the CVD reactor, allowing immediate measurements after processing.

Microstructural features were examined by a high-resolution scanning electron microscopy (HR-SEM) Zeiss HR Gemini FESEM Ultra 55 equipped with Bruker EDX system ESPRIT 1.8 suitable for energy-dispersive X-ray measurements.

Morphology at a higher magnification and structure of carbon coating was studied using two transmission electron microscopes: JEOL JEM-2200FS HR-TEM with two C_S-correctors, 200 kV field emission gun (FEG) and in-column energy filter (Omega Filter) configured to produce a high-end energy filtered imaging; and Zeiss Libra 200 FE energy-filtered transmission electron microscopy (EFTEM) equipped with a high efficient Field Emission cathode (200 kV) and energy Omega-filter.

Raman spectroscopy, used for characterization of carbon layers, was performed with the help of Horiba JobinYvon HR800 high resolution Raman spectrometer equipped with a green Nd:YAG laser (λ=532.1 nm), a red He-Ne laser (λ=632.8 nm), and a multichannel CCD detection system in the backscattering configuration. For peaks fitting and peaks parameters calculation MagicPlot [https://magicplot.com/] software was applied.

X-ray photoelectron spectroscopy (XPS) was performed with an Omicron Multiprobe XPS system with a base pressure of 2×10^{-10} mbar, using a monochromated Al Kα source (hν=1486.6 eV) and an EA125 U5 analyzer at a 45° takeoff angle. Wide surveys were collected at 50 eV pass energy, while core level spectra were collected at 20 eV pass energy. Data collected were analyzed using CasaXPS [http://www.casaxps.com/] software.

The carbon content deposited onto the fibers was determined by thermo-gravimetric analysis using Stanton Redcroft device at maximum temperature of 950°C in air. The heating rate was settled to 5 $°C\cdot min^{-1}$. Specific surface area was estimated with the help of a Quantachrome Autosorb iQ instrument running nitrogen physisorption measurements at 77 K.

3 RESULTS AND DISCUSSION

3.1 Procedure of graphene deposition

3.1.1 Graphene deposition with catalyst

The carbon film in the complex form of co-existence of carbon nanotubes (CNT) and multi-layered defective graphene coating was deposited onto alumina nanofibers of aspect ratio 10^7 by the hot-wall CVD process. For catalyst deposition a gas phase, the network of ceramic nanofibers and 5–15 wt.% of ferrocene $Fe(C_5H_5)_2$ powder were placed into a boron silicate flask pre-filled by argon, which then was annealed at 250 °C for 15 minutes in a muffle furnace. Sample decorated with partially oxidized iron nanoparticles was placed in a quartz tube heated up to 1000 °C in nitrogen atmosphere and further reduced in hydrogen for 10 minutes.

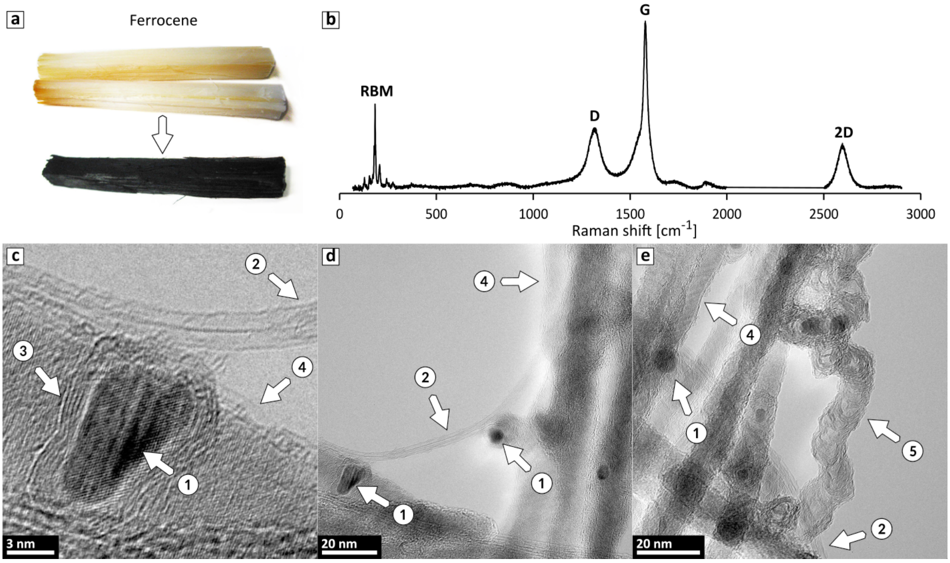

Figure 3.1 Sample with Fe catalyst nanoparticles deposited by gas phase, before and after CVD (a); Raman spectra of carbon coated sample (b); HR-TEM images of graphenated nanofibers (c),(d) and (e). Where arrows is indicate to: ① – iron nanoparticle, ② – carbon nanotube, ③ – 5-6 graphene layers around catalyst, ④ – 1-3 defected graphene layers around the nanofiber, ⑤ – carbon nanofiber.

Figure 3.1 demonstrates the most pronounced features of the substrate functionalized by carbon. The substrate in the form of a bundle of tightly packed fibers was quite homogeneously deposited by iron nanoparticles from the gas phase, Fig. 3.1a. The HR-TEM images of the carbon nanostructure are presented in Fig. 3.1c-e clearly demonstrating the nanoparticles of the catalyst ①, carbon nanotubes ②, multi-layered graphene ③, few graphene layers with different defectiveness ④, and carbon nanofibers ⑤.

The catalyst particles promote the decomposition of methane and formation of graphene. Therefore, around the metal nanoparticles coating is relatively thick ③ as compared to layers grown on the fibers' surface ④. The hypothesis behind using a catalyst suggested that carbon accumulated around the nanoparticles will be spreading in different directions, thereby covering the ceramic nanofibers.

Expectedly, the presence of metal nanoparticles promotes growth of CNTs ② and stacked-cup carbon nanofibers (SCCNF) ⑤. The nanotubes grow from the fine particles (around 1 nm) and the carbon nanofibers develop from the larger particles (3 nm and more). The radial breathing mode (RBM) in Raman spectra (50–400 cm^{-1}) indicates the presence of CNTs, Fig. 3.1c. Nanotubes diameters, calculated with the help of Raman spectroscopy, are in the range from 0.9 to 1.3 nm.

3.1.2 Graphene deposition without catalyst

As the fibers in the network have some structural nano-sized irregularities, Fig. 2.1d, it was suggested that graphene may grow onto the ceramic substrate without catalyst that influence the quality of the coatings to a great extent. For carbon deposition without catalyst, the network of ceramic nanofibers was directly placed into the reactor preheated up to 1000 °C. Before deposition, each sample was first annealed for 5 min in air and then 5 min in nitrogen to purify the substrate from any impurities and/or bond water. Graphene growth was performed by sequential introduction of the mixture of gases: methane as a carbon precursor and nitrogen and/or hydrogen that allows control of the morphology of graphene layers.

The optimized procedure of graphene layers is described in detail in our works [Papers I–III]. A simple single-step CVD process was performed at atmospheric pressure and temperature of 1000°C in the atmosphere of methane (CH_4) flowing with a rate of 50 cm^3min^{-1} and nitrogen (N_2) flowing with a rate of 500 cm^3min^{-1} required for elimination of the products of reaction. Time of the reaction was adjusted depending on the desired structure of the coating; for example, mass gain of 15 % of the substrate weight is reached during 20 min of processing.

The final product — alumina nanofibers (ANF) coated by carbon (ANFC) exhibits Raman spectra, Fig. 3.2b, of the layered structure revealing no peaks in between 50–400 cm^{-1}, which points to an absence of the CNTs. Also, significant change in I_D/I_G ratio indicates defectiveness of the structures. The detailed analysis of Raman spectra depicted from the samples with different morphology

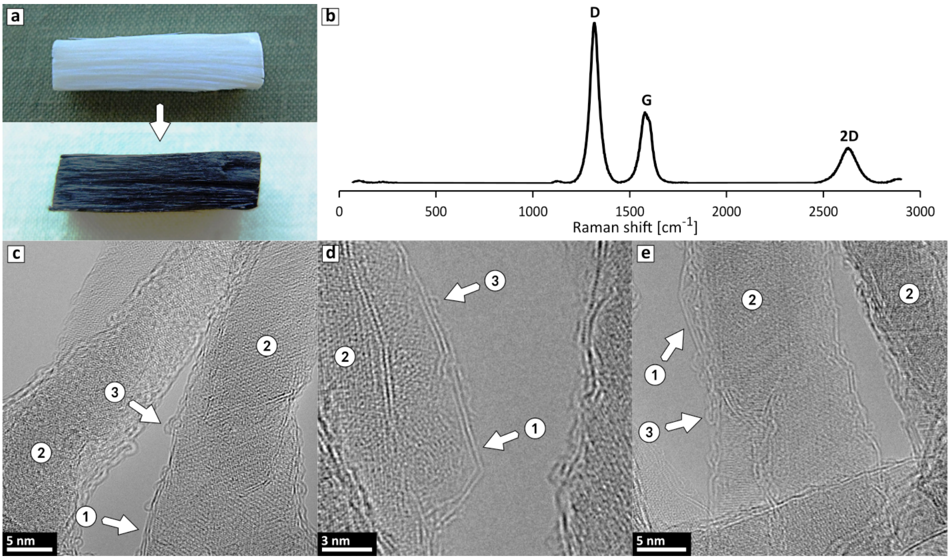

Figure 3.2 Common view of the fibers network before and after deposition of graphene (a). Raman spectrum (b). TEM images of covered ceramic nanofibers (c)-(e). Label ① points to graphene layers, ② marking substrate nanofibers and ③ indicates the islets of the last layer.

of the graphene layers is given in [Papers I–IV]. The characteristic Raman spectra of graphene grown on alumina nano-fibers demonstrate the well-pronounced peaks at around 1596 cm^{-1} (G band) indicating the formation of a graphitized structure; at 1340 cm^{-1}(D band) providing further confirmation for the graphitic carbon formation; and a peak at ca. 2700 cm^{-1} (2D band) reflecting multi-layered structure of coatings.

3.2 Graphenated nanostructures

3.2.1 Morphological study

Depending on the process parameters, the nanostructures of different morphologies can be produced as shown in Fig. 3.3. It was demonstrated that alumina nanofibers could successfully serve as a substrate for the direct catalyst-free synthesis of graphene with tailored number of layers and density of foliates, Fig. 3.3.

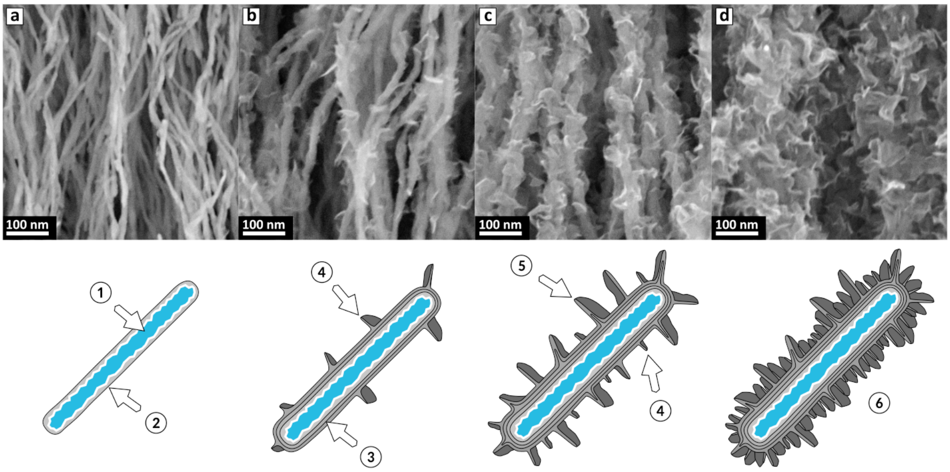

Figure 3.3 schematic of the structure of the coating. Label ① indicate substrate fiber, ② – first few (1-5) layers, ③ – many (5-15) layers, ④ – new thin flake, ⑤ – evolved thick flake, ⑥ – resulting coating with maximum density of the flakes.

As soon as the weight gain (ΔW) of the carbon coating is reached of about ΔW=150 %, the formation of the graphene flakes along the longitudinal axis of the fiber is observed. The appearance of foliates is similar to the leaves of aquatic plants *"Leptodictyum riparium"*: quite homogeneously distributed foliates grow perpendicular to the fiber surface and their density is regulated by process parameters.

Figure 3.4 indicates the carbon increment registered in a set on samples grown at 1000 °C without catalyst but at different deposition time and a rate of methane flow. At the constant temperature, the most affecting factor in controlling layers morphology was the time of reaction. Extending the deposition time provides a higher weight gain, and, as it is shown in Fig. 3.5, a larger number of the layers. Figure 3.5 demonstrates the sample gained 170 % of the weight with the clearly observed 7–10 graphene layers. The maximum achieved ΔW in this set is 869.7 % produced in CH_4 flow 200 $cm^3 min^{-1}$ with growth time 120 min. The set of experiment performed for longer time (5 and 48 hours with the weight gain of 1096.2 % and 1171.5 %, respectively) did not reveal any substantial difference in the flakes shape, distribution and density as compared with the

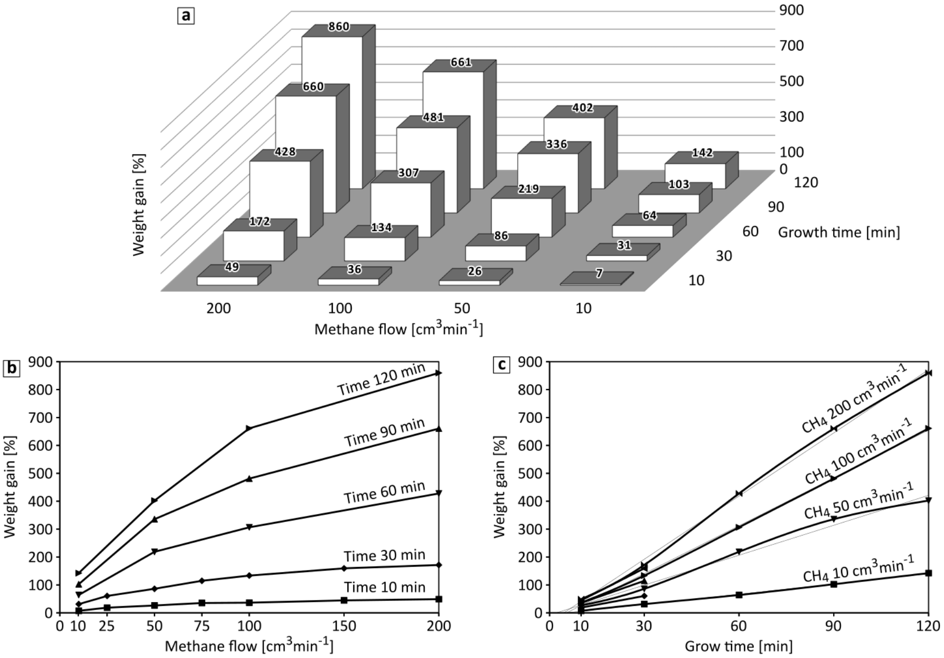

Figure 3.4 Weight gain observed in the set of samples where methane flow rate variates from 10 to 200 cm^3min^{-1} and growth time from 10 to 120 min (a). Separately shown dependencies of the weight gain from the methane flow rate (b) and growth time (c).

specimen treated for 2 h. Therefore, the saturation in carbon deposition may be explained by limited room for foliates growth that is essentially determined by the inter-fibers distance in a substrate. The saturation occurs at ΔW of around 700–900 %, due to difficulties for penetration of carbon atoms deep inside the sample representing a branched structure. Gas penetration or inter-fibers channels closing fully completes at around ΔW=1200 %.

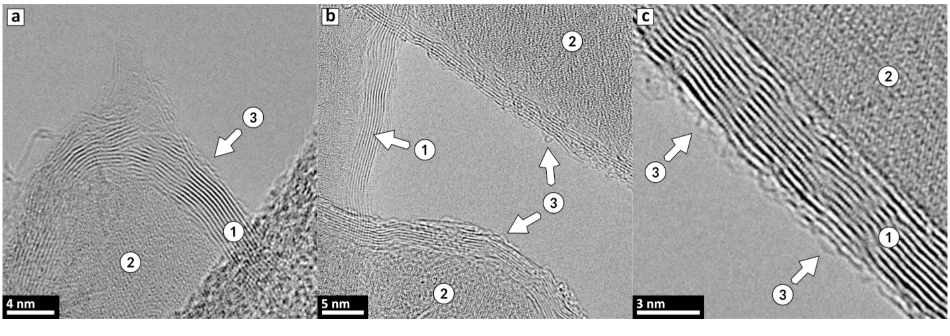

Figure 3.5 TEM images of carbon coating consisting of seven to ten graphene layers in different magnification. Label ① points to stacked graphene layers, ② marks a substrate nanofiber; and ③ shows outer highly defective layer.

From the series of the experiments, it can be assumed that the graphene layer looks like a patchwork quilt. With an increase in number of layers, the size of the graphene domains increases. The boundary between domains may play a role of nucleation centres for new domains creation.

The TEM study of the microstructural features revealed slight oscillation of the flakes that interferes sharpness at the edges of foliates. Figure 3.6 shows the HR-TEM images of the foliated graphene multi-layers indicating the structural features of the coating deposited at the flow of CH_4 during 90 and 120 min.

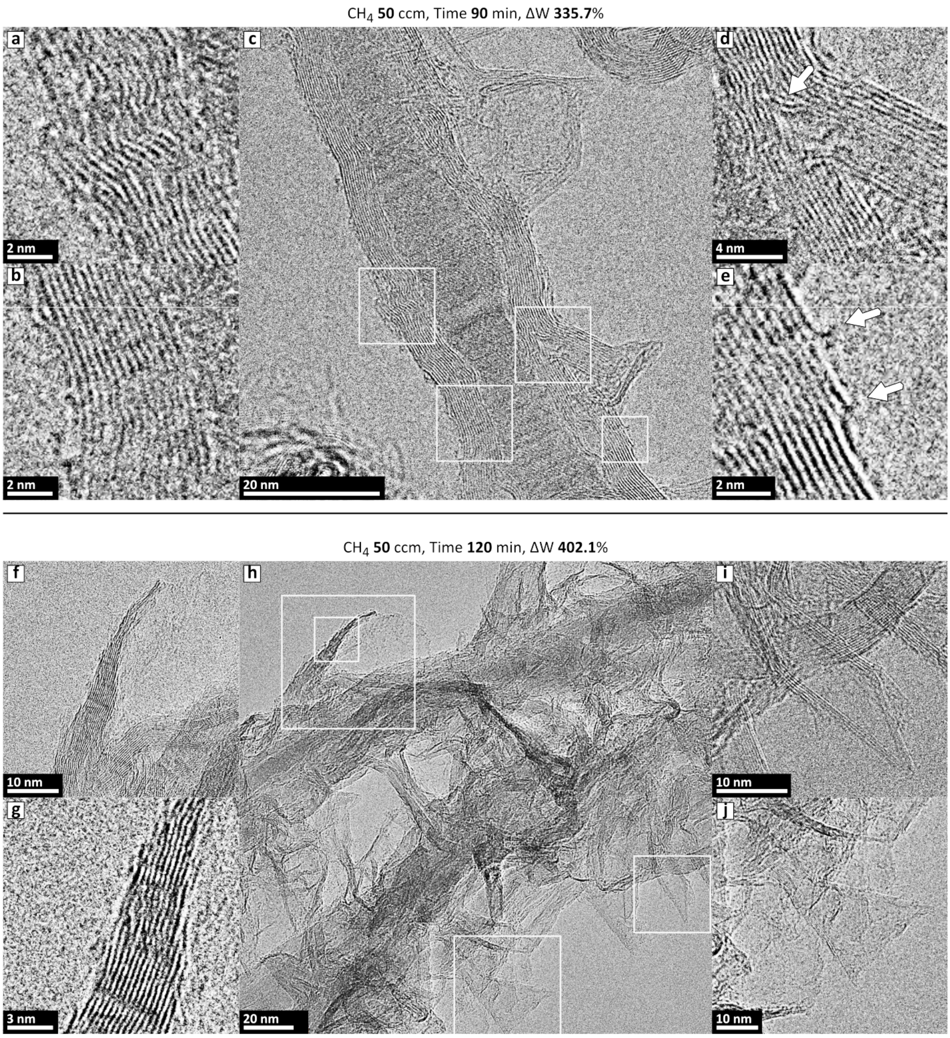

Figure 3.6 TEM images of coating structure in details and graphene flakes internal organization: (a, b) – well-recognized graphene layers; (c) – general view with marks of zoomed areas; (d) – point of bifurcation of graphene layers; (e) – free edges of the outer layers; (f, g) – nanostructure of foliates; (h) – common view of the foliated structure; (i, j) – flakes of few graphene layers.

Figure 3.7 provides an insight into the structure of foliates. The multi-layered graphene sheets can obviously be seen giving quite a high density of the free edges that can successfully be used for electrochemical and electrode needed applications.

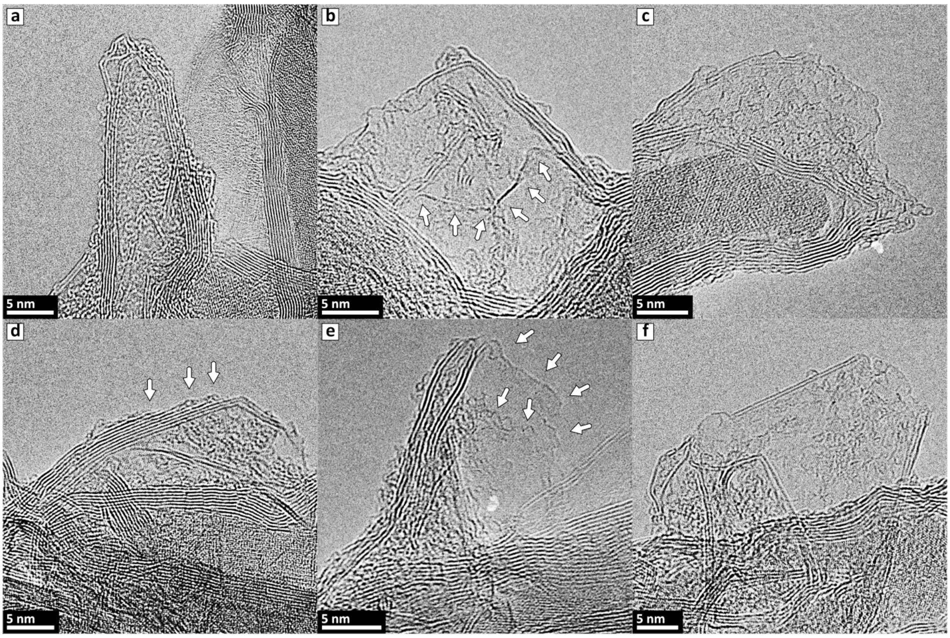

Figure 3.7 (a-f) HR-TEM micrographs of foliates from different locations. Arrows indicate the edges of layers.

3.2.2 Mechanisms of graphene growth

Study of the mechanism of foliate formation may give a new path for tailoring nanostructures. A stress-buckling mechanism described elsewhere for the graphenated CNTs [46], suggested a residual stress build-up between CNT walls due to unequal growth rates. Here, an alternative method is proposed. Carbon radicals in close vicinity of the unsaturated aluminium sites and/or structural defects on the substrate surface create the nucleation seeds for the development of foliates. Then, during growing, the expanding domains touch each other to form a specific structure. The possible options can be sub-divided into two parts depending of the availability of the nucleation sites. Options for a ”smooth” surface with low amount of sites (types A and B) as well as ”rough” surface with considerable amount of sites (types C and D) are provided in Fig. 3.8.

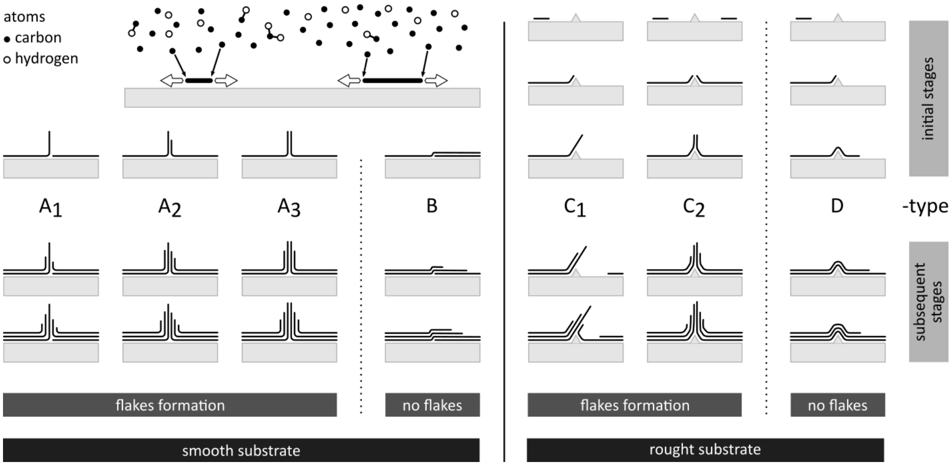

Figure 3.8 Schematic of the proposed types of flake formation mechanisms. Stages of the deposition procedure is indicated in the right side of the figure.

3.3 Parametric study of the graphenated nanostructures

The screening experiments involved studying of effects of the reaction time, gases flow rate and presence of hydrogen in a gas mixture on morphology of the nanostructures.

3.3.1 Hydrogen

The molecular hydrogen (H_2) can be used as a diluent gas for the carbon precursor and may affect the process of CVD graphene growth [53]. Thermal decomposition of methane itself produces hydrogen and carbon radicals together with intermediate compounds C_xH_y. The presence of additional hydrogen shifts the balance of the decomposition reactions capturing free carbon radicals and the formation of excessive amount of C_xH_y. Hydrogen interaction with the substrate influences the kinetic of CH_4 chemisorption [54], as H_2 and/or atomic H participate in the initial physical adsorption of CH_4 and create sites for sticking hydrocarbon and carbon radicals on the surface eliminating hydrogen and passivating defects [30]. This can result in several consequences. At a low hydrogen concentration, the graphene edges are not passivated and inclined to tight attachment to the substrate surface resulting in the limited diffusion of active C atoms beneath the graphene top layer and producing ”smooth” nanostructure [55]. High load of hydrogen stimulates termination of the graphene edges and the active diffusion of carbon with formation of additional layers. Also, H_2 decreases the rate of coating formation due to the smaller number of the available carbon atoms. Moreover, it may improve the quality of the coating due to etching of highly defective carbon constructions.

Figure 3.9 shows an influence of hydrogen on the weight gain revealing substantial decrease in weight accompanying an increase in H_2 content.

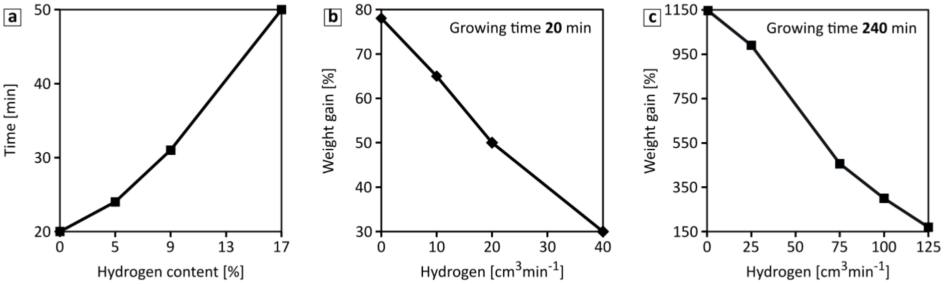

Figure 3.9 Correlation between growth time and hydrogen content in methane-hydrogen gas mixture [%] (a). Correlation between coating weight [wt%] and hydrogen additive [cm^3min^{-1}] to the methane flowing at a rate of 200 cm^3min^{-1} during 20 min (b) and 240 min (c).

The weight of the coating decreased from 77.6 to 29 weight percent with an increase in the hydrogen content in methane-hydrogen mixture from 0 to 16.7 % at growth time of 20 min. For a growth time of 240 min, the coating weight decreased from 1067.3 to 170.8 % with an increase in the hydrogen content from 0 to 38.5 %. As soon as the hydrogen content in mixture reaches 45 %, carbon growth on the surface of ceramic nanofibers is completely stopped. Figure 3.9a demonstrates almost linear dependence between the hydrogen content and the reaction time. Increasing hydrogen content in methane-hydrogen gas mixture from 0 to 17 % results in increase time needed for coating growth with the weight of 80 % from 20 to 50 min.

Moreover, hydrogen noticeably change graphene flakes shape, Figure 3.10. The flakes appearance is more sharp and thin, and density of the flakes are apparently higher. Foliates grown in the pure methane look shorter and of more rounded shape.

Presumably, graphene grown with the addition of hydrogen is of higher quality. This hypothesis is supported by Raman spectroscopy illustrating that I_D/I_G ratio insignificantly and evenly decreases from 1.7 to 1.2 with an increase in hydrogen content mainly due to an increase of G peak intensity, while D peak is remained of the same intensity.

A growing carbon structure consume atoms from the space in the immediate vicinity; therefore, concentration of carbon and hydrogen atoms (C/H ratio) is important. A high concentration of carbon atoms leads to a shorter growth time, but a lower quality of the resulting material. High concentration of the hydrogen atom leads to a higher graphene quality but a longer growth time. Consequently, structures obtained in a competition between deposition and etching will consist of those carbon atoms which have been assembled into defect-free clusters with strong interconnections. All weakly bonded atoms will be etched by

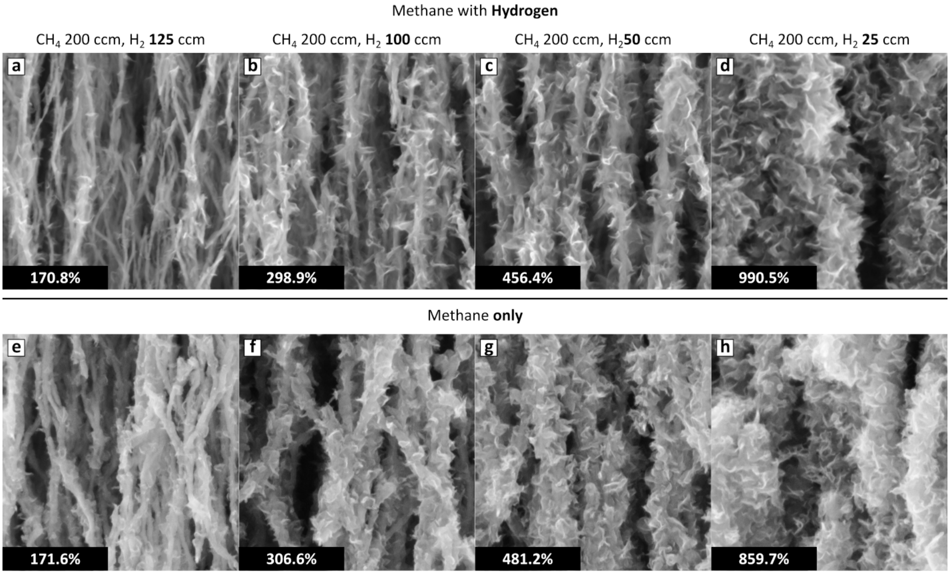

Figure 3.10 SEM images of graphene flakes grown in the presence of hydrogen (a),(b),(c),(d). The CH_4 and H_2 flow rates are indicated above the images. SEM of the flakes grown in pure methane, but with the similar weight of coating (e),(f),(g),(h).

hydrogen. And this competitive environment can be adjusted by controlling the methane-hydrogen ratio, or in the general case by C/H ratio.

Optimum of hydrogen load, growth time and weight of coating for ANFC structures is found to be in the range of 20–35 % of hydrogen content in the gas mixture. However, growing under high hydrogen concentration is a time-consuming process, especially for making samples with high amount of carbon. Moreover, for some applications graphene of high quality is not required. Conversely, the additional process, activation, can be performed if the goal is to increase amount of defects in a carbon structure as it may increase the activity of the material in case when the interaction occurs on the defects. From this point of view, creation of initially defective structure can make sense.

3.3.2 Reaction time and methane flow rate

To study the evolution of the foliates, the following parameters were chosen: methane flow rate 10, 25, 50, 75, 100, 150 and 200 cm^3min^{-1} and growth time 10, 30, 60, 90 and 120 min. The maximum methane consumption is limited by equipment. Figure 3.11 illustrates the effect of the reaction time and the methane flow rate on developed morphology of the ANFC.

The evolution of the graphene flakes is visually seen. First discernible flakes appear when the weight gain $\Delta W=100$ %. In the range $\Delta W=200$–400 %, nanofoliates fast occupy all available space increasing in size and density. After $\Delta W=500$ %, it is hardly to find morphological difference between samples in the

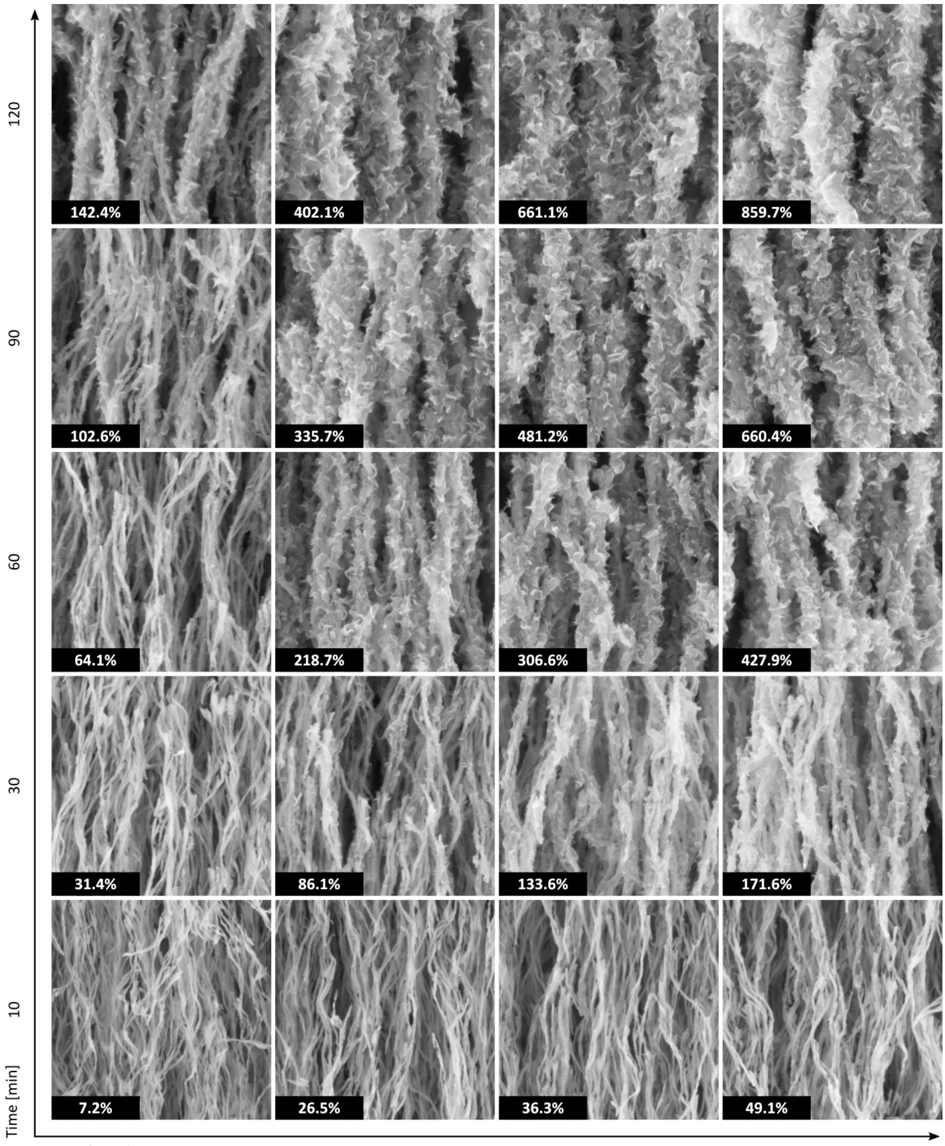

Figure 3.11 HR-SEM images of the developed nanostructures. Coating weight is indicated inside a black rectangle, the width of this rectangle is 400 nm.

HR-SEM images. The conclusion from the study of full factorial set of samples can be as following: if there is a need to produce the samples relatively fast and with coating weight of near maximum, it is preferable to use a higher available methane flow; if there is a need to produce the well-developed surface, the best way is to use methane flow of 50 cm^{3}min^{-1} or less adding hydrogen.

3.4 Characterization

Detailed characterization of the obtained graphenated nanostructures is described in papers [I and III]. Here, the most important features and properties are communicated.

3.4.1 X-ray photoelectron spectroscopy

The XPS analysis, Fig. 3.12 [Paper III], illustrates the fact that ANFCs are mainly composed of oxygen and carbon. XPS survey spectra reveal C 1s and O 1s as the most pronounced peaks. The sample of the low carbon content (ΔW=15 %) generates two peaks associated with the binding energies of 74 and 119 eV, which are absent in other materials and relates to Al 2p and 2s photoelectrons, Fig. 3.12a.

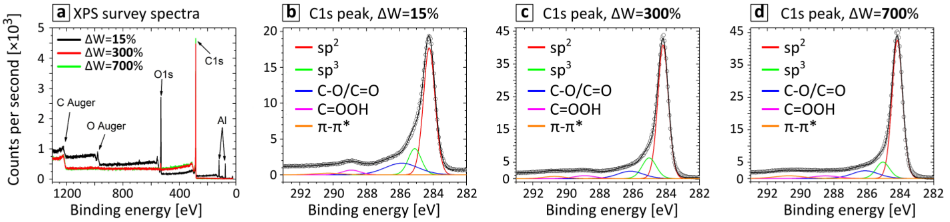

Figure 3.12 X-ray photoelectron spectra survey (a). High-resolution spectra of C 1s peak of samples with different coating weight gain, ΔW=15 % (b), ΔW=300 % (c) and ΔW=700 % (d). Adapted from [Paper III].

The oxygen content is the lowest one for a highly graphenated nanostructure (ΔW=700 %), thus indicating high carbon purity of the deposited film [Paper III]. The C 1s spectra exhibit a sharp peak at 284.3 eV with additional contributions at higher binding energies, Fig. 3.12b-d [Paper III], which can be ascribed as a trigonally bonded carbon (sp^2 centers), tetrahedrally bonded carbon (sp^3 centers), C-O/C=O carbon, carboxylic acid groups, and π–$\pi*$ shake-up peaks, respectively [Paper III]. Fibers covered by 2–5 layers of graphene (ΔW=15 %) have the lowest sp^2 concentration (63 %) and the highest concentration of oxidized carbon centers (20 %). Therefore, at the early stages of deposition, the layer chemically interacts with the oxide support [Paper III].

3.4.2 Raman spectroscopy

Figure 3.13 demonstrates the spectra depicted from pure alumina, few-layered graphenated alumina, alumina coated by the foliated graphene; and MWCTs since alumina nanofibers encapsulated by graphene may be essentially described as a multiwalled carbon nanotube filled by ceramic nanorod. The detailed analysis of the Raman spectra is given in [Papers I–III].

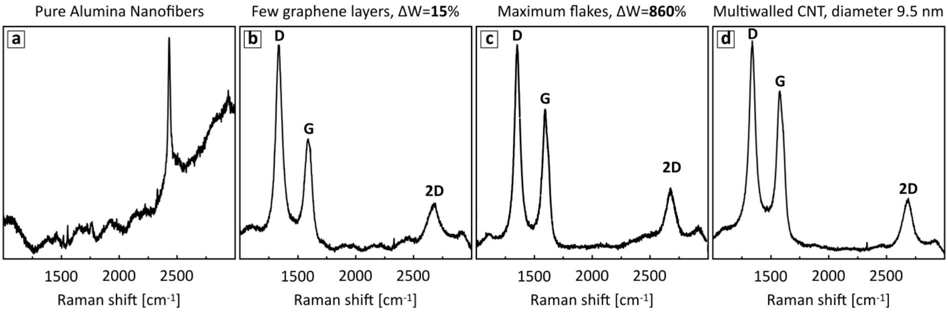

Figure 3.13 Raman spectra from purified alumina nanofibers (a), slightly coated (ΔW=15 %) (b) and deposited by flakes near maximum (ΔW=860 %) (c). Commercially available MWCNT (d).

The characteristic peaks for graphene structures are D and G peaks at ~1350 and ~1590 cm^{-1}, respectively [56]. Additional peaks at 2680, 2930, and 3230 cm^{-1} represent characteristics of graphene layers [57]. A single symmetric peak at 2680 cm^{-1} indicates a few-layer graphene, as there is no splitting into an asymmetric doublet typical for graphite [57]; moreover, the relatively narrow bands suggest the nanocrystalline structure of layers and foliates.

Taking into consideration the fact that intensity of the D, G and 2D peaks changes insignificantly, and the I_D/I_G ratio is kept to be equal 1.45 ± 0.07 at weight gain from 100 up to 900 %, an attempt to reveal interrelation between graphene flakes evolution and Raman peaks was performed. The study was inspired by the recently examined free-standing graphene stacks of 2–20 layers and observation of a panoply of Raman peaks at the frequency range of 80–300 cm^{-1} [58].

The observed peaks frequencies and shapes are unique for the specific number of layers [58], and effect is repeatable at different energies of excitation photons, E_{exc} = 1.58 eV (785 nm), 1.96 eV (633 nm), and 2.33 eV (532 nm) (Fig. 2b in [58]). Five samples with gradual increase of size and density of flakes with clearly distinguishable morphological features were chosen for investigation. The Raman measurements were performed using two lasers, green and red, with photon wavelengths 532 nm and 633 nm, respectively. Raman signals were collected from five adjacent points and averaged; for isolation of a signal from the flakes, the spectrum from the sample with the weight gain of 26 % was used as a baseline and extracted from all other spectra. Figure 3.14, represents the Raman response observed in the range 150–350 cm^{-1} in green and red excitation light and definitely testifies to the interrelations between the obtained peaks and modifications of coatings morphology.

Under a green laser, there are three discernible peaks can be found, the peak labelled as ① at 238.3 cm^{-1} , the peak ② at 269.5 cm^{-1} and the peak ③ at 287 cm^{-1}. With a help of the red laser, four peaks, ❶ at 185.5 cm^{-1}, ❷ at 213.7 cm^{-1}, ❸ at 244.5 cm^{-1} and ❹ at 290.5 cm^{-1} were found. Under the green light,

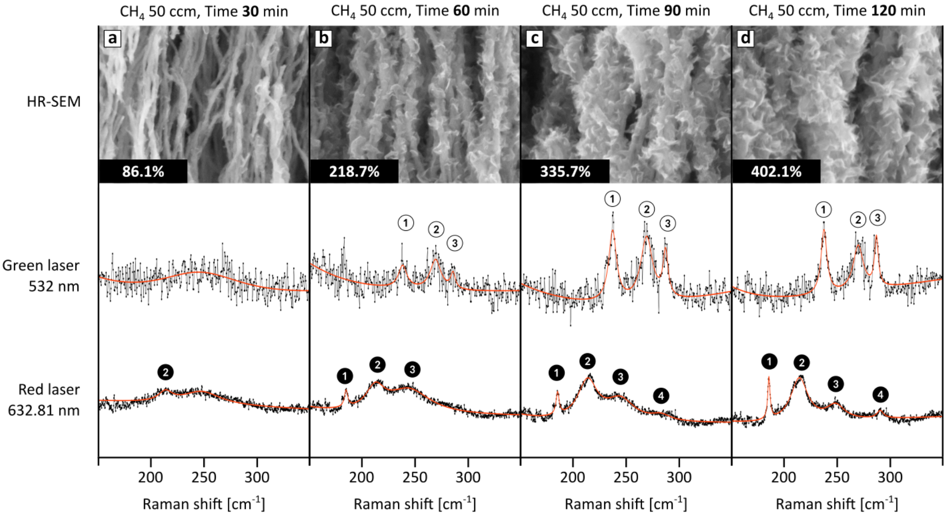

Figure 3.14 Raman spectra of four samples obtained at two excitation energies 2.33 eV (Green laser) and 1.96 eV (Red laser) representing dependence between coating morphology and peaks in the range 150–350 cm^{-1}.

a signal/noise ratio is worse as compared to the red one: the peaks are more recognizable and sharp. Excitation by red laser provides much lower noise but the peaks looks a bit suppressed. Only peaks ❶ and ❷ can be reliably allocated. Moreover, the peak ❷ probably consists of two overlapping peaks. Predictably, it is hard to tie up the measured spectra with the results obtained on a high quality graphene with an exact number of layers; however, it can be used as an empirical correlation stimulated by flakes evolution.

4 APPLICATIONS OF GRAPHENATED STRUCTURES

4.1 Material for electrochemical energy conversion

With the exhaustion of conventional energy sources, the need in renewable and efficient energy is continuously growing [59, 60]. The challenge is the development of a simple, repeatable and environmentally friendly process for production of the tailored and controllable graphenated nanostructures [61]. In publication [II], the alumina nanofibers network, which were successfully used as a substrate for the single-stage non-catalytic synthesis of graphene, is shown to serve as an excellent material for the electrochemical energy conversion due to presumably high electrical conductivity, chemical inertness, suitable durability, proper geometry allowing access to all catalyst particles, as well as a long time stability and reproducibility of functional characteristics [D]. The long-standing problem of agglomeration of the CNTs and/or graphene nanoplatelets has been solved through the presence of the rigid fibers providing the 3D architecture and the high level of porosity.

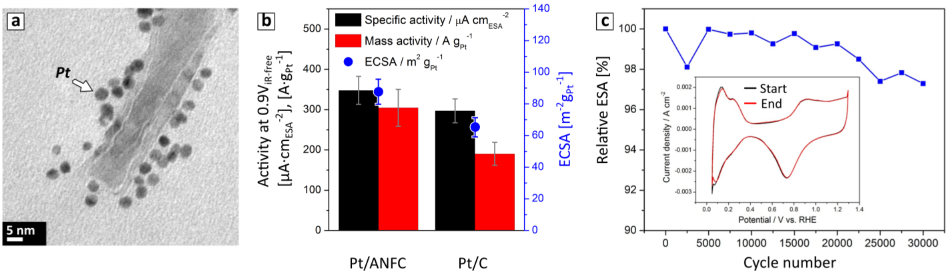

Figure 4.1 TEM observations of Pt nanoparticles on the surface of ANFC (a). Comparision of mass and surface activity of Pt/ANFC and Pt/C (b). Stability test, the degradation of electrochemical surface against the number of cycles (c): insert — two cyclic voltammograms (CV), at the beginning of the stability test (black line) and at the end of the test (red line). Adapted from [Paper III].

Paper II provides the detailed analysis of the prepared substrate covered by 1–3 layers of graphene and decorated by *Pt* and demonstrates that the electrochemical surface area (ESA) is in the range of 0.05–0.4 V_{RHE} for the developed material, which is larger than the reported for commonly used Pt/C. The difference in the potential at a half current between Pt/ANFC and Pt/C is around 22 mV. Therefore, a smaller driving force is needed to reduce the oxygen [Paper II]. Fig. 4.1a displays a specific activity and a mass activity specified from the kinetic current obtained at 1600 rpm in O_2 saturated 0.1 M $HClO_4$ and ECSA [Paper II].

Good stability is explained by the relatively high (75 %) content of the sp^2 hybridized carbon atoms (Fig.5b in [Paper II]), while for an activated carbon, the sp^3 hybridization is typical [62], and the electrochemical degradation of carbon is more prone at sp^3 sites rather than at sp^2 [63]. Therefore, a material possessing all properties required for serving as a highly stable electrocatalyst support is developed [Paper II]. This graphene encapsulated and platinizing hybrid fibers network has a straightforward applications in imminent catalyst nanostructures.

4.2 Electroconductive fillers for composites

The research area of graphene added composites is now quite mature [64–66]. However, the benefits offered by nanocarbon-based fillers is hindered by problems with agglomeration and poor dispersity in the host matrix. For the first time, the novel approach to electroconductive nano-fillers for otherwise dielectric materials has been proposed in [Paper IV].

The thermal analysis and Raman spectroscopy of the graphenated alumina nanofibers produced with no foliates on the several graphene layers are detailed in [Paper IV]. The HR-TEM micrograph, Fig. 4.2, reveals that the core-shell structured hybrid fillers are composed of 2–3 layers of graphene on alumina core fiber. Raman spectrum, obtained from the fibers subjected to ball milling, confirms integrity of the carbon layers on the surface. The distinguishing features of sp^2 carbon are the G and the D bands at around 1350 and 1580 cm^{-1}, respectively [57, 67]. Four well-recognized peaks around 1340 cm^{-1}, 1600 cm^{-1}, 2680 cm^{-1} and 2930 cm^{-1} are clearly identified together with an additional weak peak at 3180 cm^{-1} [IV]. Relatively narrow bands point to the nanocrystalline structure of the carbon.

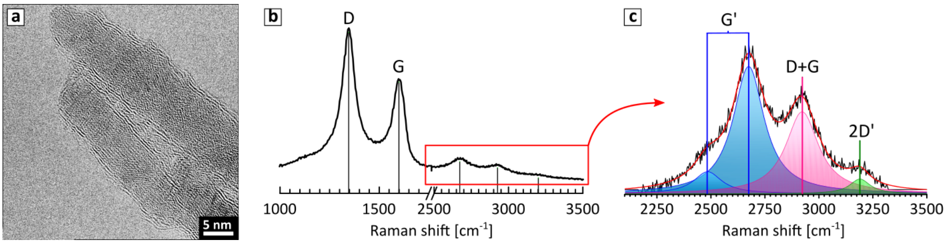

Figure 4.2 (a) HR-TEM image of the nanofibers covered by few graphene layers; (b) Raman spectrum of ANFCs, (c) the Raman shift in range from 2000 to 3500 cm^{-1}. Adapted from [Paper IV].

The dried suspension of the alumina and fillers represents a homogeneous mixture of the nanofibers within the ceramic matrix, Fig. 4.3, providing clear evidence of good dispersion of the nanofibers within the matrix. The alumina and partially stabilized zirconia based nanocomposites were consolidated by spark plasma sintering technique as described in [IV,A,B,E]. The Raman spectrum confirmed the structural integrity of the graphene in the alumina matrix after sintering as demonstrated in Fig. 4.3b.

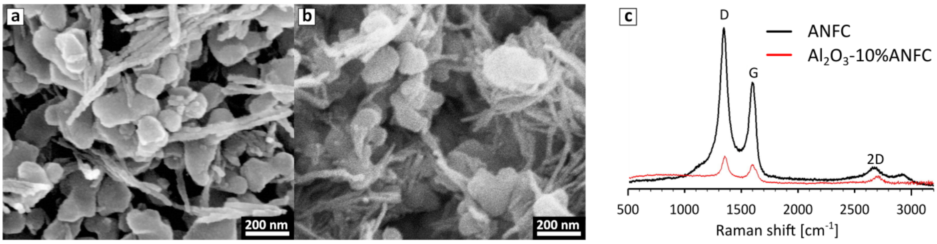

Figure 4.3 SEM images of composite powders with (a) 5 wt.%, and (b) 15 wt.% of ANFC in alumina matrix, (c) Raman spectrum of ANFC and sintered Al_2O_3-10 wt.% ANFC composite. Adapted from [A].

Sintered materials demonstrated significant increase in electroconductivity at as low load of graphene as 0.3 wt% for alumina-based composites and 0.34 wt% for zirconia based composites. An increase in electroconductivity of several order of magnitude is illustrated in Fig. 4.4a-b. This fact confirms the feasibility of the developed nanostructures of the graphenated alumina nanofibers as nanofillers for enhancing electrical response of otherwise dielectric ceramic matrices.

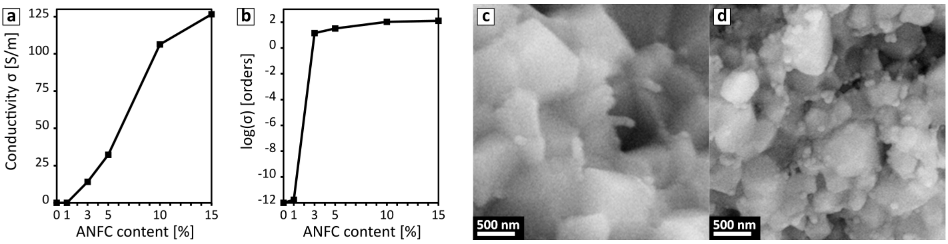

Figure 4.4 Dependence of sintered samples electrical conductivity from ANFC content in linear (a) and logarithmic (b) scale. SEM images of sintered materials with 5 wt% (c) and 15 wt% (d) of ANFC content. Adapted from [A]

4.3 Scaffolds for bio-application

Micro-environmental control of stem cell fate is of primary importance in tissue engineering and regenerative medicine. Recently it was proved that topography of the culture substrate or scaffold may affect stem cell differentiation. The highly aligned 3D network represents a great opportunity for tissue engineering [68]. The main role of the scaffold is to provide a structurally relevant 3D environment that allows the cells adherence. For a scaffold to be successful there is a set of key characteristics: (a) to be highly porous to allow for both cell penetration and mass transport; (b) to have the mechanical properties to match the application; and (c) to be biocompatible [69, 70]. Biomimetic scaffolds might reproduce the structure of natural extracellular matrix [71]; moreover, 3D conduits facilitate nerve regeneration [72]. As summarized in [73] ”Clinical evidence suggests that nano- and microtopography incorporated into scaffolds is a prerequisite for meaningful restoration of nerve function”. There are currently three major ways to fabricate nanofibrous scaffolds: self-assembly, electrospinning, and phase separation. Each has its own processing capabilities, advantages, and disadvantages. The developed substrates for cells differentiation and growth based on the biocompatible and chemically stable network of ANFC represents the significant breakthrough in biotechnology [Paper V]. Using our graphene augmented inorganic nanofibers (GAIN) scaffolds, an efficient neuronal differentiation of the stem cells has been demonstrated for the first time.

Figure 4.5 schematically shows a process of producing specifically oriented supports for cells growth. The horizontal orientation of the fibers tolerates preferable orientation and varying morphology of different types of cells. The vertical orientation of the fibers in the scaffold allows development of mixed tumour model.

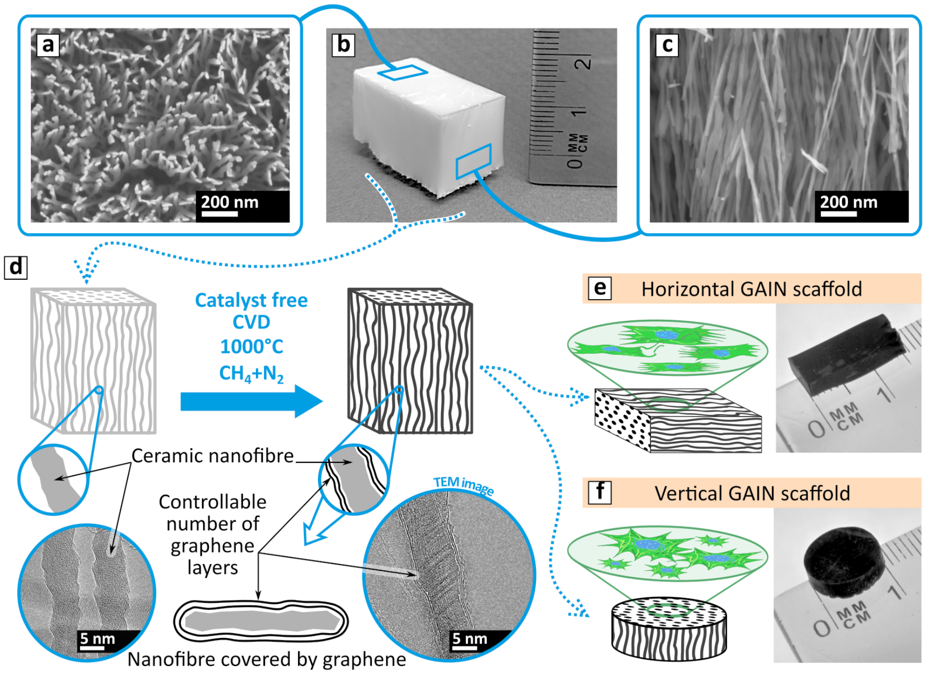

Figure 4.5 (a-c) The images of GAIN scaffolds: (a) the SEM top view; (b) the network of the highly oriented nanofibres; (c) the SEM side view. (d) The schematic of the CVD process. (e) The GAIN scaffold with horizontally oriented fibres. (f) The GAIN scaffold with vertically oriented fibres allowing development of mixed tumour in vitro models. Adapted from [Paper V].

For *in vitro* study, adipose derived human mesenchymal stem cells (MSC) were selected. The effect of the GAIN scaffolds on cell shape without deterioration of their normal growth has been obviously demonstrated [Paper V]. Furthermore, elongated morphology of human MSC and its high polarization create prerequisites for the preferential specific differentiation [Paper V]. Analysis of an inflammatory response indicates an immune tolerance of the GAIN scaffolds [Paper V].

The expression levels of Nestin by MSCs grown on the horizontal GAIN scaffolds substrate reveal continuous increase after three days of the tests unlike a reference glass substrate demonstrating decrease in Nestin, Figure 4.6. Nestin is an intermediate filament protein originally described as a marker of neural stem cells [74], but it is also expressed in a wide variety of different cell types and is regarded as a marker of MSCs [75].

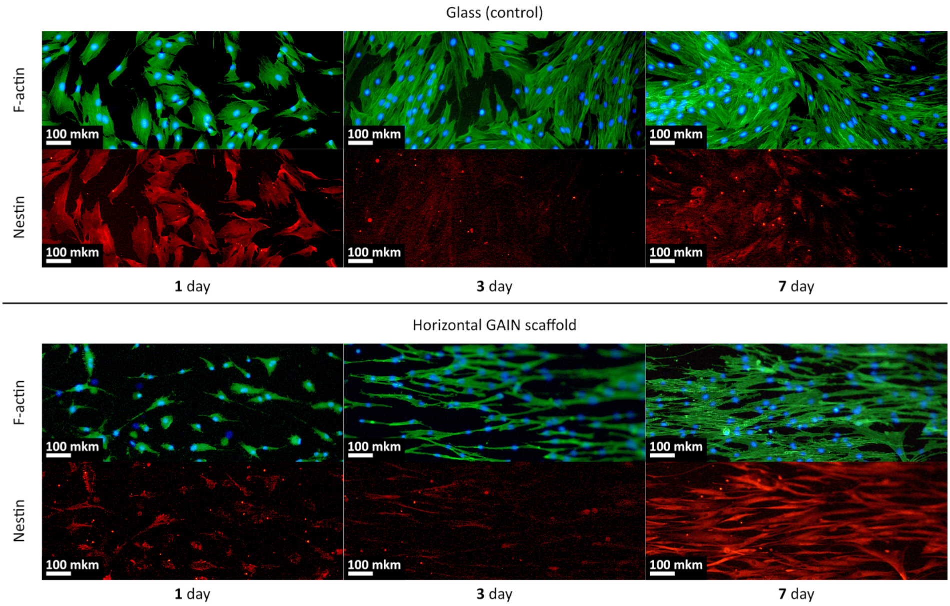

Figure 4.6 Immunofluorescence images of MSCs grown on glass (control) and horizontal GAIN for 1, 3 and 7 days. Cells are stained by phalloidin (green) and nestin (red). Nuclei are stained by Hoescht (blue).

Altogether, GAIN scaffolds actively influence the morphology of the cells, alignment, and adhesion, and is capable of guiding the MSCs differentiation towards neural lineages.

4.4 Sensors for bio-analytes

Ascorbic acid (AA), dopamine (DA), and uric acid (UA) are compounds of primary importance in bio- and medical sciences. All these bio-molecules play a fundamental role in human metabolism [76] and co-exist in physiological fluids [77]. Ascorbic acid is a powerful antioxidant needed to cure cancer, scurvy, colds, and many other diseases [78]; dopamine is one of the most vital neurotransmitters controlling functions of the central nervous system [79]; uric acid is the primary product of purine metabolism indicating gout, hyperuricemia and other diseases [80].

The development of a technique for simultaneous detection of all three compounds is essential for diagnose of relevant health problems. However, the electrochemical oxidation potentials of AA, DA, and UA are overlapped and responses are influenced by the presence of other bio-species [13, 81]. Extensive efforts have been made in order to overcome these problems [82, 83]. Carbon nanostructures and, especially, graphene have shown remarkable charge-transfer properties and suitable chemical stability [84].

In this work, combination of the unique electronic properties of graphene with a large surface area of self-organized nanofibers, a sensor, made out of highly foliated graphene deposited onto fibers surfaces, was developed for effective simultaneous determination of bio-analytes AA, DA, and UA [D,G]. Schematic representation of the process of sensor preparation and developed nanostructure are shown in Fig. 4.7 The distinguishing point is that the hybrid nanofibers are produced with no catalysts, which could affect the limit of detection.

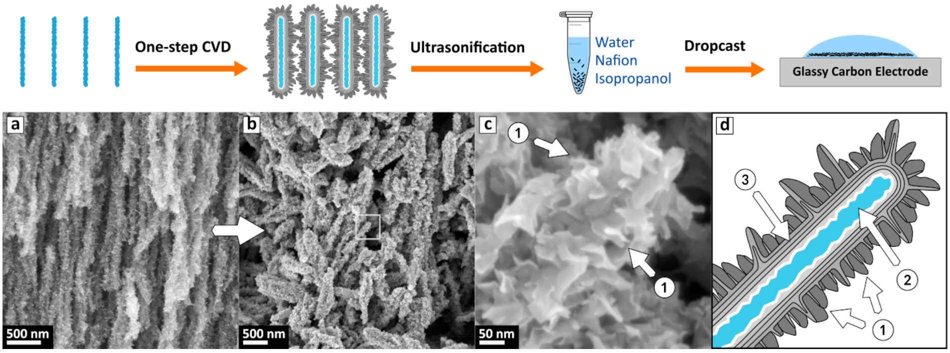

Figure 4.7 The upper part of the figure represents the steps of sensor preparation. SEM image of fibrous substrate with $\Delta W=700$ *% (a). SEM image of the mixture of the ANFC (b). A magnified HR-SEM image of a typical constituent of the mixture (c), where ① indicates graphene flakes. Schematic of the nanostructure (d), where ① graphene flakes, ② ceramic core nanofiber, and ③ graphene layers grown perpendicular to substrate.*

Electrochemical measurements, i.e. cyclic voltammetry and differential pulse voltammetry, were performed in a potentiostat/galvanostat Autolab PGSTAT30 in a standard three-electrode electrochemical cell [G]. A polished glassy carbon disk electrode (GCE) modified by nanofibers mixture and a saturated calomel electrode (SCE) were utilized for testing electrochemical activity of the developed structures. For the substrate with a weight gain $\Delta W=700$ %, density of the foliates was calculated to be 50 ± 10 per micron length of the fiber. An average diameter of the fiber after treatment was 45 ± 10 nm providing a specific surface area of 120 m^2g^{-1} (BET).

Figure 4.8 demonstrates electrocatalytic activity of the ANFC decorated electrode by addition of AA, DA and UA in 0.1 M pH 7.0 phosphate buffer solution in the range from –0.3 to 1 V. The voltammetric responses of the bio-analytes AA, DA and UA exhibit the well-defined and resolved oxidation peaks at –60 mV, 210 mV and 320 mV, respectively. Therefore, the developed sensor demonstrates a good selective electrocatalytic performance and can be successfully used for the simultaneous detection of three bio-species.

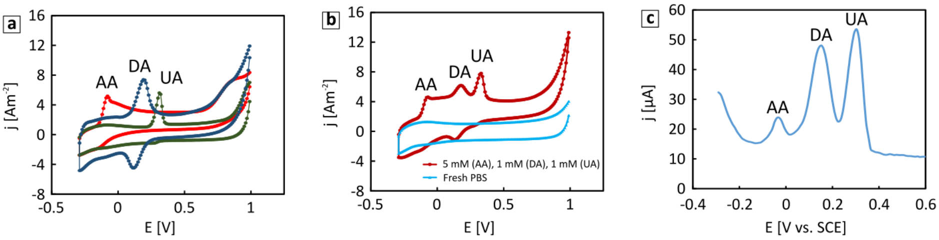

Figure 4.8 CV responses of (a) individual sensing of 5mm AA, 1 mM DA, and 1 mM UA; (b) ternary mixture of 5 mM AA, 1 mM DA, and 1mM UA in 0.1 M phosphate buffer solution (pH 7.0) at 10 mV·s^{-1}; DPV responses at (c) mixture of 50 μM AA, 60 μM DA, 50 μM UA in phosphate buffer solution (pH 7.0) at a scan rate of 10 mV·s^{-1}. Adapted from [G].

Differential pulse voltammetry (DPV) measurements, performed at the potential range from –0.3 to 0.5 V with a scan rate of 10 mV·s^{-1}, evaluate the sensitivity and the limit of detection for bio-analytes under consideration. Figure 4.8c shows the DPV profile of the mixture of bio-molecules demonstrating the negligible interference between AA, DA and UA. The limit of detection calculated from differential pulse voltammetry measurement was found to be 0.59 μM, 0.47 μM and 0.28 μM for ascorbic acid, dopamine, and uric acid, respectively. Table 4.1 compares the present study and some other works. It evidences that electrode prepared out of the developed graphenated nanostructures is a perspective material for highly sensitive and selective electrochemical sensors.

Table 4.1 Performance of different electrodes for simultaneous determination of AA, DA and UA [G].

	Linear range [μM]			Limit of detection [μM]			
Electrode	**AA**	**DA**	**UA**	**AA**	**DA**	**UA**	**Ref.**
Helical CNTs	7.5–180	2.5–105	6.7–65	0.92	0.8	1.5	[85]
Tryptophan-graphene	0.2–12.9	0.5-110	10–1000	10.09	0.29	1.24	[86]
SWCNH^{a}	30–400	0.2–3.8	0.06–10	5	0.06	0.02	[87]
N-doped graphene	5–1300	0.5–170	0.1–20	2.2	0.25	0.045	[88]
ANF-C700	**0.005–30**	**0.005–45**	**0.005–45**	**0.84**	**0.57**	**0.77**	[G]

^{a} Single-Walled Carbon NanoHorn

CONCLUSIONS

The present work was concentrated on the development of a cost-effective and environmentally friendly method of graphene growth on arbitrary ceramic surfaces at atmospheric pressure and relatively low temperatures by procedure. The main attention was paid onto nanostructural modifications of carbon layers encapsulating alumina nanofibers to ensure wide possible applications of the designed nanostructures. As a support for carbon deposition, the high-tech Estonian product — metal oxide nanofibers of a great aspect ratio was used for the first time.

Based on results of this study, the following conclusions can be drawn:

- The custom-made CVD set-up has been designed, worked out and successfully used for deposition of the carbon nanostructures, including graphene, onto the fibrous substrate;
- The bottom-up procedure of cost-effective single-step catalyst-free graphene growth on the ceramic substrate has settled;
- For the first time, the process of controllable deposition of carbon with tailored morphology, starting from a few layered smooth coatings and ending by highly foliated fuzzy nanostructures, has been developed;
- The parametric study has confirmed a decisive role of hydrogen in a gas mixture and a time of deposition;
- A material which offers tailorable density of graphitic edges, which is needed for a highly stable electrocatalyst support has been offered;
- Graphene encapsulated nanofibers have been used as fillers for manufacturing electroconductive ceramics with no deterioration in mechanical properties;
- For the first time, unique properties of scaffolds, based on graphenated nanostructures, have been used to provide an improved capacity in enhancing human mesenchymal stem cells alignment without any additional manipulations and a possible cells differentiation fate;
- The outstanding electrochemical stability of the platinized graphene encapsulated fibers and an improvement in the mass activity have confirmed applicability of the structures for electrochemical applications;
- Alumina nanofibers encapsulated by highly foliated multi-layered graphene have been used for a simultaneous detection of ascorbic and uric acids

together with dopamine. The developed sensor has demonstrated the superior electrocatalytic activities providing excellent selectivity and low detection limits towards this ternary mixture.

REFERENCES

[1] Vlassiouk, I., Fulvio, P., Meyer, H., Lavrik, N., Dai, S., Datskos, P., Smirnov, S., Large scale atmospheric pressure chemical vapor deposition of graphene. — *Carbon*, 2013, 54, 58–67, doi:10.1016/j.carbon.2012.11.003.

[2] Bianco, A., Cheng, H.-M., Enoki, T., Gogotsi, Y., Hurt, R. H., Koratkar, N., Kyotani, T., Monthioux, M., Park, C. R., Tascon, J. M., Zhang, J., All in the graphene family – A recommended nomenclature for two-dimensional carbon materials. — *Carbon*, 2013, 65, 1–6, doi:10.1016/j.carbon.2013.08.038.

[3] Novoselov, K. S., Geim, A. K., Morozov, S. V., Jiang, D., Zhang, Y., Dubonos, S. V., Grigorieva, I. V., Firsov, A. A., Electric Field Effect in Atomically Thin Carbon Films. — *Science*, 2004, 306(5696), 666–669, doi:10.1126/science.1102896.

[4] Sakhaee-Pour, A., Elastic properties of single-layered graphene sheet. — *Solid State Communications*, 2009, 149(1-2), 91–95, doi:10.1016/j.ssc.2008.09.050.

[5] Goenka, S., Sant, V., Sant, S., Graphene-based nanomaterials for drug delivery and tissue engineering. — *Journal of Controlled Release*, 2014, 173, 75–88, doi:10.1016/j.jconrel.2013.10.017.

[6] Ehrenfreund, P., Foing, B. H., Fullerenes and Cosmic Carbon. — *Science*, 2010, 329(5996), 1159–1160, doi:10.1126/science.1194855.

[7] Hot technologies. — *Nanotech inside*, 2012, 54(2).

[8] Geim, A. K., Kim, P., Carbon Wonderland. — *Scientific American*, 2008, 298(4), 90–97, doi:10.1038/scientificamerican0408-90.

[9] Huc, V., Bendiab, N., Rosman, N., Ebbesen, T., Delacour, C., Bouchiat, V., Large and flat graphene flakes produced by epoxy bonding and reverse exfoliation of highly oriented pyrolytic graphite. — *Nanotechnology*, 2008, 19(45), 455601, doi:10.1088/0957-4484/19/45/455601.

[10] Shukla, A., Kumar, R., Mazher, J., Balan, A., Graphene made easy: High quality, large-area samples. — *Solid State Communications*, 2009, 149(17-18), 718–721, doi:10.1016/j.ssc.2009.02.007.

[11] Stankovich, S., Dikin, D. A., Piner, R. D., Kohlhaas, K. A., Kleinhammes, A., Jia, Y., Wu, Y., Nguyen, S. T., Ruoff, R. S., Synthesis of graphene-based nanosheets via chemical reduction of exfoliated graphite oxide. — *Carbon*, 2007, 45(7), 1558–1565, doi:10.1016/j.carbon.2007.02.034.

[12] Hernandez, Y., Nicolosi, V., Lotya, M., Blighe, F. M., Sun, Z., De, S.,

McGovern, I. T., Holland, B., Byrne, M., Gun'Ko, Y. K., Boland, J. J., Niraj, P., Duesberg, G., Krishnamurthy, S., Goodhue, R., Hutchison, J., Scardaci, V., Ferrari, A. C., Coleman, J. N., High-yield production of graphene by liquid-phase exfoliation of graphite. — *Nature Nanotechnology*, 2008, 3(9), 563–568, doi:10.1038/nnano.2008.215.

[13] Wang, J., Liang, M., Fang, Y., Qiu, T., Zhang, J., Zhi, L., Rod-Coating: Towards Large-Area Fabrication of Uniform Reduced Graphene Oxide Films for Flexible Touch Screens. — *Advanced Materials*, 2012, 24(21), 2874–2878, doi:10.1002/adma.201200055.

[14] Liang, M., Wang, J., Luo, B., Qiu, T., Zhi, L., High-Efficiency and Room-Temperature Reduction of Graphene Oxide: A Facile Green Approach Towards Flexible Graphene Films. — *Small*, 2012, 8(8), 1180–1184, doi:10.1002/smll.201101968.

[15] Somani, P. R., Somani, S. P., Umeno, M., Planer nano-graphenes from camphor by CVD. — *Chemical Physics Letters*, 2006, 430(1-3), 56–59, doi:10.1016/j.cplett.2006.06.081.

[16] Wu, Z.-S., Ren, W., Gao, L., Liu, B., Jiang, C., Cheng, H.-M., Synthesis of high-quality graphene with a pre-determined number of layers. — *Carbon*, 2009, 47(2), 493–499, doi:10.1016/j.carbon.2008.10.031.

[17] Forbeaux, I., Themlin, J.-M., Debever, J.-M., Heteroepitaxial graphite on 6H-SiC(0001): Interface formation through conduction-band electronic structure. — *Physical Review B*, 1998, 58(24), 16396–16406, doi: 10.1103/PhysRevB.58.16396.

[18] Hass, J., de Heer, W. A., Conrad, E. H., The growth and morphology of epitaxial multilayer graphene. — *Journal of Physics: Condensed Matter*, 2008, 20(32), 323202, doi:10.1088/0953-8984/20/32/323202.

[19] Emtsev, K. V., Bostwick, A., Horn, K., Jobst, J., Kellogg, G. L., Ley, L., McChesney, J. L., Ohta, T., Reshanov, S. A., Röhrl, J., Rotenberg, E., Schmid, A. K., Waldmann, D., Weber, H. B., Seyller, T., Towards wafer-size graphene layers by atmospheric pressure graphitization of silicon carbide. — *Nature Materials*, 2009, 8(3), 203–207, doi:10.1038/nmat2382.

[20] Vázquez de Parga, A. L., Calleja, F., Borca, B., Passeggi, M. C. G., Hinarejos, J. J., Guinea, F., Miranda, R., Periodically Rippled Graphene: Growth and Spatially Resolved Electronic Structure. — *Physical Review Letters*, 2008, 100(5), 056807, doi:10.1103/PhysRevLett.100.056807.

[21] Wintterlin, J., Bocquet, M.-L., Graphene on metal surfaces. — *Surface Science*, 2009, 603(10-12), 1841–1852, doi:10.1016/j.susc.2008.08.037.

[22] Wang, Z., Li, N., Shi, Z., Gu, Z., Low-cost and large-scale synthesis of graphene nanosheets by arc discharge in air. — *Nanotechnology*, 2010, 21(17), 175602, doi:10.1088/0957-4484/21/17/175602.

[23] Wu, X., Liu, Y., Yang, H., Shi, Z., Large-scale synthesis of high-quality graphene sheets by an improved alternating current arc-discharge method. — *RSC Advances*, 2016, 6(95), 93119–93124, doi:10.1039/C6RA22273K.

[24] Kosynkin, D. V., Higginbotham, A. L., Sinitskii, A., Lomeda, J. R.,

Dimiev, A., Price, B. K., Tour, J. M., Longitudinal unzipping of carbon nanotubes to form graphene nanoribbons. — *Nature*, 2009, 458(7240), 872–876, doi:10.1038/nature07872.

[25] Tiwary, C., Javvaji, B., Kumar, C., Mahapatra, D., Ozden, S., Ajayan, P., Chattopadhyay, K., Chemical-free graphene by unzipping carbon nanotubes using cryo-milling. — *Carbon*, 2015, 89, 217–224, doi:10.1016/j.carbon.2015.03.036.

[26] Zhang, Y., Zhang, L., Zhou, C., Review of Chemical Vapor Deposition of Graphene and Related Applications. — *Accounts of Chemical Research*, 2013, 46(10), 2329–2339, doi:10.1021/ar300203n.

[27] Li, X., Cai, W., An, J., Kim, S., Nah, J., Yang, D., Piner, R., Velamakanni, A., Jung, I., Tutuc, E., Banerjee, S. K., Colombo, L., Ruoff, R. S., Large-Area Synthesis of High-Quality and Uniform Graphene Films on Copper Foils. — *Science*, 2009, 324(5932), 1312–1314, doi:10.1126/science.1171245.

[28] Sutter, P. W., Flege, J.-I., Sutter, E. A., Epitaxial graphene on ruthenium. — *Nature Materials*, 2008, 7(5), 406–411, doi:10.1038/nmat2166.

[29] Coraux, J., N‘Diaye, A. T., Busse, C., Michely, T., Structural Coherency of Graphene on Ir(111). — *Nano Letters*, 2008, 8(2), 565–570, doi: 10.1021/nl0728874.

[30] Muñoz, R., Gómez-Aleixandre, C., Review of CVD Synthesis of Graphene. — *Chemical Vapor Deposition*, 2013, 19(10-11-12), 297–322, doi:10.1002/cvde.201300051.

[31] Reina, A., Jia, X., Ho, J., Nezich, D., Son, H., Bulovic, V., Dresselhaus, M. S., Kong, J., Large Area, Few-Layer Graphene Films on Arbitrary Substrates by Chemical Vapor Deposition. — *Nano Letters*, 2009, 9(1), 30–35, doi:10.1021/nl801827v.

[32] Hofrichter, J., Szafranek, B. N., Otto, M., Echtermeyer, T. J., Baus, M., Majerus, A., Geringer, V., Ramsteiner, M., Kurz, H., Synthesis of Graphene on Silicon Dioxide by a Solid Carbon Source. — *Nano Letters*, 2010, 10(1), 36–42, doi:10.1021/nl902558x.

[33] Geim, A. K., Novoselov, K. S., The rise of graphene. — *Nature Materials*, 2007, 6(3), 183–191, doi:10.1038/nmat1849.

[34] Ismach, A., Druzgalski, C., Penwell, S., Schwartzberg, A., Zheng, M., Javey, A., Bokor, J., Zhang, Y., Direct Chemical Vapor Deposition of Graphene on Dielectric Surfaces. — *Nano Letters*, 2010, 10(5), 1542–1548, doi:10.1021/nl9037714.

[35] Novoselov, K. S., Fal′ko, V. I., Colombo, L., Gellert, P. R., Schwab, M. G., Kim, K., A roadmap for graphene. — *Nature*, 2012, 490(7419), 192–200, doi:10.1038/nature11458.

[36] Bonaccorso, F., Colombo, L., Yu, G., Stoller, M., Tozzini, V., Ferrari, A. C., Ruoff, R. S., Pellegrini, V., Graphene, related two-dimensional crystals, and hybrid systems for energy conversion and storage. — *Science*, 2015, 347(6217), 1246501–1246501, doi:10.1126/science.1246501.

[37] Yu, K., Lu, G., Bo, Z., Mao, S., Chen, J., Carbon Nanotube with Chemically

Bonded Graphene Leaves for Electronic and Optoelectronic Applications. — *The Journal of Physical Chemistry Letters*, 2011, 2(13), 1556–1562, doi:10.1021/jz200641c.

[38] Zeng, L., Lei, D., Wang, W., Liang, J., Wang, Z., Yao, N., Zhang, B., Preparation of carbon nanosheets deposited on carbon nanotubes by microwave plasma-enhanced chemical vapor deposition method. — *Applied Surface Science*, 2008, 254(6), 1700–1704, doi: 10.1016/j.apsusc.2007.07.131.

[39] Fan, Z., Yan, J., Zhi, L., Zhang, Q., Wei, T., Feng, J., Zhang, M., Qian, W., Wei, F., A Three-Dimensional Carbon Nanotube/Graphene Sandwich and Its Application as Electrode in Supercapacitors. — *Advanced Materials*, 2010, 22(33), 3723–3728, doi:10.1002/adma.201001029.

[40] Yu, D., Dai, L., Self-Assembled Graphene/Carbon Nanotube Hybrid Films for Supercapacitors. — *The Journal of Physical Chemistry Letters*, 2010, 1(2), 467–470, doi:10.1021/jz9003137.

[41] Yoo, E., Kim, J., Hosono, E., Zhou, H.-s., Kudo, T., Honma, I., Large Reversible Li Storage of Graphene Nanosheet Families for Use in Rechargeable Lithium Ion Batteries. — *Nano Letters*, 2008, 8(8), 2277–2282, doi:10.1021/nl800957b.

[42] Tung, V. C., Chen, L.-M., Allen, M. J., Wassei, J. K., Nelson, K., Kaner, R. B., Yang, Y., Low-Temperature Solution Processing of Graphene−Carbon Nanotube Hybrid Materials for High-Performance Transparent Conductors. — *Nano Letters*, 2009, 9(5), 1949–1955, doi:10.1021/nl9001525.

[43] Stoner, B. R., Raut, A. S., Brown, B., Parker, C. B., Glass, J. T., Graphenated carbon nanotubes for enhanced electrochemical double layer capacitor performance. — *Applied Physics Letters*, 2011, 99(18), 183104, doi:10.1063/1.3657514.

[44] Liyanage, L. S., Cott, D. J., Delabie, A., Elshocht, S. V., Bao, Z., Philip Wong, H.-S., Atomic layer deposition of high-k dielectrics on single-walled carbon nanotubes: a Raman study. — *Nanotechnology*, 2013, 24(24), 245703, doi:10.1088/0957-4484/24/24/245703.

[45] Stoner, B. R., Glass, J. T., Carbon nanostructures: A morphological classification for charge density optimization. — *Diamond and Related Materials*, 2012, 23, 130–134, doi:10.1016/j.diamond.2012.01.034.

[46] Ubnoske, S. M., Raut, A. S., Brown, B., Parker, C. B., Stoner, B. R., Glass, J. T., Perspectives on the Growth of High Edge Density Carbon Nanostructures: Transitions from Vertically Oriented Graphene Nanosheets to Graphenated Carbon Nanotubes. — *The Journal of Physical Chemistry C*, 2014, 118(29), 16126–16132, doi:10.1021/jp502317u.

[47] González, I., De Jesus, J., Cañizales, E., Bamboo-shaped carbon nanotubes generated by methane thermal decomposition using Ni nanoparticles synthesized in water–oil emulsions. — *Micron*, 2011, 42(8), 819–825, doi:10.1016/j.micron.2011.05.004.

[48] Parker, C. B., Raut, A. S., Brown, B., Stoner, B. R., Glass, J. T.,

Three-dimensional arrays of graphenated carbon nanotubes. — *Journal of Materials Research*, 2012, 27(07), 1046–1053, doi:10.1557/jmr.2012.43.

[49] Zheng, J., Ma, X., He, X., Gao, M., Li, G., Praparation, characterizations, and its potential applications of PANi/ graphene oxide nanocomposite. — *Procedia Engineering*, 2012, 27, 1478–1487, doi:10.1016/j.proeng.2011.12.611.

[50] Kutuzov, M., Method And System For Alumina Nanofibers Synthesis From Molten Aluminum. — 2013, uS Patent App. 13/756,366.

[51] Aghayan, M., Hussainova, I., Kirakosyan, K., Rodríguez, M. A., The template-assisted wet-combustion synthesis of copper oxide nanoparticles on mesoporous network of alumina nanofibers. — *Materials Chemistry and Physics*, 2017, 192, 138–146, doi:10.1016/j.matchemphys.2017.01.068.

[52] Aghayan, M., Hussainova, I., Gasik, M., Kutuzov, M., Friman, M., Coupled thermal analysis of novel alumina nanofibers with ultrahigh aspect ratio. — *Thermochimica Acta*, 2013, 574, 140–144, doi:10.1016/j.tca.2013.10.010.

[53] Vlassiouk, I., Regmi, M., Fulvio, P., Dai, S., Datskos, P., Eres, G., Smirnov, S., Role of Hydrogen in Chemical Vapor Deposition Growth of Large Single-Crystal Graphene. — *ACS Nano*, 2011, 5(7), 6069–6076, doi:10.1021/nn201978y.

[54] Losurdo, M., Giangregorio, M. M., Capezzuto, P., Bruno, G., Graphene CVD growth on copper and nickel: role of hydrogen in kinetics and structure. — *Physical Chemistry Chemical Physics*, 2011, 13(46), 20836, doi:10.1039/c1cp22347j.

[55] Zhang, X., Wang, L., Xin, J., Yakobson, B. I., Ding, F., Role of Hydrogen in Graphene Chemical Vapor Deposition Growth on a Copper Surface. — *Journal of the American Chemical Society*, 2014, 136(8), 3040–3047, doi:10.1021/ja405499x.

[56] Ferrari, A. C., Raman spectroscopy of graphene and graphite: Disorder, electron–phonon coupling, doping and nonadiabatic effects. — *Solid State Communications*, 2007, 143(1-2), 47–57, doi:10.1016/j.ssc.2007.03.052.

[57] Ferrari, A. C., Basko, D. M., Raman spectroscopy as a versatile tool for studying the properties of graphene. — *Nature Nanotechnology*, 2013, 8(4), 235–246, doi:10.1038/nnano.2013.46.

[58] Lui, C. H., Heinz, T. F., Measurement of layer breathing mode vibrations in few-layer graphene. — *Physical Review B*, 2013, 87(12), 121404, doi:10.1103/PhysRevB.87.121404.

[59] Sahoo, N. G., Pan, Y., Li, L., Chan, S. H., Graphene-Based Materials for Energy Conversion. — *Advanced Materials*, 2012, 24(30), 4203–4210, doi:10.1002/adma.201104971.

[60] Choi, H.-J., Jung, S.-M., Seo, J.-M., Chang, D. W., Dai, L., Baek, J.-B., Graphene for energy conversion and storage in fuel cells and supercapacitors. — *Nano Energy*, 2012, 1(4), 534–551, doi:10.1016/j.nanoen.2012.05.001.

[61] Mahmood, N., Zhang, C., Yin, H., Hou, Y., Graphene-based nanocomposites for energy storage and conversion in lithium batteries, supercapacitors

and fuel cells. — *Journal of Materials Chemistry A*, 2014, 2(1), 15–32, doi:10.1039/C3TA13033A.

[62] Stamatin, S. N., Borghei, M., Andersen, S. M., Veltze, S., Ruiz, V., Kauppinen, E., Skou, E. M., Influence of different carbon nanostructures on the electrocatalytic activity and stability of Pt supported electrocatalysts. — *International Journal of Hydrogen Energy*, 2014, 39(16), 8215–8224, doi:10.1016/j.ijhydene.2014.03.052.

[63] Speder, J., Zana, A., Spanos, I., Kirkensgaard, J. J., Mortensen, K., Arenz, M., On the influence of the Pt to carbon ratio on the degradation of high surface area carbon supported PEM fuel cell electrocatalysts. — *Electrochemistry Communications*, 2013, 34, 153–156, doi:10.1016/j.elecom.2013.06.001.

[64] Miranzo, P., Belmonte, M., Osendi, M. I., From bulk to cellular structures: A review on ceramic/graphene filler composites. — *Journal of the European Ceramic Society*, 2017, 37(12), 3649–3672, doi: 10.1016/j.jeurceramsoc.2017.03.016.

[65] Román-Manso, B., Chevillotte, Y., Osendi, M. I., Belmonte, M., Miranzo, P., Thermal conductivity of silicon carbide composites with highly oriented graphene nanoplatelets. — *Journal of the European Ceramic Society*, 2016, 36(16), 3987–3993, doi:10.1016/j.jeurceramsoc.2016.06.016.

[66] Ramesh, S., Khan, M. M., Alexander Chee, H., Wong, Y., Ganesan, P., Kutty, M., Sutharsini, U., Chew, W. K., Niakan, A., Sintering behaviour and properties of graphene oxide-doped Y-TZP ceramics. — *Ceramics International*, 2016, 42(15), 17620–17625, doi:10.1016/j.ceramint.2016.08.077.

[67] Ferrari, A. C., Meyer, J. C., Scardaci, V., Casiraghi, C., Lazzeri, M., Mauri, F., Piscanec, S., Jiang, D., Novoselov, K. S., Roth, S., Geim, A. K., Raman Spectrum of Graphene and Graphene Layers. — *Physical Review Letters*, 2006, 97(18), 187401, doi:10.1103/PhysRevLett.97.187401.

[68] Madurantakam, P. A., Cost, C. P., Simpson, D. G., Bowlin, G. L., Science of nanofibrous scaffold fabrication: strategies for next generation tissue-engineering scaffolds. — *Nanomedicine*, 2009, 4(2), 193–206, doi:10.2217/17435889.4.2.193.

[69] Niinomi, M., Metallic biomaterials. — *Journal of Artificial Organs*, 2008, 11(3), 105–110, doi:10.1007/s10047-008-0422-7.

[70] Ohtsuki, C., Kamitakahara, M., Miyazaki, T., Bioactive ceramic-based materials with designed reactivity for bone tissue regeneration. — *Journal of The Royal Society Interface*, 2009, 6(Suppl_3), S349–S360, doi:10.1098/rsif.2008.0419.focus.

[71] Kadler, K., Matrix loading: Assembly of extracellular matrix collagen fibrils during embryogenesis. — *Birth Defects Research Part C: Embryo Today: Reviews*, 2004, 72(1), 1–11, doi:10.1002/bdrc.20002.

[72] Jeffries, E. M., Wang, Y., Incorporation of parallel electrospun fibers for improved topographical guidance in 3D nerve guides. — *Biofabrication*, 2013, 5(3), 035015, doi:10.1088/1758-5082/5/3/035015.

[73] Spivey, E. C., Khaing, Z. Z., Shear, J. B., Schmidt, C. E., The fundamental role of subcellular topography in peripheral nerve repair therapies. — *Biomaterials*, 2012, 33(17), 4264–4276, doi:10.1016/j.biomaterials.2012.02.043.

[74] Lendahl, U., Zimmerman, L. B., McKay, R. D., CNS stem cells express a new class of intermediate filament protein.. — *Cell*, 1990, 60(4), 585–95.

[75] Xie, L., Zeng, X., Hu, J., Chen, Q., Characterization of Nestin, a Selective Marker for Bone Marrow Derived Mesenchymal Stem Cells. — *Stem Cells International*, 2015, 2015, 1–9, doi:10.1155/2015/762098.

[76] Argüello, J., Leidens, V. L., Magosso, H. A., Ramos, R. R., Gushikem, Y., Simultaneous voltammetric determination of ascorbic acid, dopamine and uric acid by methylene blue adsorbed on a phosphorylated zirconia–silica composite electrode. — *Electrochimica Acta*, 2008, 54(2), 560–565, doi:10.1016/j.electacta.2008.07.021.

[77] Ye, F., Feng, C., Jiang, J., Han, S., Simultaneous determination of dopamine, uric acid and nitrite using carboxylated graphene oxide/lanthanum modified electrode. — *Electrochimica Acta*, 2015, 182, 935–945, doi:10.1016/j.electacta.2015.10.001.

[78] Du, J., Yue, R., Ren, F., Yao, Z., Jiang, F., Yang, P., Du, Y., Novel graphene flowers modified carbon fibers for simultaneous determination of ascorbic acid, dopamine and uric acid. — *Biosensors and Bioelectronics*, 2014, 53, 220–224, doi:10.1016/j.bios.2013.09.064.

[79] Mo, J.-W., Ogorevc, B., Simultaneous Measurement of Dopamine and Ascorbate at Their Physiological Levels Using Voltammetric Microprobe Based on Overoxidized Poly(1,2-phenylenediamine)-Coated Carbon Fiber. — *Analytical Chemistry*, 2001, 73(6), 1196–1202, doi:10.1021/ac0010882.

[80] Zou, H. L., Li, B. L., Luo, H. Q., Li, N. B., A novel electrochemical biosensor based on hemin functionalized graphene oxide sheets for simultaneous determination of ascorbic acid, dopamine and uric acid. — *Sensors and Actuators B: Chemical*, 2015, 207, 535–541, doi:10.1016/j.snb.2014.10.121.

[81] Zhang, W., Yuan, R., Chai, Y.-Q., Zhang, Y., Chen, S.-H., A simple strategy based on lanthanum–multiwalled carbon nanotube nanocomposites for simultaneous determination of ascorbic acid, dopamine, uric acid and nitrite. — *Sensors and Actuators B: Chemical*, 2012, 166-167, 601–607, doi:10.1016/j.snb.2012.03.018.

[82] Yang, Y. J., Li, W., CTAB functionalized graphene oxide/multiwalled carbon nanotube composite modified electrode for the simultaneous determination of ascorbic acid, dopamine, uric acid and nitrite. — *Biosensors and Bioelectronics*, 2014, 56, 300–306, doi:10.1016/j.bios.2014.01.037.

[83] Zhang, Y., Yuan, R., Chai, Y., Zhong, X., Zhong, H., Carbon nanotubes incorporated with sol–gel derived La(OH)3 nanorods as platform to simultaneously determine ascorbic acid, dopamine, uric acid and nitrite. — *Colloids and Surfaces B: Biointerfaces*, 2012, 100, 185–189, doi:10.1016/j.colsurfb.2012.04.044.

[84] Xiao, C., Chu, X., Yang, Y., Li, X., Zhang, X., Chen, J., Hollow nitrogen-doped carbon microspheres pyrolyzed from self-polymerized dopamine and its application in simultaneous electrochemical determination of uric acid, ascorbic acid and dopamine. — *Biosensors and Bioelectronics*, 2011, 26(6), 2934–2939, doi:10.1016/j.bios.2010.11.041.

[85] Cui, R., Wang, X., Zhang, G., Wang, C., Simultaneous determination of dopamine, ascorbic acid, and uric acid using helical carbon nanotubes modified electrode. — *Sensors and Actuators B: Chemical*, 2012, 161(1), 1139–1143, doi:10.1016/j.snb.2011.11.040.

[86] Lian, Q., He, Z., He, Q., Luo, A., Yan, K., Zhang, D., Lu, X., Zhou, X., Simultaneous determination of ascorbic acid, dopamine and uric acid based on tryptophan functionalized graphene. — *Analytica Chimica Acta*, 2014, 823, 32–39, doi:10.1016/j.aca.2014.03.032.

[87] Zhu, S., Li, H., Niu, W., Xu, G., Simultaneous electrochemical determination of uric acid, dopamine, and ascorbic acid at single-walled carbon nanohorn modified glassy carbon electrode. — *Biosensors and Bioelectronics*, 2009, 25(4), 940–943, doi:10.1016/j.bios.2009.08.022.

[88] Sheng, Z.-H., Zheng, X.-Q., Xu, J.-Y., Bao, W.-J., Wang, F.-B., Xia, X.-H., Electrochemical sensor based on nitrogen doped graphene: Simultaneous determination of ascorbic acid, dopamine and uric acid. — *Biosensors and Bioelectronics*, 2012, 34(1), 125–131, doi:10.1016/j.bios.2012.01.030.

OTHER RELATED PUBLICATIONS

A Drozdova, M., Hussainova, I., Pérez-Coll, D., Aghayan, M., **Ivanov, R.**, Rodríguez, M.A., A novel approach to electroconductive ceramics filled by graphene covered nanofibers. — *Materials & Design*, 2016, 90, 291–298, doi:10.1016/j.matdes.2015.10.148

B Drozdova, M., Pérez-coll, D., Aghayan, M., **Ivanov, R.**, Rodríguez, M. A.; Hussainova, I., Hybrid graphene/alumina nanofibers for electrodonductive zirconia. — *Key Engineering Materials*, 2016, 674, 15–20, doi:10.4028/www.scientific.net/KEM.674.15

C Taleb, M., **Ivanov, R.**, Bereznev, S., Kazemi, S. H., Hussainova, I., Graphene-ceramic hybrid nanofibers for ultrasensitive electrochemical determination of ascorbic acid. — *Microchimica Acta*, 2017, 184, 897−905. doi:10.1007/s00604-017-2085-7

D Taleb, M., **Ivanov, R.**, Bereznev, S., Kazemi, S. H., Hussainova, I., Ultra-sensitive voltammetric simultaneous determination of dopamine, uric acid and ascorbic acid based on a graphene-coated alumina electrode. — *Microchimica Acta*, 2017, doi:10.1007/s00604-017-2510-y

E Hussainova, I., Drozdova, M., Aghayan, M., **Ivanov, R.**, Pérez-Coll, D., Graphene Covered Alumina Nanofibers as Toughening Agent in Alumina Ceramics. — *Advances in science and Technology*, 2014, 88, 49–53, doi:10.4028/www.scientific.net/AST.88.49

F Baronins, J., Antonov, M., **Ivanov, R.**, Shuliak, V., Hussainova, I., Effect of basalt and silica additives on erosive wear resistance of cast ceramics. — *Proceedings of the Estonian Academy of Sciences*, 2016, 65(2), 144–151, doi:10.3176/proc.2016.2.05

G Taleb, M., Hussainova, I., **Ivanov, R.**, Jasiuk, I., Graphenated ceramic nanofibers for highly sensitive simultaneous detection of dopamine, uric acid and ascorbic acid. — *Advanced Materials Letters*, 2017, 8(12), 1178–1183, doi:10.5185/amlett.2017.1557

H Patent application: Self-aligned fibrous scaffold for highly anisotropic cell cultures; Owner: Tallinn University of Technology; Authors: Irina Hussainova, Michael Gasik, **Roman Ivanov**; Priority number: US62/361,015; Priority date: 12.07.2016.

I Patent application: A ceramic composite material with funcionally graded properties; Owner: Tallinn University of Technology; Authors: Maria Drozdova, **Roman Ivanov**, Irina Hussainova; Priority number: P201700026; Priority date: 7.07.2017.

ACKNOWLEDGEMENTS

Firstly, I would like to express my sincere gratitude to my supervisor, Prof. Irina Hussainova for the guidance, continuous support and encouragement of my PhD study. Her patience, motivation and incredible working capacity made this work possible.

I am very thankfull to Ilja Anoshkin for his practical help in my initial experiments, wich became a good start for my work. Knowledge I gained thanks to him became extremely valuable in my studies. Also I would like to thank Albert Nasibulin who gave the opportunity to perform experiments in Aalto university.

As well want to express my gratitude to Serban Stamatin for his in-depth and comprehesensive investigations of developed hybrid materials, whose results inspired to continue and widen studies in this field.

I would like to thank Prof. Michael Gasik and Dr. Jekaterina Kazantseva for involving me into exiting research in the field of cell biology which opens new horizons for developed material applications and foreshadows many new discoveries in this direction.

I want to thank my collegues Masoud Taleb and Maria Drozdova for very useful discussions, fruitful common work, enjoyable working atmosphere and sharing their experience with me. Also I want to mention my collegues Janis Baroninš, Zorjana Mural, Marina Aghayan, Yaroslav Holovenko, Maria Fomitšenko, Nikhil Kumar Kamboj, Tatevik Minasyan and Ali Saffarshamshirgar and thank them for open, helpful and pleasant working environment which had a positive impact on the quality of the obtained results.

I would like to thank Mart Viljus and Olga Volobujeva for opportunity to recieve nice SEM images and especially many thanks to Valdek Mikli for, literally, infinite amount of SEM images, his explanations and willingness to help. I would like to express my gratitude to Taavi Raadik for opportunity to obtain Raman results, his help, explanations and comprehensive assistance.

I would like to express my appreciation to Alexey Garshev from Moscow State University for the superior TEM investigations, and special thanks to Denis Shabratov and Pavel Kudinski for providing such opportunities

Separate gratitude to Mikhail Kutuzov our industrial partner for inspiring topics to study, although not all of them became projects.

Finally, I am deeply grateful to Maksim Antonov for a lot of help, sharing of interesting ideas and endless philosophical discussions.

This work was supported by the Estonian Ministry of Higher Education and Research under projects PUT1063 ”Nanonet of ceramic fibers with targeted functionalities” (I. Hussainova), IUT19-29 ”Multi-scale structured ceramic-based composites for extreme applications”, Foundation Archimedes targeted grant AR12133 ”NanoCom”, and PROTOTRON program under ”ULTRINIA” and ”ViroGAIN” projects. And partially supported by ASTRA “TUT Institutional Development Programme for 2016-2022” Graduate School of Functional Materials and Technologies (2014-2020.4.01.16-0032).

ABSTRACT

Chemical Vapour Deposition of Graphene Coating onto Ceramic Nanofibers Substrates and Applications Thereof

Graphene is one of the youngest member in nanosized carbon materials which represents the basic building block for many others carbon structures. Due to its extraordinary properties, graphene is considered as a promising candidate to be used in highly demanding industrial fields. However, there is a series of obstacles to be overwhelmed on the way to full realization of potentials graphene may offer. Fundamentally, the high performance of any kind of system is closely related to the properties of materials it is fabricated out. Therefore, the procedure of materials fabrication plays one of the pivotal role in anticipated performance. Currently, one of the greatest challenges is a controllable deposition of graphene layers onto complex shape dielectric substrate in a reproducible manner.

The study focuses on the elaboration of novel hybrid materials based on the high-tech Estonian product — alumina nanofibers of huge aspect ratio of 10^7 and diameters of a single fiber either 7 or 40 nm. In this work, for the first time, the simple and scalable single-step catalyst-free procedure of chemical vapour deposition of tailorable carbon nanostructures on the network of self-organized nanofibers has been demonstrated. The routine for growth of peculiar carbon nanostructures directly on dielectric substrates opens new perspectives for making required materials with the specified density of graphene foliates. Variations in the process conditions, especially hydrogen concentration and time of reaction, were exploited to control the morphology and dimensionality of the deposited layers with a controllable density of foliates' edges. Edge density has a strong effect on charge concentration and activity in oxygen reduction reaction; therefore, different nanostructures may find applications in a wide variety of industrial fields.

In this work, the multifunctional hybrids have been developed to overcome the limitations of the existing materials for tough and electroconductive ceramic-matrix materials; highly sensitive sensors of biological liquids; electrochemical energy conversion; and scaffolds for bio-applications.

Such, the ability to transform an insulating ceramics into highly conductive ones by adding the graphenated nanofibers into the host matrix has been affirmed. Coupling between a few layered graphene and alumina nanofibers has resulted in the development of a novel type of electroconductive fillers for insulators,

which are able to modify the intrinsic electrical properties. The general strategy developed in this work opens a new avenue for processing of composites with electrical properties required for the electrical discharge machining.

The graphenated alumina nanofibers, representing ceramic fiber encapsulated by the conductive and inert few-layered graphene, is shown to be a promising material for electrochemical applications. This hybrid structure has demonstrated performance needed for a electrocatalyst support of Pt particles in fuel cells. Stability and unique structure offer new possibilities for application of these coated fibers in electrochemical energy conversion technologies.

Moreover, highly foliated fuzzy hybrid structures have shown intriguing application potential as the electrochemical sensors for low-limit and high-sensitivity detection of bio-analytes.

For the first time it was demonstrated that the graphenated alumina fibers three-dimensional (3D) customized scaffold is capable to modulate mesenchymal stem cells differentiation without additions of specific culture media, which may give new stimuli in cells manipulation and regenerative medicine.

KOKKUVÕTE

Grafeenpinde keemiline aursadestus keraamilistele nanokiududele ja nende kasutus

Grafeen on uusim süsiniknanomaterjal ja mitmete süsinikstruktuuride peamine koostisosa. Erakordsete omaduste tõttu peetakse grafeeni paljutõotavaks kandidaadiks väga nõudlikes tööstusvaldkondades kasutamiseks. Ometi tuleb grafeeni potentsiaali täielikuks avamiseks ületada veel palju takistusi. Põhimõtteliselt on mistahes süsteemi suutlikkus tihedalt seotud selle valmistamiseks kasutatud materjalide omadustega. Seetõttu on materjalide valmistamisel ülioluline oodatava suutlikkuse kujundamine. Praegusel ajal on üheks suuremaks probleemiks grafeenikihtide kontrollitav ja reprodutseeritav sadestamine keerulise kujuga dielektrilistele aluspindadele.

Käesolev uurimus keskendub selliste uudsete hübriidmaterjalide väljatöötamisele, mis põhinevad ainulaadtel Eestis toodetavatel alumiiniumoksiid nanokiududel. Nende kiudude pikkuse ja läbimõõdu suhe on hiigelsuur (10^7), üksiku kiu läbimõõt on juures 7 kuni 40 nm. Esmakordselt on demonstreeritud lihtsat ja skaleeritavat üheastmelist katalüsaatoriteta protseduuri, millega iseorganiseeruvate nanokiudude võrgustiku pinnale keemiliselt aurufaasist sadestatakse nanostruktuurid, mis on vastavalt vajadusele konstrueeritud süsinikust. Süsinikule eriomaste nanostruktuuride kasvatamine otse dielektrilisele aluspinnale avab uusi võimalusi vajaliku tihedusega grafeenikilniga kaetud materjalide valmistamisel. Sadestatud jaäb kuju ja mõõtmete ning pinde servade tiheduse kontrollitavuse saavutamiseks kasutati protsessitingimuste, eriti vesiniku kontsentratsiooni ja reaktsiooniaja varieerimist. Pinde servade tihedus mõjutab märgatavalt laengute kontsentratsiooni ja hapniku redutseerimise aktiivsust. See võimaldab kasutada mitmesuguseid nanostruktuure paljudes tööstusvaldkondades. Selle uurimistöö raames on töötatud välja olemasolevate materjalidega kaasnevaid piiranguid ületavad ja mitmeks otstarbeks sobivad hübriidmaterjalid, mida saab kasutada elektri juhtivate keraamilise maatriksiga sitkete materjalide, väga tundlike biovedelikuandurite, energia elektrokeemilise muundamise ja bioloogiliste tugistruktuuride jaoks.

Need materjalid tõestavad, et isoleerivate omadustega keraamilise maatriksi saab muuta hästijuhtivaks, kui sellele lisada grafeeniga kaetud nanokiude. Grafeenikihtide ja alumiiniumoksiid kiudude sidumise tulemusena on välja töötatud muidu isolaatorite uut tüüpi täiteained, mis juhivad elektrit ja on võimelised muutma neile omaseid elektrilisi omadusi. Väljatöötatud üldine protseduur avab uusi võimalusi elektroerosioontöötluseks sobivate omadustega komposiitide saamisel.

See uurimus näitab, et mõne inertse ja juhtiva grafeenikihiga kaetud keraamilised alumiiniumoksiidnanokiud on elektrokeemiarakenduste jaoks paljutõotav materjal. Demonstreeritud on sellise hübriidstruktuuri toimivust kütuseelementide plaatinaosakeste elektrokatalüütilisel toetamisel. Püsivus ja ainulaadne struktuur pakuvad uusi võimalusi sellise pindega kiudude kasutamiseks energia elektrokeemilisel muundamisel. Peale selle on kihistunud ja selgete piirjoonteta hübriidstruktuurid näidanud, et neil on huvipakkuvat potentsiaali suure tundlikkusega elektrokeemiliste anduritena, mis tuvastavad bioloogilisi analüüte ka väikese koguse korral.

Esima kordselt demonstreeriti, et grafeeniga kaetud alumiiniumoksiidkiudude kolmemõõtmeline struktuur suudab spetsiaalse söötme lisamiseta moduleerida mesenhümaalsete tüvirakkude diferentseerumist. See võib anda uusi stiimuleid rakkude manipuleerimisele ja regeneratiivmeditsiinile.

CURRICULUM VITAE

Personal data

Name	Roman Ivanov
Date of birth	07 24 1981
Place of birth	Tallinn, Estonia

Contact data

Address	Vikerlase 15–18, 13616 Tallinn, Estonia
Phone	+372 58416148
E-mail	roman.ivanov@ttu.ee, roman.ivanov@gmail.com

Education

Period	**Institution**	**Degree**
2013 – 2017	Tallinn University of Technology	PhD studies
2003 – 2005	National Research University of Electronic Technology (MIET) (Russia)	Master of Science
1999 – 2003	National Research University of Electronic Technology (MIET) (Russia)	Bachelor
1987 – 1999	Tallinn Central Russian Gymnasium	Highschool

Language competence

Russian	Native speaker
English	Good
Estonian	Average

Education

Period	**Organization**	**Position**
2008 – 2010	Nanojet company	AFM operator
2007 – 2009	Estonian Nanotechnology Competence Center	Researcher
2006 – 2007	MikroMasch company	Technical specialist

ELULOOKIRJELDUS

Isikuandmed

Nimi	Roman Ivanov
Sünniaeg	24 07 1981
Sünnikoht	Tallinn, Eesti

Contact data

Aadress	Vikerlase 15–18, 13616 Tallinn, Eesti
Telefon	+372 58416148
E-post	roman.ivanov@ttu.ee, roman.ivanov@gmail.com

Education

Periood	**Õppeasutus**	**Haridus**
2013 – 2017	Tallinna Tehnikaülikool	Doktoriõpe
2003 – 2005	Riiklik Elektroonilise Tehnoloogia Instituut (MIET) (Venemaa)	Magistrikraad
1999 – 2003	Riiklik Elektroonilise Tehnoloogia Instituut (MIET) (Venemaa)	Bakalaureusekraad
1987 – 1999	Tallinna Kesklinna Vene Gümnaasium	Keskharidus

Language competence

Vene keel	Emakeel
Inglise keel	Kesktase
Eesti keel	Algtase

Education

Periood	**Organisatsioon**	**Ametikoht**
2008 – 2010	Nanojet OÜ	AMF operaator
2007 – 2009	Eesti Nanotehnoloogiate Arenduskeskuse AS	Uurija
2006 – 2007	Mikromasch Eesti OÜ	Tehniline spetsialist

PUBLICATION I

Ivanov, R., Mikli, V., Kübarsepp, J., Hussainova, I., Direct CVD growth of foliated graphene closed shells on alumina nanofibers. — *Key Engineering Materials*, 2016, 674, 77–80, doi:10.4028/www.scientific.net/KEM.674.77

Key Engineering Materials Vol. 674 (2016) pp 77-80
© (2016) Trans Tech Publications, Switzerland
doi:10.4028/www.scientific.net/KEM.674.77

Submitted: 2015-05-07
Accepted: 2015-05-14

Direct CVD growth of multi-layered graphene closed shells around alumina nanofibers

Roman Ivanov[1,a *], Valdek Mikli[2,b], Jakob Kübarsepp[1,c]
and Irina Hussainova[1,3,c]

[1]Department of Materials Engineering, Tallinn University of Technology, Ehitajate 5, 19086, Tallinn, Estonia

[2]Department of Materials Science, Tallinn University of Technology, Ehitajate 5, 19086, Tallinn, Estonia

[3]ITMO University, Kronverksky 49, St. Petersburg, 197101, Russian Federation

[a]roman.ivanov@ttu.ee (corresponding author), [b]valdek.mikli@ttu.ee, [c]jakob.kubarsepp@ttu.ee, [c]irina.hussainova@ttu.ee

Keywords: Nanofibers, Alumina, Graphene, CVD, Raman spectroscopy.

Abstract. In this work, a catalyst-free direct deposition of multi-layered graphene closed shells around highly aligned alumina nanofibers with aspect ratio of 10^7 is demonstrated for the first time. A single – step chemical vapor deposition process of specified parameters was used for development of hybrid structures of carbon shells around the core alumina nanofibers. Transmission electron microscopy and Raman spectroscopy were used to confirm formation of graphene layers and to understand the morphology of the various structures. The developed routine for growth of peculiar carbon nanostructures opens new opportunities for deposition of the tailored carbon structures on dielectric substrates.

Introduction

One- and/or two-dimensional carbon forms are considered as materials for the next generation supercapacitors, fuel and solar cells, reinforcements in composites, etc. due to their unique properties. Utilization of various nanocarbon structures requires a procedure for preparation of different objects depending on their specific needs. Direct synthesis of tailored nanostructures with required morphology on an appropriate functional substrate is a fundamental goal. A method for direct CVD growth of tailorable number of graphene-like layers on insulating materials represents a challenge for future functional and structural applications [1]. Recent studies on growth of single-walled carbon nanotubes on oxide substrates have proved the suggestion that oxides can graphitize carbon [2]. Among other methods, the chemical vapor deposition (CVD) has been demonstrated as a suitable process for the cost effective synthesis of a metal-catalyzed growth of the large-area graphene sheets [3-5]. The electronic structure of the graphene is modified largely by hybridization of its π orbits with the d orbitals of the metal substrate. This results in a complicated procedure for removal of metal catalysts and transferring the graphene to dielectric substrates. Although great efforts were applied to explore the direct growth of graphene on dielectric substrates, the poor properties of the product produced with the help of a high temperature synthesis or a high-cost plasma enhanced chemical vapor deposition make the catalyst-free method to be challenging [6].

In this report, for the first time we demonstrate that alumina nanofibers (ANF) can successfully serve as a substrate for the direct growth of peculiar carbon nanostructures representing multi-layer graphene close shells with tailorable density of graphene foliates with open edges. We show that the catalyst free CVD method can be used to cover the dielectric fiber of tremendous aspect ratio (10^7) by different carbon nanostructures.

Experimental procedure

Materials. The fibers of gamma-alumina with average single-fiber diameters of 7 nm and length of 3–10 cm represent tight bundles consisting of several thousand nanofibers, Fig. 1a, with a specific surface area of 155-160 m^2g^{-1} (BET method). A bundle of the well-aligned alumina nanofibers were developed by a controlled liquid phase oxidation of aluminum melt [7,8]. Among variety of ceramic fibers available on market, alumina fibers have received a particular attention due to unique high-temperature properties and chemical stability.

Processing. Carbon deposition was carried out via one-step CVD process at temperature of 1000 ºC and atmospheric pressure in a flow of two gases: ethylene (C_2H_4) with a flow rate of 10 cm^3/min and hydrogen (H_2) with a flow rate of 360 cm^3/min. The substrate was placed into a crucible boat and introduced into the hot-wall CVD reactor with an inner diameter of a quartz tube of 12 mm. Time of synthesis was selected to be either 20 min (specimen of a "low carbon content" – LC) or 250 min (specimen of a "high carbon content" – HC). As a final step of the CVD process, the samples were cooled down to the room temperature in an argon flow (950 cm^3/min). The mass gain of the carbon-covered bundles was 13% and 171% for LC and HC specimens, respectively. Control of the deposition parameters was performed by ratio between a carbon source (ethylene) and hydrogen.

Characterization. The morphology of the hybrid structures was examined by scanning electron microscopy (SEM, Zeiss Gemini Ultra-55), optical microscopy (Leica DM4000) and high-resolution transmission electron microscopy (HRTEM, JEOL 2200-S, Japan). Raman spectra of the graphene layers on alumina substrates were obtained with Raman spectroscopy (Horiba Jobin Yvon LabRAM 300) with laser excitation energy of 514 nm that allows for the identification of single and few-layer graphene and other carbon allotropes [9-11].

Results and discussion.

Microstructure development. Figure 1 demonstrates the optical and SEM images of the hybrid structures of alumina nanofibers and carbon. Figure 2 a-d presents TEM images of the structures obtained.

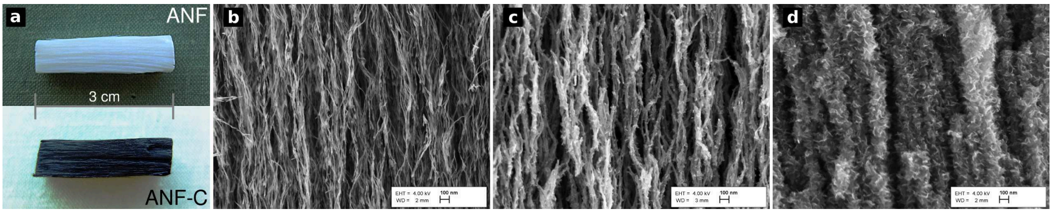

Figure 1. Optical and SEM images of alumina nanofibers: (a) The block of the substrate ANFs serving as a support for carbon structures growth – the upper image shows untreated block of fibers, and the bottom image demonstrates the fibers after CVD treatment; (b) SEM image of untreated fibers; (c) SEM image of the sample after 20 min of CVD treatment; (c) SEM image of ANFs covered by carbon nanostructures after 250 min of CVD treatment.

Several graphene layers with interspace of ca. 3 – 4 Å are folded around nanofibers along a longitudinal axis. The most influential factor in determining layer morphology during the parametric study was the time of treatment. By varying time, the resultant structure could consist of a few layered graphene sheets around the alumina nanofibers or highly foliated graphenated shells. Mass gain of 13% corresponds to 2 – 5 layers of relatively "smooth" graphene sheets. The carbon formed on the nanofibers during 250 min is rolled over the fibers with lots of admixture of the opened graphitic flakes developing the nanostructure of closed shell of graphene multi-layers and nanofoliates with the high density of open edges. Number of layers in a shell is increased up to 6 – 15. The schematic representation of the complex structures with divergent graphene-like carbon nanoflakes is shown in Figure 2e. The graphene foliates are randomly entangled and cross-linked on the surface of graphene.

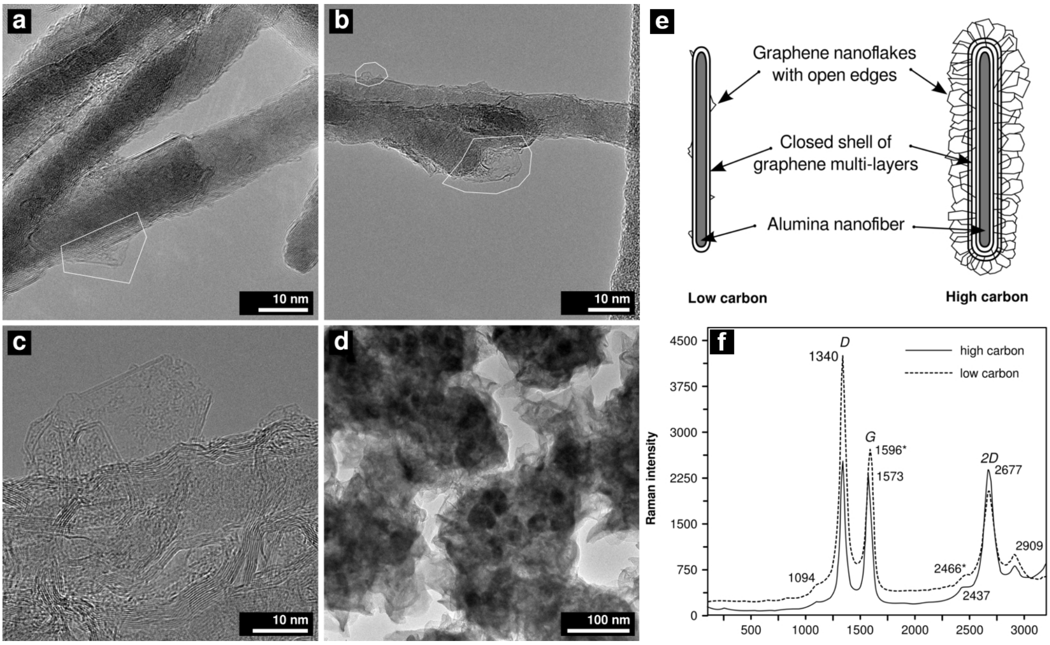

Figure 2. TEM images of ANF wrapped into multi-layered graphene shells: (a) and (b) “LC” sample with foliates outlined by polygons; (c) “HC” sample with the fridge of nanocarbon flakes; (d) top view of “HC” structures; (e) the schematic sketch of hybrid nanostructures; and (f) Raman spectra of the samples.

Raman spectroscopy. Figure 2f demonstrates the Raman spectra of the specimens providing additional information on structure of developed graphene layers. The Raman spectra exhibit the G peak and the D peak at around 1580 and 1350 cm^{-1}, respectively, and provide further confirmation of carbon formation. An intense and narrow G band, a weak D mode and a very intense 2D mode characterize the few-layered graphene. In our case, the intensity of G peak is lower as compared to the 2D peak at ca. 2700 cm^{-1}. However, the narrow bands suggest the layers and foliates possess nanocrystalline structure. The position of 2D band pointed at the presence of several layers of graphene [9]. The Raman modes reflect the main features observed for MWCNT [10]. Actually, carbon nanotubes are essentially rolled up graphene sheets and multi-walled tubes represent several layers of graphene wrapped around the core tube. The ratio between intensities of the D and G peaks, I_D/I_G, can be used for estimation of the amount of structural defects/edges and the degree of graphitization in graphitic materials [11]. The value of area-averaged I_D/I_G increases from ~1.05 to ~1.5 for samples HL and LC, respectively. The ratio evolution may be attributed to possible saturation in growth of the continuously folding carbon layers and an intensive growth of foliates. Because of large number of the edge planes in the direction parallel to incident polarization as well as the twisted graphitic planes of multi-layer graphene flakes, the I_D/I_G ratio is expectedly high. The ratio between intensities of the I_G and I_{2D} was calculated to be ~0.9 to ~1.12 for HC and LC specimens, respectively. Decrease in I_G/I_{2D} ratio for a longer treated sample suggests the presence of higher fraction of nano-foliates on the surface of the shell layers.

Conclusion.

In summary, we have demonstrated the direct catalyst – free one-step CVD growth of multi-layered graphene closed shells around highly aligned dielectric (alumina) nanofibers. This process was shown to be suitable for formation of either “smooth” a few-layered graphene closed shells or “graphenated” fuzzy shells with the high edge density of nano-foliates in dependence on the parameters of treatment. Further improvement in the control of the process parameters can lead to the direct deposition of the tailored graphenic structures for a large-scale use in different applications.

Acknowledgment

This work was supported by institutional research funding IUT 19-29 of the Estonian Ministry of Education and Research. Archimedes targeted grant AR12133 (NanoCom) is also gratefully appreciated for supporting this study. The authors would like to thank Prof. A. Nasibulin for helpful discussion on the topic.

References

[1] A. Ismach, C. Druzgalski, S. Penwell, A. Schwartzberg, M. Zheng, A. Javey, J. Bokor, Y. Zhang, Direct Chemical Vapor Deposition of Graphene on Dielectric Surfaces, Nano Lett. 10 (2010) 1542-1548.

[2] M.H. Rümmeli, A. Bachmatiuk, A. Scott, F. Bornert, J.H. Warner, et al. Direct low temperature nano-graphene synthesis over a dielectric insulator, ACS Nano 4 (2010) 4206.

[3] R. Muñoz, C. Gómez-Aleixandre, Review of CVD Synthesis of Graphene, Chem. Vap. Deposition 19 (2013) 297-322.

[4] S. Bhaviripudi, X. Jia, M.S. Dresselhaus, J. Kong, Role of kinetic factors in chemical vapor deposition synthesis of uniform large area graphene using copper catalyst, Nano Lett. 10 (2010) 4128-33.

[5] T. Lin, F. Huang, D. Wan, H. Bi, X. Xie, M. Jiang, Self-regulating homogenous growth of high-quality graphene on Co–Cu composite substrate for layer control, Nanoscale 5 (2013) 5847-53.

[6] C. Yang, H. Bi, D. Wan, F. Huang, X. Xie, M. Jiang, Direct PECVD growth of vertically erected graphene walls on dielectric substrates as excellent multifunctional electrodes, J. Mater. Chem. A 1 (2013) 770-5.

[7] M. Aghayan, I. Hussainova, M. Gasik, M. Kutuzov, M. Friman, Coupled thermal analysis of novel alumina nanofibers with ultrahigh aspect ratio, Thermochim. Acta 574 (2013) 140-144.

[8] R. Ivanov, I. Hussainova, M. Aghayan, M. Drozdova, D. Perez-Coll, M.A. Rodriguez, F. Rubio-Marcos, Graphene encapsulated oxide nanofibers as a novel type of nanofillers for electroconductive ceramics, Materials Letters (submitted) (2015)

[9] A.C. Ferrari, D.M. Basko, Raman spectroscopy as a versatile tool for studying the properties of graphene, Nat. Nanotechnol. 8 (2013) 235-246.

[10] L. Bokobza, J.-L. Bruneel, M. Couzi, Raman spectroscopic investigation of carbon-based materials and their composites. Comparison between carbon nanotubes and carbon black, Chem. Phys. Lett. 590 (2013) 153-159.

[11] C. Casiraghi, A. Hartschuh, H. Qian, S. Piscanec, C. Georgi, A. Fasoli, K.S. Novoselov, D.M. Basko, A.C. Ferrari, Raman Spectroscopy of Graphene Edges, Nano Lett. 9 (2009) 1433-1441.

PUBLICATION II

Hussainova, I., **Ivanov, R.**, Stamatin, S.N., Anoshkin, I.V., Skou, E.M., Nasibulin, A.G., A few-layered graphene on alumina nanofibers for electrochemical energy conversion. — *Carbon*, 2015, 88, 157–164, doi:10.1016/j.carbon.2015.03.004

CARBON 88 (2015) 157–164

Available at www.sciencedirect.com

ScienceDirect

journal homepage: www.elsevier.com/locate/carbon

A few-layered graphene on alumina nanofibers for electrochemical energy conversion

Irina Hussainova [a,b], *Roman Ivanov* [a], *Serban N. Stamatin* [c], *Ilya V. Anoshkin* [d,e], *Eivind M. Skou* [c], *Albert G. Nasibulin* [d,f,*]

[a] *Department of Materials Engineering, Tallinn University of Technology, Ehitajate 5, 19086 Tallinn, Estonia*
[b] *ITMO University, Kronverkskiy 49, St. Petersburg 197101, Russia*
[c] *Institute of Chemical Engineering, Biotechnology and Environmental Technology, University of Southern Denmark, Niels Bohrs Alle, 1, DK-5230 Odense M, Denmark*
[d] *Department of Applied Physics, Aalto University School of Science, Puumiehenkuja 2, 00076 Espoo, Finland*
[e] *Department of Radio Science and Engineering, P.O. Box 13000, 00076 Espoo, Finland*
[f] *Skolkovo Institute of Science and Technology, 100 Novaya Str., Skolkovo, Moscow Region 143025, Russia*

ARTICLE INFO

Article history:
Received 7 January 2015
Accepted 2 March 2015
Available online 7 March 2015

ABSTRACT

A few-layered graphene on the surface of highly aligned alumina nanofibers (ANFs) with an aspect ratio of 10^7 was synthesized in a single-step catalyst-free direct chemical vapor deposition process. The product, graphenated alumina nanofibers (G-ANFs), consisting of the ceramic nanofibers surrounded by the conductive and inert few-layered graphene, is a promising material for electrochemical applications. The synthesized material has been demonstrated to be an excellent electrocatalyst support for Pt particles in fuel cells. A 1.5-fold improvement in the mass activity has been obtained for Pt/G-ANF in comparison to the commercially available Pt/C. The electrochemical stability was found to be outstanding for acidic medium electrochemistry. Their remarkable stability and unique structure opens a new avenue for the use of this material in various electrochemical energy conversion technologies.

1. Introduction

Over the past several years, carbon nanomaterials have been attracting significant interest of a research community in attempts to develop alternative and environmental friendly energy sources. Carbon nanotubes (CNTs) and graphene are considered to be materials for the next generation supercapacitors, fuel and solar cells as well as lithium rechargeable batteries [1–5] due to their unique electrical properties [6,7]. New horizons in graphene-based materials applications have inspired innovations in methods and devices for energy conversion and storage. Fundamentally, the reliability of these systems is strongly dependent on materials used for their production. Nowadays a wide variety of emerging carbon materials with tailored nanostructures has been continuously developing for applications in energy related systems. Utilization of carbon nanostructures for a wide variety of applications requires a procedure for preparation of different objects depending on their specific needs. Direct synthesis of tailored carbon forms with required morphology on an appropriate functional substrate is a fundamental goal of the nanostructured carbon roadmap.

---

* *Corresponding author at:* Skolkovo Institute of Science and Technology, 100 Novaya Str., Skolkovo, Moscow Region 143025, Russia.
E-mail address: a.nasibulin@skoltech.ru (A.G. Nasibulin).

http://dx.doi.org/10.1016/j.carbon.2015.03.004
0008-6223/

The specific capacitance of carbon forms is generally influenced by their three-dimensional organization. Three-dimensional (3D) structures of graphenated CNTs representing graphene foliates along the length of the vertically aligned CNTs have recently shown enhanced electrochemical capacitance [8]. However, even well-aligned CNTs with primarily basal plane exposure as well as graphenated CNTs with both edge and basal plane exposure have a tendency to agglomerate. Therefore, a lower specific capacitance would be expected as compared to stiff structure with high edges density providing greater ability to control the geometrical framework [8,9]. Graphene has exhibited both enhanced activity and durability as a fuel cell catalyst support and extraordinary modification in properties of platinum (Pt) cluster electrocatalysts [1,10]. The main prerequisites for carbon materials to be considered as an electrocatalyst support are robustness and stability under potential cycling in acidic medium. An electrochemically stable carbon structure should provide a large amount of graphitic domains [11] to maximize the activity of Pt and minimize its content. A hybrid structure consisting of graphitic foliates grown along the aligned multi-walled CNTs has recently demonstrated a potential to have significant impact in charge storage and relative applications [9]. A key bottleneck in commercialization of electrochemical energy conversion devices is the electrocatalyst activity and stability. Latest studies showed that metal nanoparticles tend to self-organize on graphene-like materials maximizing the surface for electrocatalytic activity [12]. CNTs showed an increased electrochemical stability when compared to activated carbon [13]. Moreover, metal nanoparticles are stabilized at the metal oxide–graphene interface, improving considerably the electrochemical stability [14]. Therefore, it is likely that the metal–metal oxide–graphene junction will provide the needed electrochemical stability, which might boost the commercialization of electrochemical energy conversion devices. Graphene can not only be used as a carbon support for electrocatalysis but also be used effectively to reduce the Pt loading and, therefore, reduce the cost of a final product and its availability.

Graphene sheets of different sizes and defect level can be prepared by various methods, including manual mechanical cleavage of graphite with adhesive tape, epitaxial growth on single SiC crystal, chemical vapor deposition (CVD) on metal surfaces, *etc.* [15]. Graphenated nanostructures can be readily grown using different chemical vapor deposition approaches employing microwave plasma [9], radio frequency inductively coupled plasma, hot filament plasma, *etc.* [16]. The ability to synthesize graphene or a few-layered graphene flakes or even carbon nanowalls directly on insulating materials crucially removes the step of transferring the graphene after synthesis and can remove the need for large-area synthesis as required with metal substrates [16]. Recent studies on growth of single-walled carbon nanotubes on oxide substrates of silica, alumina and zirconia have proved the suggestion that oxides can graphitize carbon [17,18].

In this report, for the first time we demonstrate that alumina nanofibers (ANFs) can successfully serve as a substrate for the direct non-catalyst synthesis of a few-layered graphene. This 3D conductive, inert and relatively rough structure of graphenated wraps around the metal oxide nanofibers is an excellent support to immobilize the catalyst. Here, we show one of the potential uses of this material for the electrochemical energy conversion.

2. Experimental

2.1. Materials

The synthesis of the hybrid nanostructures on the surface of ANFs was carried out through a simple one-step chemical vapor deposition (CVD) process at atmospheric pressure. The aluminum oxide (Al_2O_3) nanofibers with the diameter of 7 nm represent a unique product with a very high and controllable anisotropy developed by controlled liquid phase oxidation of aluminum melt [19]. The crystal growth from a metal melt is an excellent technique to fabricate nanomaterials because of low cost, high yield and the ability to achieve high purity of the oxide structures in the as-synthesized state.

For the carbon nanostructure synthesis, the bundle of ANFs was placed in a crucible boat and introduced into the CVD reactor with a quartz tube with an inner diameter of 12 mm, then annealed at the temperature of 1000 °C during 3 min in an air atmosphere. The air in the reactor was replaced with nitrogen for 5 min with a gas flow rate of 1000 $cm^3 min^{-1}$ and further the process was performed at the temperature of 1000 °C in the atmosphere of two gases: methane (CH_4) with the flow rate of 50 $cm^3 min^{-1}$ and nitrogen (N_2) with the flow rate of 500 $cm^3 min^{-1}$ for elimination of the products of reaction. Time of the synthesis was selected to be 20 min resulting in the mass gain of the carbon of 14% ± 2%. As a final step of the CVD process, a delivery of methane was discontinued while nitrogen gas flow was increased up to 3000 $cm^3 min^{-1}$ followed by samples cooling down to the room temperature.

For platinization of the graphenated ANFs (G-ANF), a modified polyol synthesis was used as described elsewhere [20]. Briefly, 30 ml of ethylene glycol (99%, VWR) containing 4.8 mM K_2PtCl_4 (46.75% Pt, Alfa-Aesar) and 3 mM polyvinylpyrrolidone with $M_W = 55{,}000$ (Sigma Aldrich) was stirred for 20 min, turning to a pale-yellow solution. The mixture was then pretreated for 3 h at 160 °C under Ar flow. Then, after cooling to room temperature, 150 mg of G-ANF was added into the vessel along with 250 ml of acetone (99%, VWR) and magnetic stirred for 12 h. Hundred milliliters of ultrapure water (>18.2 MΩ, Millipore) was added to the obtained solution of 20 wt.% Pt on G-ANF and six times centrifuged at 4500 rcf for 10 min each cycle. In the final step, the obtained material was heat-treated at 200 °C for 12 h.

2.2. Characterization

The microstructural characterization methods include scanning electron microscopy (SEM, Zeiss Gemini Ultra-55), optical microscopy (Leica DM4000) and high-resolution transmission electron microscopy (HRTEM, JEOL 2200-S, Japan). The Raman spectroscopy (Horiba Jobin Yvon LabRAM 300 spectrometer equipped with a 514 nm laser), which is a powerful method for the analysis of graphitic materials

[21–26], was used for identification of structural features of the graphitic materials. X-ray Photoelectron Spectroscopy (XPS) was carried out by means of SPECS® coupled with Mg Kα source (1253.2 eV). The spectra were recorded between 200 and 1260 eV kinetic energies with a resolution of 2.5 eV. Data was analyzed via CasaXPS™ software using a Shirley background for the peak-deconvolution with a relative standard deviation less than 5%.

The electrochemical characterization was performed in a typical two-compartment three-electrode glass cell set-up. A dynamic hydrogen electrode (Hydroflex®, Gaskatel) was used as a reference electrode and a Pt coil encapsulated in a glass tube with a ceramic frit was used as a counter electrode. A rotating disk electrode (RDE, Pine Instruments) with a 0.196 cm^2 mirror polished glassy carbon insert was used as a working electrode. The Pt electrode loading was kept at 20 $\mu g_{Pt}\,cm^{-2}$ for Pt/G-ANF and Pt/C (20 wt.% Pt, BASF). The specific electrochemical surface area (ECSA) was calculated by dividing the electrochemical surface area (ESA) to the Pt mass. Specific and mass activities were obtained by dividing the kinetic current at 0.9 V_{RHE} to the electrochemical surface area and Pt mass, respectively [27,28]. All measurements were carried out in 200 ml freshly prepared 0.1 M $HClO_4$ solution.

3. Results and discussion

3.1. Graphenated alumina nanofibers

Fig. 1 shows images of both untreated ANF block serving as a support for carbon nanostructures growth and G-ANFs. The G-ANFs represent self-assembled, freestanding ANFs wrapped up with a few-layered graphene closed shells. One can see for the SEM images the highly porous structure of the ANFs remained after the graphene syntheses.

Fig. 2 presents HR-TEM images from the sample prepared by free catalyst CVD process on the surface of the ANFs using methane as a carbon source. Several graphitic layers with interspace of ca. 3–4 Å wrap the nanofibers being aligned with a longitudinal axis of the fiber. Mass gain of 14% corresponds to 1–3 layers of relatively “smooth” graphene shells around the dielectric nanofiber. Quite insignificant amount of nanofoliates grown from the surface of the outer graphene layers and not adherent to the ANF surface directly are observed. As one can see for the images the ANFs are completely covered by a few layers of graphene replicating the nanostructure of ANFs. Therefore, this relatively rough graphene can be successfully utilized for the catalyst immobilization. The nanostructures of the ANFs and the surface of the ANFs after graphene synthesis and Pt particle deposition are schematically shown in Fig. 3.

The Raman spectrum shown in Fig. 4 was found to exhibit strong G band peak at around 1596 cm^{-1} indicating the formation of a graphitized structure. The D peak at 1340 cm^{-1} provides further confirmation for the graphitic carbon formation. Graphene and few-layer graphene is characterized by an intense and narrow G band, a weak D mode and a very intense 2D mode. In our case, the intensity of the G peak is a bit lower as compared to 2D peak at ca. 2700 cm^{-1}. However, the narrow bands suggest that carbon possess a nanocrystalline structure. The position of 2D band at

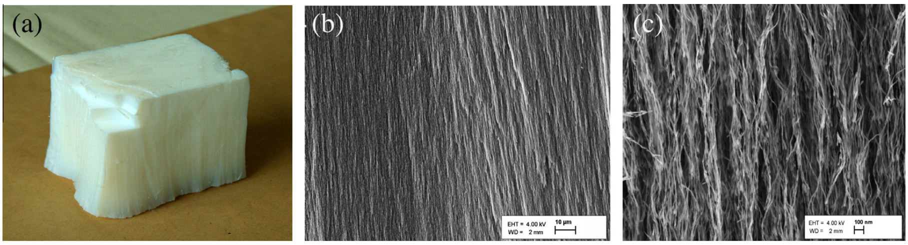

Fig. 1 – (a) Optical image of the block of the substrate alumina nanofibers (ANFs). The height of the block is about 5 cm. SEM images of (b) pristine ANFs and (c) G-ANFs obtained after 20 min CVD treatment. (A color version of this figure can be viewed online.)

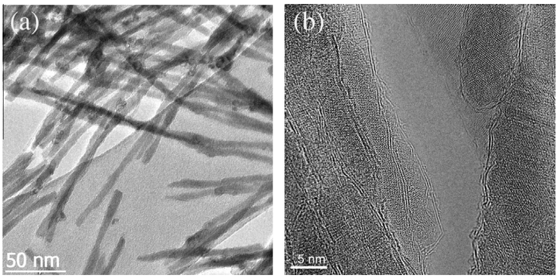

Fig. 2 – TEM image of the graphenated ANFs (G-ANFs).

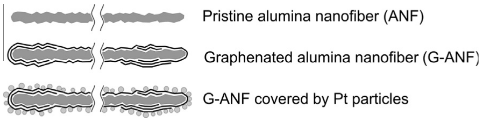

Fig. 3 – The schematics of a pristine ANF, after the graphene synthesis and after Pt particle deposition.

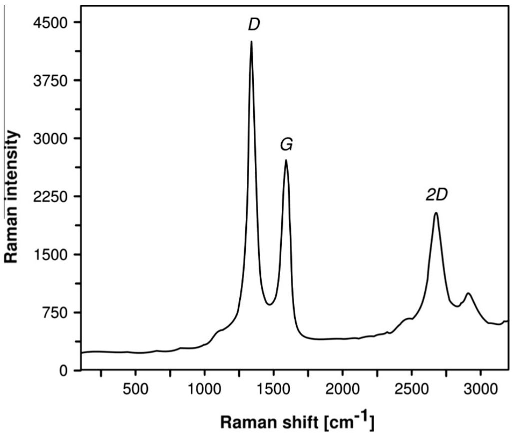

Fig. 4 – Raman spectrum of the G-ANFs obtained with the laser wavelength of 514 nm.

~2700 cm^{-1} pointed to the presence of a few-layers of graphene [21–26]. The Raman modes detected in this study reflect the main features observed for multiwalled carbon nanotubes (MWCNT) [21–24]. Actually, carbon nanotubes are essentially rolled up graphene sheets and multi-walled tubes represent several layers of graphene wrapped around the core tube. One of the features of MWCNT spectrum is a prominent D band [26]. This band is often referred as disorder- and/or defect- and/or edge-induced peak and its intensity relative to the intensity of G peak is used as a measure of the quality of carbon nanostructures. The strong and sharp D band peak and 2D band peak suggest nano-crystallinity of the structure and the formation of the edge-type defects along the length of the ANFs.

The ratio between the intensities of the D and G peaks, I_D/I_G, can be used for estimation of the amount of structural defects/edges and the degree of graphitization in graphitic materials [26]. The value of area-averaged I_D/I_G is about 1.5. Because of large number of the edge planes in the direction parallel to incident polarization as well as the twisted graphitic planes of graphene flakes, the I_D/I_G ratio is expectedly high. Following the procedure described in detail in [29], the ratio between intensities of the I_G and I_{2D} was calculated to be around 1.1 suggesting the presence of a few-layer graphene sheets.

The chemical composition of the carbon-alumina hybrid was examined by XPS. Only aluminum, oxygen and carbon are the constituting elements as it can be seen from the full survey spectrum shown in Fig. 5. The XPS survey confirms carbon as the main element present in material with approximately 55% of the surface composition being dominated by carbon. Therefore, it can be concluded that most of the alumina is entirely covered by carbon. The high resolution spectrum of C 1s peak is shown in Fig. 5b. This peak carries a main contribution from sp^2 hybridized carbon around 284.6 eV while the peak around 285.5 eV is attributed to the carbon structural defects. Fig. 5b clearly indicates the main contribution of the sp^2 hybridized carbon, which accounts for approximately 75%. Carbon defects contribution is estimated to only 5%. Three peaks at 286.5, 287.5 and 289.5 eV specify carbon–oxygen bonds such as C–O, C=O and C=OOH, respectively. Some degree of the carbon surface oxidation is expected due to the exposure to air. The last peak is common for nanostructured carbon and it comes from the π–π^* interaction [13,30].

3.2. *Electrochemical characterization*

A high degree of graphitization has been confirmed to exist as a main constituent component by Raman, XPS and high resolution-transmission electron microscopy (HR-TEM). Therefore, the platinized G-ANFs were considered as the

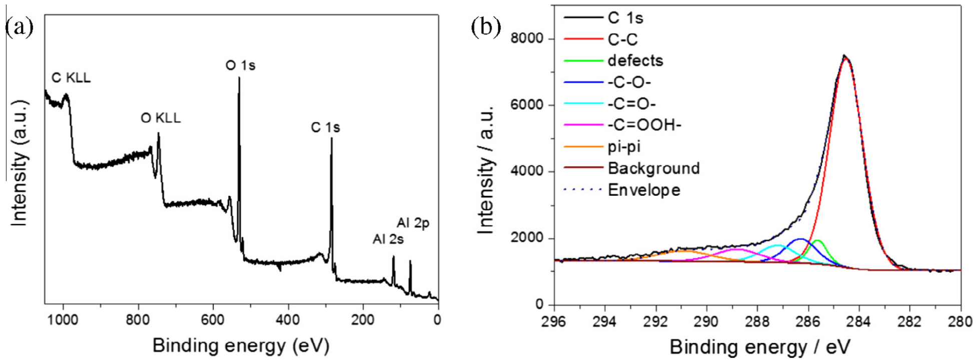

Fig. 5 – The results of (a) XPS investigations of G-ANFs; (b) deconvolution of the C 1s peak. (A color version of this figure can be viewed online.)

promising novel materials for an electrocatalyst support in fuel cells. Pt in the form of nanoparticles is uniformly dispersed on the surface of G-ANF (Fig. 6). Pt particles appear to fully cover the surface of G-ANF, yet no severe particle agglomeration can be observed (Fig. 6a and b). The morphology of Pt/G-ANF is presented in Fig. 6c where the sample appears to have a top layer formed of Pt nanoparticles, then a middle graphenated layer and an ANF core. This few-layered structure co-harvests the robustness properties of ANF and electrical conductivity of the graphenated layer. Pt crystallite size estimated from the Pt (111) reflection using the Scherrer equation is 2.9 ± 0.5 nm. This is close to the average particle size, 3.2 ± 0.3 nm, as obtained after counting approx. 500 particles from several HR-TEM images shown in Fig. 6d. The slight difference comes from the relative small number of particles counted from the HR-TEM images and the volume averaged size from XRD. Fig. 6 shows that the Pt nanoparticles supported on the outer graphene-like shell are homogeneously distributed with rather narrow variations in size. It is well-known that highly dispersed catalyst nanoparticles with ultra-fine size and narrow size distribution supported on carbon may serve as ideal system for high electrocatalytic activity.

The electrochemical performance depends on the degree of Pt availability to the reactants. The ESA was measured from the H_{upd} region (0.05–0.4 V_{RHE}), which is significantly larger for Pt/G-ANF than for Pt/C (20 wt.% Pt/C, BASF) as shown in the Supporting information, Fig. S1A. The oxygen reduction reaction sweeps at different rotating speed (Supporting information, Fig. S1B) resemble typical Pt/C oxygen reduction reaction sweeps. The diffusion limiting current values (measured at 0.4 V_{RHE}) are in accordance with the theory, which is $-6.1\ A\ cm^{-2}_{geo}$ at 1600 rpm (Supporting information, Fig. S1C). The difference in the potential at half current between Pt/G-ANF and Pt/C is approx. 22 mV. This means that there is a need of a smaller driving force to reduce the oxygen for Pt/G-ANF than for Pt/C, therefore it is expected that the mass and specific activities are larger for Pt/G-ANF.

Fig. 7 shows that Pt supported on G-ANF has an increased mass and specific activity as compared to the commercially available Pt/C. It is worth noting that the obtained values for Pt/C are in agreement with the previously reported values for this material [31]. An improvement of 50% from approx. 200 A g_{Pt}^{-1} for Pt/C to approx. 300 A g_{Pt}^{-1} for Pt/G-ANF has been obtained. The specific electrochemical surface area (ECSA) is an indirect measure of Pt availability; in the case of Pt/G-ANF the ECSA was estimated to be 85 $m^2\ g_{Pt}^{-1}$ and approximately 63 $m^2\ g_{Pt}^{-1}$ for Pt/C. Assuming that the average Pt nanoparticle size for Pt/C is 2.5 nm and 3.2 for Pt/G-ANF and the particles are spherical with a Pt density of

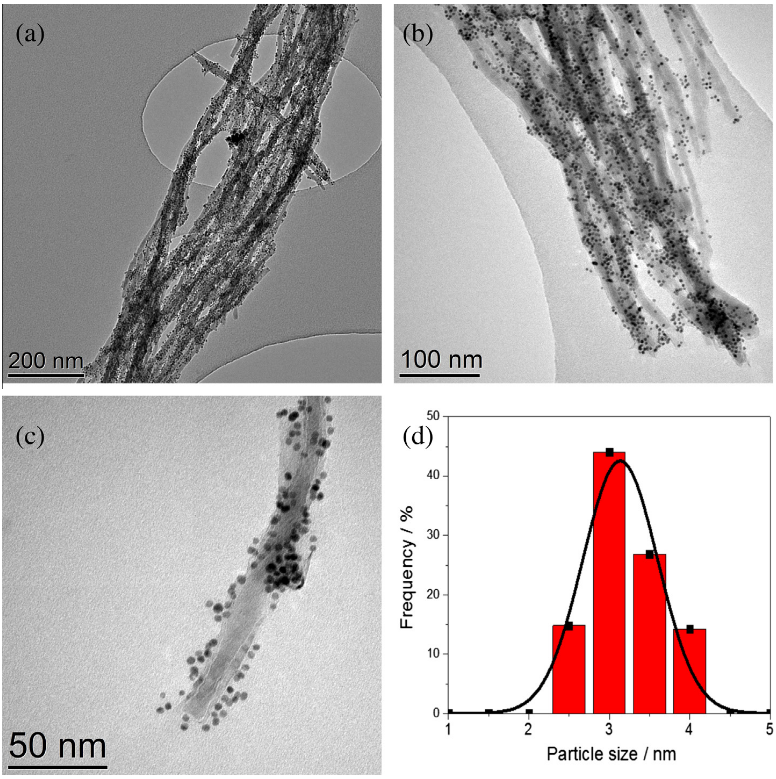

Fig. 6 – (a–c) Results of TEM observations of Pt nanoparticles on the surface of G-ANFs: HR-TEM images of Pt nanoparticles deposited on G-ANFs. (d) Histogram of Pt particle size. (A color version of this figure can be viewed online.)

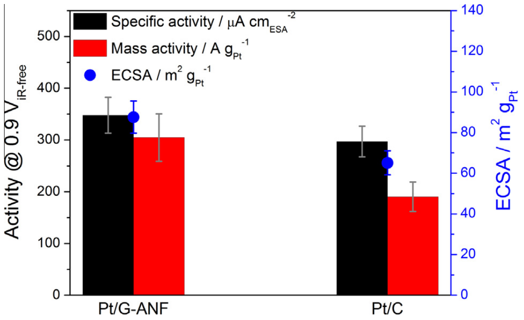

Fig. 7 – Specific activity (black bar) and mass activity (red bar) resulted from the kinetic current obtained at 1600 rpm in O_2 saturated 0.1 M $HClO_4$ and ECSA (blue scatter). (A color version of this figure can be viewed online.)

21.45 g cm^{-3}, a platinum usage of approx. 56% for Pt/C and 97% for Pt/G-ANF can be calculated. This reflects a better Pt availability for Pt/G-ANF, which is one of the main prerequisites for fuel cell electrocatalysts.

One of the important factors in electrochemical energy conversion is the stability under long-term potential cycling. An electrochemical protocol, which is widely acknowledged to promote the degradation of the electrocatalyst support [32] was used to study the durability and stability of the graphenated hybrid structure. The protocol consists of cycling the sample at 0.5 V s^{-1} between 1 and 1.5 V$_{RHE}$ for 30,000 cycles. This protocol is well-known for promoting support degradation [32,33]. It was demonstrated in Fig. 8 that less than 3% of the initial ESA was lost after testing. One should bear in mind that in a similar test the ESA loss is in the range of 20–30% for Pt/C [33,34]. To the best of our knowledge, this remarkable electrochemical stability is unprecedented in the literature. Moreover, the cyclic voltammogram (CV) at the beginning of the test (BOT) and at the end of the test (EOT) are remarkably similar (inset of Fig. 8). On the forward going sweep, between 0.05 and 0.4 V$_{RHE}$, almost no difference can be seen between the CVs at BOT and EOT. This region was used to measure the electrochemically available surface, confirming the availability of platinum even after 30,000 cycles. Therefore, the G-ANFs are not undergoing severe corrosion or decomposition. Furthermore, the peak at around 0.75 V$_{RHE}$ on the cathodic side does not shift towards higher potentials, which might indicate possible platinum particle growth. In the double-layer region (0.4–0.8 V$_{RHE}$), no striking difference can be observed indicating that the graphenic-carbon surface did not suffer from severe carbon oxidation.

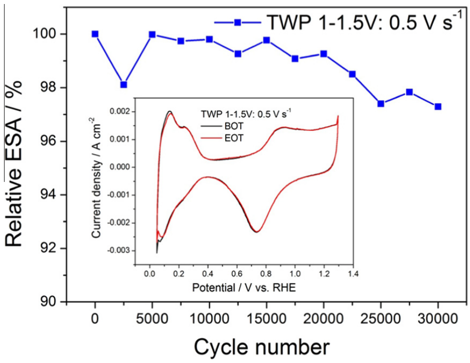

Fig. 8 – Relative ESA as function of cycle number during a triangle wave potential (TWP) cycling between 1 and 1.5 V$_{RHE}$ at 0.5 V s^{-1} for 30,000 cycles in Ar saturated 0.1 M $HClO_4$. The inset shows the cyclic voltammograms at beginning of test (BOT, black line) and end of test (EOT, red line). (A color version of this figure can be viewed online.)

This remarkable improvement in electrochemical stability might be explained by the formation of a Pt–graphene interface. Recently, it has been shown that the competition between Pt–Pt and Pt–C bonds was held responsible for the creation of a self-assembled Pt nanoparticle geometry [12]. Even though the Pt–Pt bonds are preferred in the detriment of Pt–C bonds, it is very likely that the relative small number of the Pt–C bonds is sufficient for maintaining efficient electrocatalyst morphology. At the same time, it should be noted that the electrochemical aging protocol used is focused on the degradation of the electrocatalyst support (i.e. G-ANF). According to the XPS and HR-TEM, G-ANF has a high relative concentration of sp^2 hybridized carbon. This is not the case for active carbon (i.e. the support in Pt/C) in which sp^3 is the preferred hybridization. Carbon electrochemical degradation is more prone at sp^3 sites rather than sp^2 sites [35,36], therefore it should be expected for G-ANF to be more stable owed to its high degree of sp^2 hybridization.

To sum up, we have designed a material which offers all the properties needed for serving as a highly stable electrocatalyst support. The novel technique can be generalized and applied successfully to other materials that can further improve the activity and stability of the electrocatalyst support. For example, mixed protonic-electronic conductors, where a non-durable protonic conductor (i.e. WO_3) can be covered by a highly stable graphene, can result in a perfect tandem. Therefore, we consider that the novel technique opens a new way of viewing ceramic–graphene hybrids by offering an intuitive bottom-up approach. This bottom-up approach of platinizing a graphene closed shell ceramic opens the road to co-harvesting the electronic properties of graphene and the robustness of ceramic materials. This finding has a straightforward application in future catalyst nanoarchitectures. Further improvement in the control of the process parameters can lead to the direct deposition of the tailored graphenic structures for a large-scale use in different applications. Post-mortem electrochemical stability studies are currently undergoing.

4. Conclusions

We have synthesized a novel nanomaterial, graphenated alumina nanofibers (G-ANFs), consisting of the metal oxide nanofibers surrounded by the conductive and inert few-layered graphene by a free catalyst direct one-step CVD process using methane as a carbon source. This material was found to be a promising material for electrochemical applications. After the platinization of the G-ANFs, the hybrid material was tested as a fuel cell electrocatalyst. A 1.5-fold improvement in the mass activity has been obtained for Pt/G-ANF in comparison to the commercially available Pt/C. The outstanding electrochemical stability of the obtained material was attributed to high specific surface area and nano rough structure of the graphenated wraps around the metal oxide nanofibers immobilized the catalyst on the surface of graphene.

Acknowledgments

This work was supported by institutional research funding IUT 19-29 of the Estonian Ministry of Education and Research and Danish project PEM Durability and Lifetime Part III (Energinet.dk Project No. 2013-1-12064). Archimedes targeted grant AR12133 (NanoCom) is also gratefully appreciated for supporting this study. The authors thank Ministry of Education and Science of Russian Federation (Project DOI: RFMEFI58114X0006) for financial support. This work made use of the Aalto University Nanomicroscopy Center (Aalto-NMC) premises.

Appendix A. Supplementary data

Supplementary data associated with this article can be found, in the online version, at http://dx.doi.org/10.1016/j.carbon.2015.03.004.

REFERENCES

[1] Candelaria SL, Shao Y, Zhou W, Li X, Xiao J, Zhang J-G, et al. Nanostructured carbon for energy storage and conversion. Nano Energy 2012;1:195–220. http://dx.doi.org/10.1016/j.nanoen.2011.11.006.

[2] Hecht DS, Hu L, Irvin G. Emerging transparent electrodes based on thin films of carbon nanotubes, graphene, and metallic nanostructures. Adv Mater 2011;23:1482–513. http://dx.doi.org/10.1002/adma.201003188.

[3] Inagaki M, Konno H, Tanaike O. Carbon materials for electrochemical capacitors. J Power Sources 2010;195:7880–903. http://dx.doi.org/10.1016/j.jpowsour.2010.06.036.

[4] Zhang LL, Zhou R, Zhao XS. Graphene-based materials as supercapacitor electrodes. J Mater Chem 2010;20:5983. http://dx.doi.org/10.1039/c000417k.

[5] Jhan J-Y, Huang Y-W, Hsu C-H, Teng H, Kuo D, Kuo P-L. Three-dimensional network of graphene grown with carbon nanotubes as carbon support for fuel cells. Energy 2013;53:282–7. http://dx.doi.org/10.1016/j.energy.2013.03.002.

[6] Novoselov KS, Jiang Z, Zhang Y, Morozov SV, Stormer HL, Zeitler U, et al. Room-temperature quantum Hall effect in graphene. Science 2007;315:1379. http://dx.doi.org/10.1126/science.1137201.

[7] Schedin F, Geim AK, Morozov SV, Hill EW, Blake P, Katsnelson MI, et al. Detection of individual gas molecules adsorbed on graphene. Nat Mater 2007;6:652–5. http://dx.doi.org/10.1038/nmat1967.

[8] Stoner BR, Glass JT. Carbon nanostructures: a morphological classification for charge density optimization. Diam Relat Mater 2012;23:130–4.

[9] Parker CB, Raut AS, Brown B, Stoner BR, Glass JT. Three-dimensional arrays of graphenated carbon nanotubes. J Mater Res 2012;27:1046–53. http://dx.doi.org/10.1557/jmr.2012.43.

[10] Yoo E, Okata T, Akita T, Kohyama M, Nakamura J, Honma I. Enhanced electrocatalytic activity of Pt subnanoclusters on graphene nanosheet surface. Nano Lett 2009;9:2255–9.

[11] Datsyuk V, Guerret-Piécourt C, Dagréou S, Billon L, Dupin J-C, Flahaut E, et al. Double walled carbon nanotube/polymer composites via in-situ nitroxide mediated polymerisation of amphiphilic block copolymers. Carbon NY 2005;43:873–6. http://dx.doi.org/10.1016/j.carbon.2004.10.052.

[12] Xu P, Dong L, Neek-Amal M, Ackerman ML, Yu J, Barber SD, et al. Self-organized platinum nanoparticles on freestanding graphene. ACS Nano 2014;8:2697–703.

[13] Stamatin SN, Borghei M, Dhiman R, Andersen SM, Ruiz V, Kauppinen E, et al. Activity and stability studies of platinized multi-walled carbon nanotubes as fuel cell electrocatalysts. Appl Catal B Environ 2015;162:289–99.

[14] Kou R, Shao Y, Mei D, Nie Z, Wang D, Wang C, et al. Stabilization of electrocatalytic metal nanoparticles at metal–metal oxide–graphene triple junction points. J Am Chem Soc 2011;133:2541–7.

[15] Sahoo NG, Pan Y, Li L, Chan SH. Graphene-based materials for energy conversion. Adv Mater 2012;24:4203–10.

[16] Hiramatsu M, Mitsuguchi S, Horibe T, Kondo H, Hori M, Kano H. Fabrication of carbon nanowalls on carbon fiber paper for fuel cell application. Jpn J Appl Phys 2013;52.

[17] Ismach A, Druzgalski C, Penwell S, Schwartzberg A, Zheng M, Javey A, et al. Direct chemical vapor deposition of graphene on dielectric surfaces. Nano Lett 2010;10:1542–8. http://dx.doi.org/10.1021/nl9037714.

[18] Rümmeli MH, Bachmatiuk A, Scott A, Börrnert F, Warner JH, Hoffman V, et al. Direct low-temperature nanographene CVD synthesis over a dielectric insulator. ACS Nano 2010;4:4206–10. http://dx.doi.org/10.1021/nn100971s.

[19] Aghayan M, Hussainova I, Gasik M, Kutuzov M, Friman M. Coupled thermal analysis of novel alumina nanofibers with ultrahigh aspect ratio. Thermochim Acta 2013;574:140–4. http://dx.doi.org/10.1016/j.tca.2013.10.010.

[20] Yan X, Yong K. Size control of polymer-stabilized ruthenium nanoparticles by polyol reduction. J Mater Chem 2001;11:3387–91.

[21] Ferrari AAC, Basko DMD. Raman spectroscopy as a versatile tool for studying the properties of graphene. Nat Nanotechnol 2013;8:235–46. http://dx.doi.org/10.1038/nnano.2013.46.

[22] Pimenta MA, Dresselhaus G, Dresselhaus MS, Cançado LG, Jorio A, Saito R. Studying disorder in graphite-based systems by Raman spectroscopy. Phys Chem Chem Phys 2007;9:1276–91. http://dx.doi.org/10.1039/b613962k.

[23] Ferrari AC, Meyer JC, Scardaci V, Casiraghi C, Lazzeri M, Mauri F, et al. Raman spectrum of graphene and graphene layers. Phys Rev Lett 2006;97:187401. http://dx.doi.org/10.1103/PhysRevLett. 97.187401.

[24] Ferrari AC. Raman spectroscopy of graphene and graphite: disorder, electron–phonon coupling, doping and nonadiabatic effects. Solid State Commun 2007;143:47–57. http://dx.doi.org/10.1016/j.ssc.2007.03.052.

[25] Bokobza L, Bruneel J-L, Couzi M. Raman spectroscopic investigation of carbon-based materials and their composites. Comparison between carbon nanotubes and carbon black. Chem Phys Lett 2013;590:153–9. http://dx.doi.org/10.1016/j.cplett.2013.10.071.

[26] Casiraghi C, Hartschuh A, Qian H, Piscanec S, Georgi C, Fasoli A, et al. Raman spectroscopy of graphene edges. Nano Lett 2009;9:1433–41. http://dx.doi.org/10.1021/nl8032697.

[27] Vielstich W, Lamm A, Gaseiger HA. Handbook of fuel cells—fundamentals, technology and applications. 2nd ed., vol. 3. New York: Wiley; 2003. p. 190.

[28] Mayrhofer KJJ, Strmcnik D, Blizanac BB, Stamenkovic V, Arenz M, Markovic NM. Measurement of oxygen reduction activities via the rotating disc electrode method: from Pt model surfaces to carbon-supported high surface area catalysts. Electrochim Acta 2008;53:3181–8.

[29] Reina A, Jia X, Ho J, Nezich D, Son H, Bulovic V, et al. Large area, few-layer graphene films on arbitrary substrates by chemical vapor deposition. Nano Lett 2009;9:30–5. http://dx.doi.org/10.1021/nl801827v.

[30] Ago H, Kugler T, Cacialli F, Salaneck WR, Shaffer MSP, Windle AH, et al. Work functions and surface functional groups of multiwall carbon nanotubes. J Phys Chem B 1999;103:8116–21. http://dx.doi.org/10.1021/jp991659y.

[31] Gasteiger HA, Kocha SS, Sompalli B, Wagner FT. Activity benchmarks and requirements for Pt, Pt-alloy, and non-Pt oxygen reduction catalysts for PEMFCs. Appl Catal B Environ 2005;56:9–35.

[32] Ohma A, Shinohara K, Iiyama A, Yoshida T, Daimaru A. Membrane and catalyst performance targets for automotive fuel cells by FCCJ membrane, catalyst, MEA WG. ECS Trans 2011;41:775–84.

[33] Zana A, Speder J, Roefzaad M, Altmann L, Baumer M, Arenz M. Probing degradation by IL-TEM: the influence of stress test conditions on the degradation mechanism. J Electrochem Soc 2013;160:F608–15.

[34] Speder J, Zana A, Spanos I, Kirkensgaard JJK, Mortensen K, Arenz M. On the influence of the Pt to carbon ratio on the degradation of high surface area carbon supported PEM fuel cell electrocatalysts. Electrochem Commun 2013;34:153–6. http://dx.doi.org/10.1016/j.elecom.2013.06.001.

[35] Stamatin SN, Borghei M, Andersen SM, Veltze S, Ruiz V, et al. Influence of different carbon nanostructures on the electrocatalytic activity and stability of Pt supported electrocatalysts. Int J Hydrogen Energy 2014;39:8215–24.

[36] Yousfi-Steiner N, Mocoteguy P, Candusso D, Hissel D. A review on polymer electrolyte membrane fuel cell catalyst degradation and starvation issues: causes, consequences and diagnostic for mitigation. J Power Sources 2009;194:130.

PUBLICATION III

Stamatin, S. N., Hussainova, I., **Ivanov, R.**, Colavita, P. E., Quantifying graphitic edge exposure in graphene based materials and its role in oxygen reduction reactions. — *ACS Catalysis*, 2016, 6, 5215–5221, doi:10.1021/acscatal.6b00945

ACS Catalysis
Research Article
pubs.acs.org/acscatalysis

Quantifying Graphitic Edge Exposure in Graphene-Based Materials and Its Role in Oxygen Reduction Reactions

Serban N. Stamatin,[†,∥] Irina Hussainova,[‡,§] Roman Ivanov,[‡] and Paula E. Colavita*[,†]

[†]School of Chemistry and Centre for Research on Adaptive Nanostructures and Nanodevices (CRANN), Trinity College Dublin, College Green, Dublin 2, Ireland

[‡]Department of Materials Engineering, Tallinn University of Technology, Ehitajate 5, 19086 Tallinn, Estonia

[§]ITMO University, Kronverkskiy 49, St. Petersburg 197101, Russia

Supporting Information

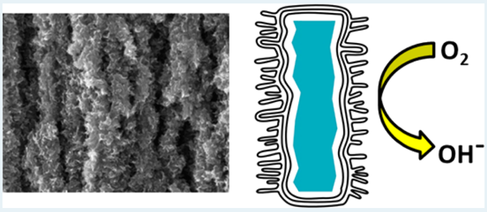

ABSTRACT: Oxygen electrochemistry is at the core of several emerging energy conversion technologies. The role of carbon nanostructures in the electrocatalysis of the oxygen reduction reaction is not well understood. Herein we report an investigation of the role of graphitic edges in oxygen electrochemistry. A new synthetic method was used to create all-carbon model electrode materials with controlled morphology. Electron microscopy results show that synthesized materials possess a high density of graphitic edges. Electrochemical intercalation experiments, however, indicate that the density of electroactive edges does not correlate positively with microscopy results. The materials were then characterized as electrodes for the oxygen reduction reaction in alkaline media. Results suggest that electrochemical determinations of edge and defect density more accurately predict electrocatalytic activity, thus suggesting that in situ characterization techniques are needed to understand the carbon/electrolyte interface.

KEYWORDS: *graphene, electrocatalysis, graphitic edges, oxygen reduction, ORR, intercalation, defects*

INTRODUCTION

Oxygen electrochemistry plays a crucial role in the deployment of several emergent energy technologies, such as the air cathodes in metal−air batteries and fuel cells. Polymer electrolyte membrane fuel cells (PEMFCs) are probably the most suitable candidates for powering the future automotive industry. However, high cost and short lifetime are the two key drawbacks that must be overcome for PEMFCs to be widely adopted by industry. The cathode materials cost contributes significantly to the overall cost of the membrane electrode assembly: the sluggish oxygen reduction reaction (ORR) gives rise to high cathodic overpotentials that require the use of precious-metal catalysts, with Pt being the preferred choice.[1]

Nanocarbons are usually used as Pt supports for fuel cell applications due to their high surface area and corrosion resistance.[2] It has been reported that the use of heteroatom-doped carbon as a support results in increased stability and activity due to catalyst−support interactions.[3−5] Heteroatom-doped carbon can also show intrinsic ORR activity which is not yet fully understood[6,7] but which is proposed to arise from the effect of heteroatom modifications on electronic, chemical, and/or morphological properties of the carbon material. Modification of carbons via functionalization or doping with heteroatoms can result in changes in the density of states and Fermi energy positioning.[1,8,9] Heteroatom modification can also create specific chemical sites at the carbon surface, thus offering new adsorption or chemisorption channels to redox species in solution. The carbon morphology may also be altered; for instance, the introduction of pyridinic groups can favor the presence of graphitic edges and thus influence the density of defects in the material.[10] Electronic, chemical, and structural/morphological effects are therefore interrelated in heteroatom-modified carbons, and they can all affect mechanisms and rates of electrochemical reactions.[11] Therefore, it is often challenging to ascribe an observed change in ORR activity to a specific effect to develop new insights into optimal carbon material design.

Graphitic edge (GE) exposure is one of the carbon properties that is of great interest in electrochemistry.[12−15] Testing the electrochemical behavior of GEs is difficult because of the challenges involved in achieving well-defined morphologies that are rich in edges and because of the challenges involved in characterizing GEs. Studies on ball-milled graphene concluded that small graphene flakes possess a higher ORR activity than larger particles due to greater exposure of GEs.[16−18] However, ball milling yields defect-rich materials that also possess oxidized surface functionalities; both of these give rise to changes in density of electronic states and lead to the presence of specific chemical sites, which can both influence

Received: April 4, 2016
Revised: June 28, 2016

DOI: 10.1021/acscatal.6b00945
ACS Catal. 2016, 6, 5215−5221

ORR activity.[19] Therefore, there is a need to test materials in which the sole effect of GE can be related to ORR activities.

GEs are usually characterized by electron microscopy methods, Raman spectroscopy, and X-ray photoelectron spectroscopy. Imaging techniques are a local probing tool, while Raman and X-ray photoelectron spectroscopy offer insights into the structure and functionalities present at the carbon surface. Indeed, the electrode kinetics are influenced by oxygen functionalities;[19] hence, the methods are mandatory for understanding the carbon. However, these characterization methods do not offer any information about the carbon/electrolyte interface, which is the main focus of electrochemistry.

Herein, we report a novel method for the production of carbon nanostructures with controlled morphologies grown on a dielectric alumina nanofiber support. We used the materials thus grown to investigate the role of GEs in oxygen reduction reactions at undoped carbon materials, with the chief aim of understanding the effect of changes in carbon matrix structure on ORR activity. Our results highlight the importance of establishing the density of electroactive GEs to correctly interpret ORR activity trends.

EXPERIMENTAL METHODS

Materials Synthesis. The graphene layers were deposited onto a support of alumina (γ-Al_2O_3) nanofibers of 7 ± 2 nm in diameter and specific surface area of 155 m^2 g^{-1},[20] by a one-step catalyst-free chemical vapor deposition (CVD) technique, as detailed elsewhere.[21,22] Decomposition of methane in the presence of nitrogen as carrier gas is catalyzed by unsaturated Al sites on an oxide surface and results in deposition of a carbon film at 1000 °C and atmospheric pressure. The carbon obtained via CVD wraps the alumina nanofibers, forming a multilayered graphene-like shroud along the oxide fiber. Deposition time, ratio between carbon source and carrier gas, and the total flow rate were controlling factors for the carbon loading and the morphology of carbon−alumina hybrid structures. In this work the dwell times were selected to be 20, 60, and 120 min in order to fabricate carbon materials with different morphologies used for electrochemical studies.

Characterization. The morphology of the hybrid structures was examined by high-resolution scanning electron microscopy (HR-SEM, Zeiss Gemini Ultra-55) and transmission electron microscopy (TEM JEOL JEM-2200FS). Raman spectra of the graphene layers on alumina substrates were obtained on a Horiba LabRam R800 with 532 nm laser excitation.[23] The carbon content was determined by thermogravimetric analysis (Stanton Redcroft); samples were heated in air up to 950 °C at 5 °C min^{-1}. Specific surface area measurements were carried out on a Quantachrome Autosorb iQ instrument, running nitrogen physisorption measurements at 77 K. X-ray photoelectron spectroscopy (XPS) was performed in an Omicron Multiprobe XPS system with a base pressure of 2×10^{-10} mbar, using a monochromated Al Kα source ($h\nu$ = 1486.6 eV) and an EA125 U5 analyzer at a 45° takeoff angle. Wide surveys were collected at 50 eV pass energy, while core level spectra were collected at 20 eV pass energy. Data were analyzed using CasaXPS; high-resolution spectra were Shirley background corrected and fitted with Voigt line shapes in order to obtain area ratios.

Hydrodynamic electrochemical characterization was performed in a three-electrode glass cell setup. All of the water used throughout the experiments was ultrapure water (>18.2 MΩ, Millipore). The electrochemical cell was kept at 80 °C overnight in ultrapure water prior to use. A hydrogen electrode (Hydroflex, Gaskatel) was used as reference electrode, and a high-purity graphite rod (99.997%, Goodfellow) was used as a counter electrode. The reference electrode potential was calibrated by performing hydrogen evolution reactions as reported in previous studies.[24] Its potential was found to be +10 mV vs RHE (Figure S1 in the Supporting Information). A rotating-disk electrode (RDE, Pine Instruments) with a 0.196 cm^2 glassy-carbon insert was used as a working electrode. The electrodes were polished to a mirror finish prior to use with a 50 nm alumina slurry on a polishing cloth (Buehler). The inks were formulated by dispersing 4.0 mg of the desired material in 920 μL of ultrapure water/isopropyl alcohol (1/1 v/v) and 80 μL of 0.05 wt % Nafion solution. The solution was sonicated for 1 h; subsequently, a 10 μL drop was spread on the surface of the mirror-polished glassy carbon. All measurements were carried out in 150 mL of freshly prepared 0.1 M KOH (semiconductor grade pellets, Sigma-Aldrich). First, the electrode was conditioned by running 10 cyclic voltammograms (CVs) between 0.05 and 1.2 V_{RHE} at a 0.2 V s^{-1} scan rate (Metrohm potentiostat). The electrolyte was then deaerated with Ar for 30 min and an additional 5 CVs were recorded from 0.05 to 1.1 V_{RHE} and a 0.05 V s^{-1} scan rate. Oxygen reduction reactions (ORRs) were recorded at 0, 400, 900, and 1600 rpm in O_2-saturated 0.1 M KOH. In order to correct for the capacitive current, the CVs in Ar were subtracted from the ORR sweeps. The onset potential was defined as the potential where the current is 0.1 mA cm^{-2}.[25] Kinetic currents were determined from the Koutecky−Levich formula.[26] Error bars for numerical values represent 95% confidence intervals.

Intercalation studies using 4-nitrobenzylamine (4-NBA), obtained according to previously reported methods,[27] were carried out by suspending 1.0 mg of the desired material in 5 mL of a 10 mM solution of 4-NBA in acetonitrile.[28] After 3 h of incubation time, the powders were collected by centrifugation and washed three times with acetonitrile and water to remove excess 4-NBA. A 1.0 mg amount of 4-NBA intercalated powders was collected and redispersed in 1 mL of acetonitrile and subsequently used as an ink. A 10 μL portion of this ink was spread on the surface of glassy carbon and immersed in 100 mL freshly prepared deaerated 0.1 M H_2SO_4 (>95% Trace-Select Ultra, SigmaAldrich). Voltammetric scans for the determination of 4-NBA coverage were carried out in an all-Teflon home-built electrochemical cell and a three-electrode geometry, using a saturated KCl Ag/AgCl (0.198 V vs RHE) reference electrode (IJ Cambria) and a Pt wire as a counter electrode. All potentials were referenced against the RHE for the reported data. CVs were recorded from −0.8 to 1.2 V_{RHE} starting at 1.2 V_{RHE} at a scan rate of 0.2 V s^{-1} (Metrohm potentiostat). The second scan was used as a background scan for the integration of the charge associated with the cathodic peak between −0.3 and 0.2 V_{RHE}. Error bars for numerical values represent 95% confidence intervals.

RESULTS AND DISCUSSION

Structural and Chemical Characterization of Graphene-Coated Nanofibers. Carbon electrodes used for our studies were obtained via CVD growth on alumina nanofiber supports;[21,22,29] the process yielded graphene-coated alumina nanofibers (G-ANF) whereby the morphology of the carbon phase could be controlled by varying the dwell time in the CVD chamber. Figure 1 shows HR-SEM images of the samples after

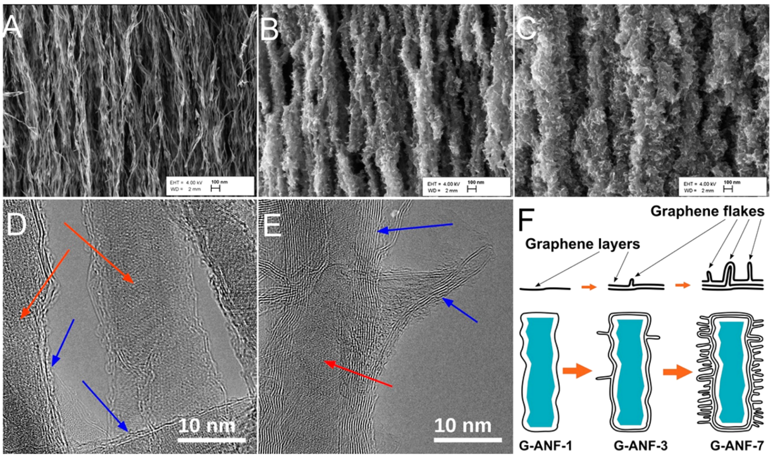

Figure 1. SEM images of G-ANF-1 (A), G-ANF-3 (B), and G-ANF-7 (C) (scale bar 100 nm). TEM images of G-ANF-1 (D) and G-ANF-3 (E). Schematic illustration of the material synthesis (F).

20 (A), 60 (B), and 120 min (C) of processing. These samples are from here onward denoted as G-ANF-1, G-ANF-3, and G-ANF-7, respectively, according to their carbon content, which is discussed below. Images in Figure 1A−C show that as the dwell time increases the width of G-ANFs increases while their walls become decorated with graphene-like flakes or protrusions. HR-TEM images of G-ANF-1 and G-ANF-3 are shown in Figure 1D,E. Analysis of G-ANF-1 reveals the presence of three to five graphene layers oriented parallel to the long axis of the fibers with an interspacing of 3−4 Å. Therefore, the structure of G-ANF-1 fibers is similar to that of a multiwall carbon nanotube. As the growth process progresses, the thickness of the carbon wall increases, as is evident in Figure 1E, where a larger number of graphene layers parallel to the long axis can be clearly seen. The development of flakes or foliates that protrude from the fiber walls is also clearly observed in Figure 1E; these foliates are thinner than the fiber walls and consist of only two to three graphene layers. The microscopy analysis therefore shows that in the early stages of CVD growth the alumina fibers are coated by a few graphene layers parallel to the oxide surface; longer deposition times lead to an increase in the number of these layers but also to the development of protrusions consisting of a few graphene layers, as shown in the schematic in Figure 1F. Microscopy results are consistent with TGA analysis (Figure S2 in the Supporting Information), which reveals that the carbon content in G-ANFs increases in the order G-ANF-1 < G-ANF-3 < G-ANF-7 and their mass gains are 15%, 300%, and 700%, respectively. Interestingly, the G-ANF morphology suggests that these materials might possess a high density of exposed graphitic edges (GEs). In particular, G-ANF-3 and G-ANF-7 samples present a high density of flakes, thus suggesting they could be good electrode materials with a high density of sites for adsorption and fast charge transfer.

XPS analysis shows that the surface of G-ANF samples is mainly composed of carbon and oxygen, as indicated by the presence of C 1s and O 1s peaks in survey spectra (Figure 2A). G-ANF-1 exhibits two additional peaks at binding energies of 74 and 119 eV, which are absent in G-ANF-3 and G-ANF-7 and which can be assigned to Al 2p and 2s photoelectrons (Figure 2A). The presence of Al in G-ANF-1 samples can be attributed to the alumina (γ-Al_2O_3) support, thus indicating that G-ANF-1 has lower carbon coverage than G-ANF-3 and G-ANF-7, in agreement with TGA determinations of carbon loading. As the dwell time in the CVD chamber increases, the carbon grows uniformly, leading to the complete coating of the alumina support with thicker carbon layers and to the disappearance of Al peaks.

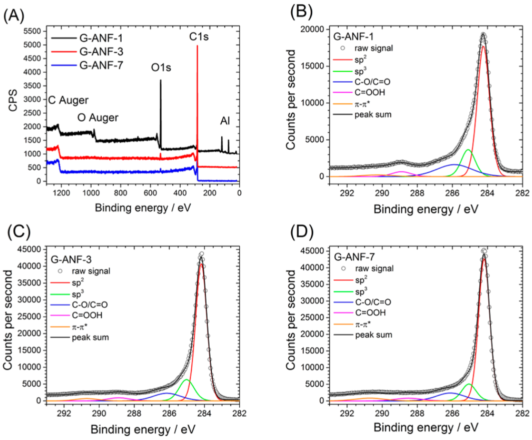

Figure 2. X-ray photoelectron spectra survey (A) and high-resolution spectra of G-ANF-1 (B), G-ANF-3 (C), and G-ANF-7 (D).

Table 1 summarizes atomic ratios determined on the basis of peak area ratios from XPS high-resolution scans. The oxygen

Table 1. Summary of Surface Concentration (Atom Percent) Determined from XPS Analysis

				C 1s		
	C	O	Al	sp^2	sp^3	ox C
G-ANF-1	52	28	20	63	15	20
G-ANF-3	97	3	0	70	14	13
G-ANF-7	99	1	0	69	14	12

content is highest for G-ANF-1 samples, in agreement with the observation of peaks arising from the alumina support; a comparison of the O 1s peaks of G-ANF samples confirmed that the majority of the photoemitted intensity in G-ANF-1 is due to oxygen atoms from the alumina support (Figure S3 in the Supporting Information). The oxygen content is lowest for G-ANF-7, thus indicating that the growth process leads to the deposition of a film with high carbon purity. The C 1s spectra exhibit a sharp peak at 284.3 eV with additional contributions at higher binding energies, as shown in Figure 2B−D. A best fit of the C 1s envelope was obtained using five contributions at 284.3, 285.1, 286.1, 288.9, and 291.2 eV that can be attributed to trigonally bonded carbon (sp^2 centers), tetrahedrally bonded carbon (sp^3 centers), C−O/C=O carbon, carboxylic acid groups, and $\pi-\pi^*$ shake-up peaks, respectively.[29] A summary of the percent composition for sp^2, sp^3, and oxidized carbon centers is reported in Table 1. The sp^3 contribution remains constant at ∼15% for all samples; however, the sp^2 concentration increases from 63% for G-ANF-1 to 70 and 69% for G-ANF-3 and G-ANF-7, respectively. The lower sp^2 concentration in G-ANF-1 occurs in parallel with a higher concentration of oxidized carbon centers (20%), thus suggesting that the slightly lower graphitic content at the early stages of the carbon growth might be due to chemical interactions between carbon and the oxide support.

Figure 3 shows Raman spectra of G-ANF-1, G-ANF-3, and G-ANF-7. The main features in Raman spectra of carbons are the D and G peaks, at ∼1350 and ∼1590 cm^{-1}, respectively,[30] which are characteristic of carbon materials. Additional peaks at 2680, 2930, and 3230 cm^{-1} can be assigned to 2D, D + D′, and 2D′ bands, respectively, which are characteristic of graphene layers.[23]

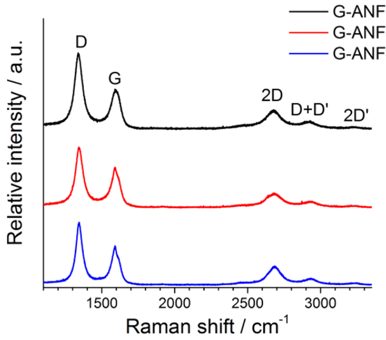

Figure 3. Raman spectra (excitation 532 nm) of G-ANF-1 (black), G-ANF-3 (red), and G-ANF-7 (blue). All spectra are normalized by the height of the G peak to facilitate comparison.

The presence of a single symmetric peak at 2680 cm^{-1} indicates that G-ANFs mostly consist of few-layer graphene, as this peak splits into an asymmetric doublet in the case of graphite;[30] moreover, the relatively narrow bands suggest the layers and foliates possess a nanocrystalline structure.[23] The D peak is due to the breathing modes of carbon rings and requires defects for its activation;[23] the D band intensity may be used to quantify disorder in the structures.[31] The ratio between intensities of the D and G peaks, I_D/I_G, can be used for comparing the amount of structural defects/edges and the degree of graphitization. The value of I_D/I_G is highest at 1.9 for G-ANF-1 and decreases to 1.4 for both G-ANF-3 and G-ANF-7; this suggests that the first few layers deposited at shorter dwell times are more defective than those deposited at later stages in the CVD process. A similar trend is obtained if peak height ratios are used in this analysis. This is likely due to the close interaction between the first few layers and the support; as the thickness of the carbon wall grows, subsequent layers are deposited on an all-carbon surface and allow for larger crystallite size.

Finally, the BET surface areas determined from N_2 adsorption isotherms were found to decrease with increasing carbon content, from 203 $m^2\ g^{-1}$ for G-ANF-1 to 125 $m^2\ g^{-1}$ for G-ANF-3 and 119 $m^2\ g^{-1}$ for G-ANF-7. In summary, this synthetic strategy yields carbon nanofibers with carbon walls consisting of few layers of graphene and with graphene foliates that protrude and expose graphitic edges at the carbon interface.

Electrochemical Characterization of Graphene-Coated Nanofibers. G-ANF materials offer an opportunity to study the electrochemical performance of metal- and dopant-free highly graphitic materials that are rich in graphitic edges (GEs). In this context, we decided to test these materials as model catalysts for understanding the role of GEs in the electrochemical reduction of water at nanostructured carbon electrodes, a matter yet to be understood.[26,32−34] We also carried out measurements on glassy carbon (GC) for comparing the performance of G-ANFs to a standard graphitic carbon electrode material.

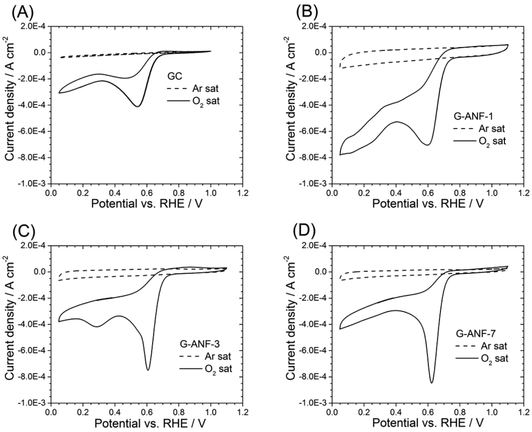

Figure 4. Cyclic voltammetric scans of GC (A), G-ANF-1 (B), G-ANF-3 (C), and G-ANF-7 (D) in 0.1 M KOH saturated with Ar (dashed line) and O_2 (solid line), recorded between 0.05 and 1.1 V_{RHE} at 0.05 V s^{-1} and 25 °C.

Cyclic voltammetric scans of glassy carbon (GC), G-ANF-1, G-ANF-3, and G-ANF-7 are featureless in Ar-saturated 0.1 M KOH (Figure 4). Among all the samples, G-ANF-1 has the highest capacitive current contributions, followed by G-ANF-3 and G-ANF-7. The observed trend in capacitive currents mirrors the measured BET areas, with G-ANF-1 being the material with the largest BET area and the greatest capacitive contribution in its CV. All samples exhibit a dramatic increase in current around 0.75 V_{RHE} in O_2-saturated electrolyte in comparison to the currents observed in Ar-saturated electrolyte (Figure 4B−D). This increase around 0.75 V_{RHE} in O_2-

saturated electrolyte corresponds to the electrochemical reduction of oxygen to water. Glassy carbon (Figure 4A) shows a similar peak at 0.65 V_{RHE} in O_2-saturated electrolyte; however, the total current is half the value observed for G-ANF samples.

A comparison of the ORR cathodic sweeps obtained using the rotating-disk electrode (RDE) method is shown in Figure 5.

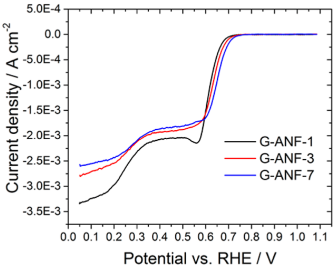

Figure 5. Cathodic voltammetric waves of G-ANF-1 (black line), G-ANF-3 (red line), and G-ANF-7 (blue line) recorded in O_2-saturated 0.1 M KOH between 0.05 and 1.1 V_{RHE} at 0.05 V s^{-1}, 900 rpm, and 25 °C. All waves are shown after subtraction of capacitive contributions.

All samples exhibit a two-step reduction: one around 0.75 V_{RHE} and another one around 0.35 V_{RHE} corresponding to a two-step electrochemical reduction of O_2 to H_2O.[9] All samples exhibit a plateau in the range 0.35−0.55 V_{RHE}, similar to a limiting current. The region between 0.35 and 0.55 V_{RHE} is diffusion-controlled, and the measured current is directly proportional to the number of electrons and rotation speed (see Koutecky−Levich section in the Supporting Information).[35,36] For curves obtained at the same rotation speed, a higher current indicates greater selectivity toward the four-electron reduction of oxygen to water. The highest current density at 0.4 V_{RHE} was observed for G-ANF-1 electrodes, indicating a higher selectivity toward the four-electron reduction of oxygen as explained in the Koutecky−Levich section of the Supporting Information. All samples were found to display mixed 2e/4e kinetics; trends in the average electron numbers, which are summarized in Table 2, suggest that whereas G-ANF-7 and G-ANF-3 favor the production of hydrogen peroxide (2e reduction), G-ANF-1 favors a 4e reduction of oxygen to water. The observation of higher electron numbers for G-ANF-1 is somewhat surprising, considering that morphological studies show that G-ANF-1 consists of a relatively smooth carbon coating without visible evidence of a high density of reactive GE structures.

The potential at 0.1 mA cm^{-2}, also known as onset potential, averaged over six independent measurements was found to be similar for all samples, as reported in Table 2. The potentials at half-current were also found to be comparable among all samples. The most noticeable difference among the electrodes was observed for the kinetic current densities determined as shown in the Supporting Information. The mass-transport-corrected kinetic current density was determined using the following formula in the Koutecky−Levich plots (Figure S3 in the Supporting Information):

$$\frac{1}{j} = \frac{1}{j_k} + \frac{1}{B\omega^{1/2}} \tag{1}$$

where j is the measured current, j_k is the kinetic current, B is the Levich constant, and ω is the angular velocity. The linear extrapolation on the y axis yields the reciprocal kinetic current at infinite rotation. G-ANF-7 yielded the highest kinetic current density, followed by G-ANF-3 and G-ANF-1. It is important to consider, however, that despite all samples possessing identical geometric area and mass loading, the carbon mass loading is different for the three G-ANFs: G-ANF-7 has the highest carbon ratio, while G-ANF-1 has the lowest carbon ratio (Figure S2 in the Supporting Information). Therefore, to compare activity among samples, the kinetic current density was normalized by the carbon mass, which is the electroactive fraction of the material, to obtain a mass activity, in analogy to that obtained for carbon-supported catalysts.[37,38] When mass-normalized kinetic currents were compared, G-ANF-1 was found to possess the highest electrocatalytic activity.

It is interesting to note that the trends in reactivity point at G-ANF-1 as the material that shows greatest catalytic activity; this is in agreement with an analysis of Raman spectra, which suggests that G-ANF-1 is the most defective of the three graphene-coated fibers and therefore likely to be the most edge-rich among them. However, Raman does not provide information on the amount of edges that are actually available at the carbon/electrolyte interface, as it takes into account also the carbon−alumina interface, which is likely distorted or defect-rich. In order to directly compare the density of electrochemically exposed GEs among the three materials, intercalation studies using 4-nitrobenzylamine (4-NBA) were carried out.[27] This method was developed by Compton and co-workers[27] for graphite and carbon nanotubes and has previously been used in our laboratory for comparing exposed GE densities at amorphous carbon electrodes.[28] Briefly, partial intercalation of 4-NBA occurs at GEs where the interlayer spacing in graphite does not allow for a full intercalation, thus leaving nitroaryl moieties exposed to the electrolyte and available for electroreduction to arylamines. The integrated electroreduction currents can then be used to compare relative GE densities among the samples.

Figure 6A shows the first two cycles in the CV of intercalated G-ANF-1 in 0.1 M H_2SO_4. The CV starts at large potentials, 1.2 V_{RHE}, and is featureless until it reaches 0.15 V_{RHE}, where the reduction of $Ph\text{-}NO_2$ takes place until approximately −0.2 V_{RHE}. This peak can be observed only in the first scan, and it corresponds to the reduction of the aromatic nitro compound.[27] In the following scan, there is only a pair of peaks at ~0.6 V_{RHE}, which appear to be quasi-reversible and can be attributed to the formation of Ar-NHOH.[27,39]

Table 2. Summary of Kinetic Data As Obtained from Hydrodynamic Voltammograms

	onset potential[a] (V)	potential at half-current (V)	kinetic current density (mA cm^{-2})	mass activity (A g^{-1})	no. of electrons
G-ANF-1	0.73 ± 0.01	0.63 ± 0.01	1.3 ± 0.2	35.0	3.2 ± 0.3
G-ANF-3	0.72 ± 0.01	0.63 ± 0.01	1.8 ± 0.2	11.6	2.6 ± 0.5
G-ANF-7	0.73 ± 0.01	0.65 ± 0.01	2.3 ± 0.3	12.8	2.5 ± 0.6

[a] Potential at which the current is 0.1 mA cm^{-2}.

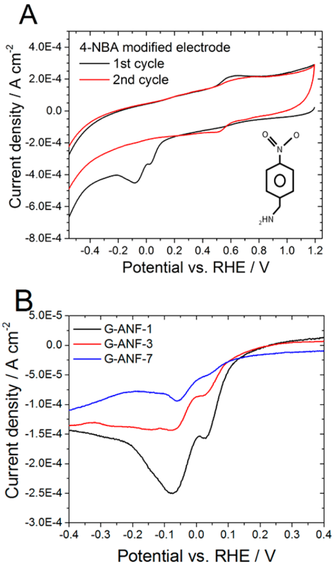

Figure 6. Cyclic voltammetric scans of a 4-NBA modified electrode (A) and 4-NBA modified G-ANF-1 (black line), G-ANF-3 (red line), and G-ANF-7 (blue line) (B) recorded in Ar-saturated 0.1 M H_2SO_4 between 1.2 and −0.8 V_{RHE} at 0.2 V s^{-1}. Curves in (B) are shown after correction by background current to facilitate comparison.

The voltammetric response for G-ANF-1 is significantly larger than those for the other two materials, and correspondingly, the largest electroreduction charge per unit area was found to be associated with G-ANF-1. Integration of the reduction peak yields surface coverage for 4-NBA, Γ_{NBA}, of (4.79 ± 0.8), (3.22 ± 0.73), and (2.75 ± 1.1) × 10^{-11} mol cm^{-2} for G-ANF-1, G-ANF-3, and G-ANF-7, respectively. The obtained values of Γ_{NBA} for G-ANF-3 and G-ANF-7 are similar; however, there is a considerable difference in comparison to G-ANF-1. The highest Γ_{NBA} value observed for G-ANF-1 indicates that the density of exposed GEs for this electrode is the highest among the three.

Analysis via microscopy would suggest that G-ANF-3 and G-ANF-7 are richer in graphitic edges, given the abundant presence of foliates at the carbon surface; XPS analysis also indicated that G-ANF-3 and G-ANF-7 are richer in sp^2 content than G-ANF-1. Accordingly, on the basis of typical trends in carbon electrodes,[11] G-ANF-3 and G-ANF-7 could have been expected to display faster charge transfer than G-ANF-1 and higher electrocatalytic activity toward the ORR.[17] Nevertheless, Raman spectroscopy showed that G-ANF-1 is the richest in defects among the three materials; these defects are likely to be in the form of edges/boundaries on the basal graphene plane and are not visible via microscopy. Raman spectroscopy cannot distinguish among electroactive and electroinactive defect sites.

In contrast, the partial intercalation of 4-NBA directly probes GEs exposed at the carbon/electrolyte interface. This method provides information on electroactive sites and takes into account defects and GEs that directly and unambiguously contribute to the electrochemical performance of the material; this method was found to indeed correlate positively with ORR activity (see Figure S5 in the Supporting Information). The use of electrochemical tools that can directly probe the role of structural changes on reactions at the carbon/electrolyte interface appear to thus be essential to complement microscopy and to accurately relate carbon properties to electrocatalytic activity.

It should be noted that the values of onset potential and potential half-maximum obtained for ORR at G-ANFs are similar to values reported for heteroatom-doped graphene and carbon nanotube composites.[17,40] Our results reveal that it is possible to modulate ORR activity and achieve high onset potentials by manipulating the properties of the carbon matrix exclusively, in the absence of heteroatom dopants. This suggests that the kinetics are not governed by heteroatom doping levels alone but that the carbon matrix structure can critically affect catalytic activity and potentially mimic or mask the effects of any chemical doping of the carbon material. Therefore, these findings indicate that it is important to conduct experiments at undoped, pure carbon electrodes with different carbon matrix properties such as GE density to elucidate the individual roles of chemical site and carbon matrix.

CONCLUSIONS

A CVD technique was used to grow carbon electrode materials with three different morphologies. XPS revealed that the material was highly graphitic in content, whereas scanning and transmission electron microscopy showed that in the initial deposition stage the substrate was wrapped by a few layers of graphene while longer synthesis times produced nanocarbons with a high density of protrusions with exposed few-layer graphene. A long CVD deposition time also results in a thicker and less defective carbon phase.

This growth method was used to fabricate three different types of electrodes that allowed us to investigate the role of defects and edges in ORR catalysis at undoped carbon electrodes. All three materials were found to display ORR onset potentials that are comparable to those of many N-doped carbon materials reported in the literature. Interestingly, the material that appears to be morphologically smooth when examined via microscopy was found to be the best performer in terms of mass activity and number of electrons involved in the reduction process. Raman and electrochemical intercalation studies suggest that this is the most defect-/edge-rich material, a structural difference that we propose accounts for its higher ORR activity. An important implication of these results is the fact that it is possible to modulate ORR activity through control of the carbon matrix to achieve catalytic performance comparable to that obtained via heteroatom doping. A careful study of matrix and doping effects in isolation might therefore be necessary to fully understand synergistic matrix-dopant effects in the ORR and to translate those into the tailored design of metal-free ORR catalysts. Such studies are necessary for building a rational foundation for the tailoring of carbon electrode materials for Pt-free electrocatalysis of the oxygen reduction reaction in polymer electrolyte fuel cells, metal−air batteries, and similar technologies.

ASSOCIATED CONTENT

Supporting Information

The Supporting Information is available free of charge on the ACS Publications website at DOI: 10.1021/acscatal.6b00945.

Calibration of Hydroflex reference against RHE, thermogravimetric analysis, O 1s spectra, Koutecky–Levich plots, and intercalation data (PDF)

AUTHOR INFORMATION

Corresponding Author

*E-mail for P.E.C.: colavitp@tcd.ie.

Present Address

‖J. Heyrovsky Institute of Physical Chemistry of the CAS, Prague, Czech Republic.

Notes

The authors declare no competing financial interest.

ACKNOWLEDGMENTS

This publication has emanated from research conducted with the financial support of Science Foundation Ireland under Grant Number 13/CDA/2213. This research was also supported by the Estonian Research Council under PUT1063 (I.H.). Use of the XPS instrument of I. V. Shvets and C. McGuinness was provided under SFI Equipment Infrastructure Funds. The authors acknowledge Dr. Valdek Mikli and Dr. Taavi Raadik, both from the Department of Materials Science, TUT, for their help with SEM imaging and Raman spectroscopy analysis. The authors are also grateful to Prof. W. Schmitt and Dr. A. Rafferty for access to instrumentation.

REFERENCES

(1) Wang, D.-W.; Su, D. *Energy Environ. Sci.* **2014**, *7*, 576−591.

(2) Trogadas, P.; Fuller, T. F.; Strasser, P. *Carbon* **2014**, *75*, 5−42.

(3) Arrigo, R.; Schuster, M. E.; Xie, Z.; Yi, Y.; Wowsnick, G.; Sun, L. L.; Hermann, K. E.; Friedrich, M.; Kast, P.; Hävecker, M.; Knop-Gericke, A.; Schlögl, R. *ACS Catal.* **2015**, *5*, 2740−2753.

(4) Ma, J.; Habrioux, A.; Alonso-Vante, N. *ChemElectroChem* **2014**, *1*, 37−46.

(5) Perini, L.; Durante, C.; Favaro, M.; Perazzolo, V.; Agnoli, S.; Schneider, O.; Granozzi, G.; Gennaro, A. *ACS Appl. Mater. Interfaces* **2015**, *7*, 1170−1179.

(6) Rao, C. V.; Cabrera, C. R.; Ishikawa, Y. *J. Phys. Chem. Lett.* **2010**, *1*, 2622−2627.

(7) Zhang, L.; Xia, Z. *J. Phys. Chem. C* **2011**, *115*, 11170−11176.

(8) Wiggins-Camacho, J. D.; Stevenson, K. J. *J. Phys. Chem. C* **2009**, *113*, 19082−19090.

(9) Yang, Z.; Ren, J.; Zhang, Z.; Chen, X.; Guan, G.; Qiu, L.; Zhang, Y.; Peng, H. *Chem. Rev.* **2015**, *115*, 5159−5223.

(10) Maldonado, S.; Morin, S.; Stevenson, K. J. *Carbon* **2006**, *44*, 1429−1437.

(11) McCreery, R. L.; McDermott, M. T. *Anal. Chem.* **2012**, *84*, 2602−2605.

(12) Ubnoske, S. M.; Raut, A. S.; Brown, B.; Parker, C. B.; Stoner, B. R.; Glass, J. T. *J. Phys. Chem. C* **2014**, *118*, 16126−16132.

(13) Yoo, E.; Kim, J.; Hosono, E.; Zhou, H.-s.; Kudo, T.; Honma, I. *Nano Lett.* **2008**, *8*, 2277−2282.

(14) Yu, D.; Dai, L. *J. Phys. Chem. Lett.* **2010**, *1*, 467−470.

(15) Zhang, J.; Xia, Z.; Dai, L. *Sci. Adv.* **2015**, *1*, e1500564.

(16) Benson, J.; Xu, Q.; Wang, P.; Shen, Y.; Sun, L.; Wang, T.; Li, M.; Papakonstantinou, P. *ACS Appl. Mater. Interfaces* **2014**, *6*, 19726−19736.

(17) Deng, D.; Yu, L.; Pan, X.; Wang, S.; Chen, X.; Hu, P.; Sun, L.; Bao, X. *Chem. Commun.* **2011**, *47*, 10016−10018.

(18) Jeon, I.-Y.; Choi, H.-J.; Jung, S.-M.; Seo, J.-M.; Kim, M.-J.; Dai, L.; Baek, J.-B. *J. Am. Chem. Soc.* **2013**, *135*, 1386−1393.

(19) Chen, P.; Fryling, M. A.; McCreery, R. L. *Anal. Chem.* **1995**, *67*, 3115−3122.

(20) Aghayan, M.; Hussainova, I.; Gasik, M.; Kutuzov, M.; Friman, M. *Thermochim. Acta* **2013**, *574*, 140−144.

(21) Ivanov, R.; Hussainova, I.; Aghayan, M.; Drozdova, M.; Pérez-Coll, D.; Rodríguez, M. A.; Rubio-Marcos, F. *J. Eur. Ceram. Soc.* **2015**, *35*, 4017−4021.

(22) Ivanov, R.; Mikli, V.; Kübarsepp, J.; Hussainova, I. *Key Eng. Mater.* **2016**, *674*, 77−80.

(23) Ferrari, A. C.; Basko, D. M. *Nat. Nanotechnol.* **2013**, *8*, 235−246.

(24) Peng, Z.; Wu, J.; Yang, H. *Chem. Mater.* **2010**, *22*, 1098−1106.

(25) Wu, G.; More, K. L.; Johnston, C. M.; Zelenay, P. *Science* **2011**, *332*, 443−447.

(26) Biddinger, E. J.; Ozkan, U. S. *J. Phys. Chem. C* **2010**, *114*, 15306−15314.

(27) Wildgoose, G. G.; Wilkins, S. J.; Williams, G. R.; France, R. R.; Carnahan, D. L.; Jiang, L.; Jones, T. G. J.; Compton, R. G. *ChemPhysChem* **2005**, *6*, 352−362.

(28) Cullen, R. J.; Jayasundara, D. R.; Soldi, L.; Cheng, J. J.; Dufaure, G.; Colavita, P. E. *Chem. Mater.* **2012**, *24*, 1031−1040.

(29) Hussainova, I.; Ivanov, R.; Stamatin, S. N.; Anoshkin, I. V.; Skou, E. M.; Nasibulin, A. G. *Carbon* **2015**, *88*, 157−164.

(30) Ferrari, A. C. *Solid State Commun.* **2007**, *143*, 47−57.

(31) Jorio, A. *ISRN Nanotechnology* **2012**, *2012*, 234216.

(32) Banks, C. E.; Davies, T. J.; Wildgoose, G. G.; Compton, R. G. *Chem. Commun.* **2005**, 829−841.

(33) Kim, H.; Lee, K.; Woo, S. I.; Jung, Y. *Phys. Chem. Chem. Phys.* **2011**, *13*, 17505−17510.

(34) Yuan, W.; Zhou, Y.; Li, Y.; Li, C.; Peng, H.; Zhang, J.; Liu, Z.; Dai, L.; Shi, G. *Sci. Rep.* **2013**, *3*, 2248.

(35) Nikolic, J.; Expósito, E.; Iniesta, J.; González-Garcia, J.; Montiel, V. *J. Chem. Educ.* **2000**, *77*, 1191−1194.

(36) Schmidt, T. J.; Gasteiger, H. A.; Stäb, G. D.; Urban, P. M.; Kolb, D. M.; Behm, R. J. *J. Electrochem. Soc.* **1998**, *145*, 2354−2358.

(37) Mayrhofer, K. J. J.; Strmcnik, D.; Blizanac, B. B.; Stamenkovic, V.; Arenz, M.; Markovic, N. M. *Electrochim. Acta* **2008**, *53*, 3181−3188.

(38) Stamatin, S. N.; Borghei, M.; Andersen, S. M.; Veltze, S.; Ruiz, V.; Kauppinen, E.; Skou, E. M. *Int. J. Hydrogen Energy* **2014**, *39*, 8215−8224.

(39) Wain, A. J.; Lawrence, N. S.; Greene, P. R.; Wadhawan, J. D.; Compton, R. G. *Phys. Chem. Chem. Phys.* **2003**, *5*, 1867−1875.

(40) Higgins, D. C.; Hoque, M. A.; Hassan, F.; Choi, J.-Y.; Kim, B.; Chen, Z. *ACS Catal.* **2014**, *4*, 2734−2740.

PUBLICATION IV

Ivanov, R., Hussainova, I., Aghayan, M., Drozdova, M., Pérez-Coll, D., Rodríguez, M. A., Rubio-Marcosc, F., Graphene-encapsulated Aluminium Oxide Nanofibers as a Novel Type of Nanofillers for Electroconductive Ceramics. — *Journal of the European Ceramic Society*, 2015, 35(14), 4017–4021, doi:10.1016/j.jeurceramsoc.2015.06.011

Journal of the European Ceramic Society 35 (2015) 4017–4021

Contents lists available at www.sciencedirect.com

Journal of the European Ceramic Society

journal homepage: www.elsevier.com/locate/jeurceramsoc

Short communication

Graphene-encapsulated aluminium oxide nanofibers as a novel type of nanofillers for electroconductive ceramics

Roman Ivanov[a], Irina Hussainova[a,b], Marina Aghayan[a], Maria Drozdova[a], Domingo Pérez-Coll[c], Miguel A. Rodríguez[c], Fernando Rubio-Marcos[c,*]

[a] *Tallinn University of Technology, Department of Materials Engineering, Ehitajate 5, 19180 Tallinn, Estonia*
[b] *ITMO University, Kronverksky 49, St. Petersburg, 197101, Russian Federation*
[c] *Instituto de Cerámica y Vidrio, CSIC, 28049 Madrid, Spain*

ARTICLE INFO

Article history:
Received 25 May 2015
Received in revised form 9 June 2015
Accepted 10 June 2015
Available online 3 July 2015

Keywords:
Nanofiber
Graphene
Nanocomposite
Thermal analysis
Raman spectroscopy
SPS

ABSTRACT

Graphene has attracted tremendous research interest in recent years owing to its exceptional properties. We report the remarkable ability to transform an insulating material, such as Al_2O_3, into a highly conductive material by filling the matrix with alumina nanofibers encapsulated by multi-layered graphene. The fibers of 7 nm in diameter were covered by graphene by catalyst-free one-step CVD process for the first time. Coupling between graphene layers and Al_2O_3 nanofibers results in the development of a novel type of fillers for ceramics, which modify the intrinsic electrical properties of the insulating materials by addition of less than 1 wt.% of graphene into the ceramic matrix. We believe that the general strategy described in this study will open new avenues in developing of graphene–ceramic composites with enhanced electrical properties that can be then suitable for high-precision electrical discharge machining.

1. Introduction

Structural oxide ceramics are intensively used in industry for a wide variety of applications from high-speed cutting tools and wear resistance parts to dental implants and chemical and electrical insulators. Over the past few years, much effort has been forwarded to the development of carbon nanotubes (CNT) and/or graphene reinforced electroconductive ceramics [1–4]. Graphene, which is one-atom thick material, has become of a great scientific interest due to its exceptional thermal, mechanical and electrical properties [5]. Several layers of graphene form graphene platelets or multilayer graphene nanosheets with a large specific surface area and a thickness of up to 100 nm exhibit outstanding mechanical properties, which makes them excellent nanofillers/additives for ceramic-based composites [4,6,7]. To achieve the required characteristics of the composite, it is essential to homogenously disperse the reinforcement additive throughout the matrix, since its agglomeration deteriorates material reliability [8]. Dispersion of graphene platelets is still a challenge [8,9] motivating development of novel approaches for preparation of the ceramic–graphene composites. In this study, we propose a novel type of nano fillers representing alumina nanofibres encapsulated into a few layered graphene for fabrication of an electroconductive oxide ceramic composite.

While the majority of the works on the ceramic–graphene composites apply a top–down approach to graphene production, such as exfoliating graphite/graphite oxide (GO) with high energy milling or colloidal processing of graphene/GO, in this work a bottom-up method is introduced. The layers of graphene were grown on the surface of γ-alumina nanofibers (ANFCs) of a huge aspect ratio of 10^7 [10] with the help of a process of chemical vapour deposition (CVD).

In this communication, we herein propose a strategy for the *in situ* self-assembly of graphene-layers into a γ-Al_2O_3 nanofiber. Using this hierarchical structure allows for improved distribution of graphene and therefore the efficiency of use. To build this "*hierarchical structure*", we developed a simple one-step CVD method that uses a hot-walled chemical vapour deposition procedure at 1000 °C and atmospheric pressure [11], which is summarized in Fig. 1. It should be emphasized that Al_2O_3–ANFCs nanocomposite with graphene contents lower than 1 wt.% can exhibit a significant high electric response with an electrical conductivity as high as $106\,S\,m^{-1}$, which implies an improvement of ~12 magnitude orders with respect to Al_2O_3 without ANFCs.

---

* Corresponding author. Fax +34 917355843.
E-mail address: frmacos@icv.csic.es (F. Rubio-Marcos).

http://dx.doi.org/10.1016/j.jeurceramsoc.2015.06.011

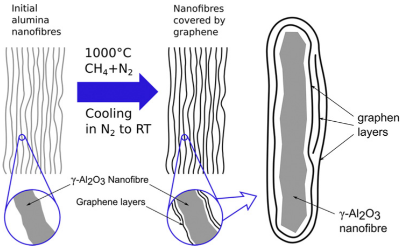

Fig. 1. Synthesis of the "*in situ*" self-assembly of graphene-layers into γ-Al_2O_3 nanofiber: Scheme of the CVD process of graphene layers growth on the surface of γ-Al_2O_3 nanofiber (ANFC) and the schematic representation of the nanofiller.

2. Experimental section

2.1. Direct synthesis of multi-layered graphene on γ-Al_2O_3 nanofiber

In situ self-assembly of graphene-layers onto a γ-Al_2O_3 nanofiber was synthetized by the hot-walled chemical vapour deposition procedure. Bundle of the aluminium oxide nanofibers (ANFs), used as a support and described in detail elsewhere [10–12] consists of the fibres with an average single fibre diameter of ~**7** nm and a length of 4–6 cm having a specific surface area of 155 $m^2 g^{-1}$. In this report, for the first time we demonstrate that ANFs can successfully serve as a substrate for the direct growth of few-layered graphene close shells around the dielectric fiber as sketched in Fig. 1. The graphene was deposited onto ANFs at temperatures up to 1000 °C by one-step CVD procedure using a mixture of nitrogen (N_2) and methane (CH_4). The covered alumina fibres were cooled down in a nitrogen flow to room temperature.

2.2. Morphology characterization

The "*hierarchical structure*" of the ANFCs, graphene layer size and morphology of both graphene layers and γ-Al_2O_3 nanofiber were examined using a JEOL 2100F transmission electron microscope (TEM/HRTEM) operating at 200 KV and equipped with a field emission electron gun providing a point resolution of 0.19 nm. The microscope coupled with an INCA *x*-sight energy dispersive X-ray spectrometer (EDXS), from Oxford Instruments, was used for chemical elemental analysis.

2.3. Thermal characterization

A differential thermal (DTA) and thermo-gravimetric analysis (TG) are carried out in a SETARAM, SETSYS 16/18 system in air. Thermal behaviour of ANFCs was studied by simultaneous coupled thermo-gravimetric analysis and infrared spectroscopy (FT-IR) with a Nicolet 6700 combined with TG from TA Instruments SDT (Q600 model).

2.4. Raman spectroscopy

Raman spectroscopy was carried out at room temperature using a WITec Alpha-300R confocal Raman microscope with a 532 nm laser. A total of 20 measurements were done at different points of the sample to study. Collected spectra were analysed by using Witec Control Plus Software, and Raman mode positions were fit assuming a Lorentz peak shape.

2.5. Al_2O_3/ANFCs composite preparation

In order to prepare uniform and well dispersed nanocomposites, the ANFCs are sonicated in ethanol by stick ultrasound (Hielscher UP400S) for 1 hour at 400 watt and 24 kHz. The obtained suspension is treated in Teflon lined attrition mill for 1 h at 1500 rpm in ethanol with zirconia balls of 3 mm in diameter. Then, commercially available α-alumina nano-powder with an average particle size of 100 nm (TM-DAR, Taimei Chemicals Co., Japan) is added to the suspension and the slurry with ANFCs concentration of 10 wt.% is subjected to further attrition milling for 1 hour with a powder-to-ball weight ratio of 1:20. After milling the prepared mixture is dried at 65 °C for 24 h and sieved using 100-μm mesh. The resulting size of the fibres after treatment is determined by a laser scattering method with a Mastersizer S (Malvern) He-Ne laser of $\lambda = 632.8$ nm and is measured to be around 500 ± 100 nm. Then, the powder mixture of Al_2O_3-10 wt.% ANFCs (with a total graphene content of about 1 wt.%) is densified to > 97% using a SPS furnace (Dr. Sinter SPS-510CE, Japan) at 1380 °C with uniaxial pressure of 40 MPa for a dwell time of 10 min. The sintering process is conducted in N_2 atmosphere. For reference, full dense (>99%) monolithic alumina sample is prepared with the same sintering conditions. Obtained samples are 10 mm in diameter and about 6 mm thick.

2.6. Microstructural characterization

The distribution of ANFCs on the Al_2O_3/ANFCs mixture and microstructure of the ceramics were evaluated using a Field Emission Scanning Electron Microscope, FE-SEM (HITACHI S-4700, Japan).

2.7. Electrical properties

Room temperature electrical properties of the Al_2O_3/ANFCs nanocomposites and Al_2O_3 monolithic material were determined by a dc-four probe method. For this purpose, the external surfaces of cylindrical densified pellets, with 10 mm in diameter and about 6 mm in thickness, were covered with an Ag-conductive paste and dried at 100 °C. Internal Ag-electrodes were also prepared by painting two rings around the lateral surface with an approximate thickness of 1 mm and a separation of about 2.4 mm. The as-prepared four electrodes were attached with four independent Pt wires and covered with Ag paste to ensure a good electrical contact. Electrical measurements were performed by an Autolab PGSTAT302N potentiostat/galvanostat in galvanostatic mode. The desired dc current is forced to flow through the volume of the sample by applying the working and counter electrodes to the external circular surfaces of the sample by means of a pair of Pt wires. The voltage difference between the inner electrodes is read by the use of the other independent pair of Pt wires. Using the method the resistance (R) of the sample is calculated from the slope of the current–voltage (*I*–*V*) curves in the experimental range of 10–100 mA. The conductivity of the Al_2O_3/ANFCs nanocomposite is obtained by:

$$\sigma = \frac{L}{RA} \tag{1}$$

where σ is the conductivity L the distance between the Ag internal electrodes, and A is the cross-section area of the sample.

3. Results and discussion

TEM images (Figs. 2a–c) show that the deposited film consists of a few layers of graphene. From image in Fig. 2b, a clear contrast between the nanofibers (support) and the graphene layers is well distinguished; the fillers, therefore, may represent the devel-

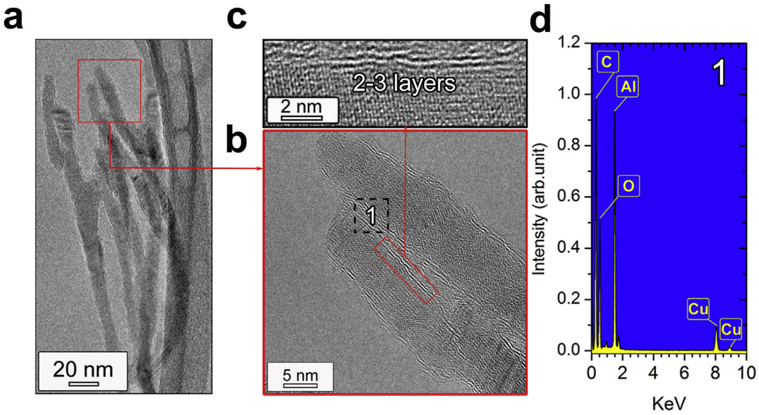

Fig. 2. Morphology characterization of the “*in situ*” self-assembly of graphene-layers into γ-Al_2O_3 nanofiber: (a-b) Series of HRTEM images corresponding to γ-Al_2O_3 nanofibers covered by graphene layers. (c) HRTEM image shows that the film on the γ-Al_2O_3 nanofibers mostly consists of less than a few layers of graphene. (d) EDX spectra corresponding to the area marked with “1” in part c.

opment of core–shell type nanostructures. Graphene layers with interspace of ca. 3–4 Å are rolled around nanofibres along a longitudinal axis. The HRTEM image (Fig. 2c) also reveals that the core-shell structure is mainly composed of 2–3 layers of graphene on alumina fiber. The composition is determined by Energy Dispersive Spectroscopy (EDS), as shown in Fig. 2d. As expected, mass gain of about 11% corresponds to 2–5 layers of graphene sheets. This fact is in accordance with the results previously established by HRTEM (Fig. 2c).

For composites manufacturing a thermal treatment at high temperatures is often required, making the thermal behaviour of the fillers to be a key factor. Therefore, to fabricate hybrid Al_2O_3/ANFCs composites, it is necessary to know the thermal behaviour of the isolated ANFC. Coupled thermal analysis of the base alumina nanofibers is thoroughly described elsewhere [10]. The results of thermal analysis are displayed in Fig. 3a and b. ANFCs mass loss is 2% of its initial weight after heating up to 200 °C. FT–IR spectra of the gases released at 100 °CC corresponds to water and CO_2, point marked as **1** in Fig. 3a and b. A sharp increase in gas flow at 100 °C, observed in Fig. 3a, is related to intensive water evaporation. The presence of CO_2 is explained by oxidation of a small amount of the amorphous carbon deposited on the fibres. Also, gradual weight loss of the fibres up to ~ 550 °C is accompanied by a slight exothermic effect caused by oxidation of the remaining amorphous carbon. Mahajan et al. [13] have observed a similar behaviour of MWCNTs under a partial oxygen atmosphere. The major weight loss (~7.5%) occurs between 400 and 550 °C (region contained between points **2** and **3** on the Fig. 3a and b), which is similar to the oxidation on MWCNTs in air where both amorphous carbon and graphene layers oxidize simultaneously. Increase in the absorbance peaks at 670 and 2300 cm^{-1} on the FT-IR spectra (Fig. 3b) corresponds to CO_2 states resulting from the intensive oxidation of a more stable “graphitized” carbon. This suggestion is confirmed by the appearance of an exothermic peak between 400 and 600 °C and a dramatic decrease in mass. In addition, gradual decrease in gas flow is observed up to 400 °C. At this point, the diminution of the gas flow is almost ceased indicating an onset of the active oxidation of a stable carbon. The following gases release is evidenced between 500 and 600 °C. Above 600 °C, a slight endothermic effect can be seen on the DTA curve, which is accompanied with an insignificant weight loss. It should be also noted that the bands corresponding to CO_2 decrease while bands corresponding to H_2O are still well recognizable at 800 °C, point signalled as **5** in Fig. 3a and b. Therefore, we suggest that the chemisorbed water (some kind of hydroxyls) evolves at the temperatures well above 600 °C. Besides, some morphological changes of γ-alumina phase discussed in the authors' previous work [10] are possible, which itself induces the endothermic effect.

The Raman spectrum of the specimen is presented in Fig. 3**c**. The main features in the spectra of sp^2 carbon structures are a

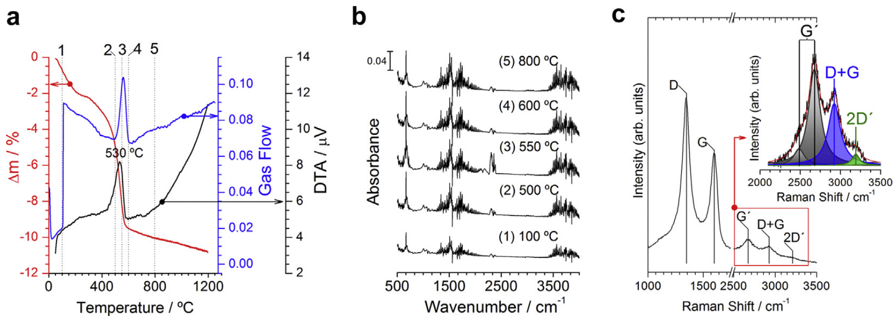

Fig. 3. (a) TG and DTA curves of ANFCs combined with gas flow curve recorded during FT-IR analysis of the gases emitted by ANFCs heating; (b) IR absorption spectra at selected temperatures; (c) Raman spectrum of ANFCs. The insert of panel c shows a detail of the Raman spectrum in the Raman Shift range from 2000 to 3500 cm^{-1} of the ANFC sample. This spectrum region is fitted to the sum of four Lorentzian peaks, which are indexed as 2G′ bands (in grey color), a 1 D + G band (in blue color) and a 2D′ band corresponding to the graphene layers (For interpretation of the references to color in this figure legend, the reader is referred to the web version of this article.).

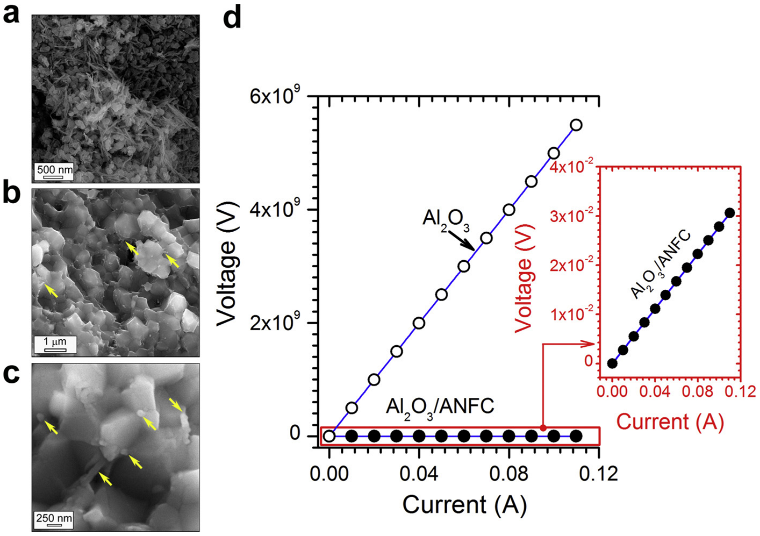

Fig. 4. Designing hybrid Al_2O_3/ANFCs nanocomposites with high electric response: (a) FE-SEM image of Al_2O_3-10 wt.% ANFCs powder. (b and c) FE-SEM images of the hybrid Al_2O_3/ANFCs nanocomposites sintered at 1380 °C. From panel c, it can be observed that the nanocomposites have an adequate interconnection between the ANFCs and the ceramic matrix without signs of ANFCs degradation. Some ANFCs are signalled with yellow arrows in b and c. (d) Current–Voltage (I–V) curves for Al_2O_3/ANFCs nanocomposites and Al_2O_3 monolithic material. The insert of panel c shows a detail of the I–V response for the Al_2O_3/ANFCs nanocomposites. **The electrical properties are the average values of five specimens with a standard tolerance of ±10%.*

well-recognized G and a disorder-induced D band at around 1350 and 1580 cm^{-1}, respectively [14,15]. Four remarkable peaks around 1340 cm^{-1}, 1600 cm^{-1}, 2680 cm^{-1} and 2930 cm^{-1} are observed in untreated ANFCs. In addition, a weak peak at 3180 cm^{-1} is found in Raman spectrum. Quite narrow bands suggest a nanocrystalline structure of the carbon deposited onto the fibres and the position of the G' band points to the presence of several layers of graphene [15]. In general, the Raman modes reflect the main features observed for MWCNT [16]. Actually, carbon nanotubes are essentially wrapped up graphene sheets and multi-walled tubes represent several layers of graphene rolled around the core tube. The intensity ratio between the D and G peaks, I_D/I_G, can be used for estimation of the amount of structural defects/edges and the degree of graphitization in graphitic materials [17]. In case of graphene covered ANF, the ratio I_D/I_G is around 1.2 pointing to a highly defective structure or presence of a large amount of open edges [15,17]. This is also emphasized by the (D + G) combination modes, band at ~2930 cm^{-1}, and the second order 2D′, band at ~3180 cm^{-1}. The G′ band is originated from a double-resonance process and can be fitted to a single Lorentzian for a monolayer graphene, while multiple bands in a multilayer graphene are represented by a complex band structure [14]. Deconvolution of the G' band, as it is shown in insert of Fig. 3c, indicates an increase in the number of layers associated to structural defects and/or open edges, as confirmed by HRTEM in Fig. 2c.

FE-SEM image of the dried suspension containing 10 wt.% of ANFCs is shown in Fig. 4a. The dried suspension of the Al_2O_3/ANFCs is composed of nanofibers interconnected with the alumina nanopowder matrix, Fig. 4a. In Fig. 4b and c, the FE-SEM images of the hybrid Al_2O_3/ANFCs nanocomposites sintered at 1380 °C is demonstrated. It is worth to note that the nanocomposite presents a homogeneous dispersion of the nanofibers within the ceramic matrix (Fig. 4b) without signs of ANFCs degradation (Fig. 4c). This fact provides a clear evidence for the excellent dispersion of the nanofibers within the matrix, forming an ANFCs network percolation**.**

The electrical conductivity of the Al_2O_3/ANFCs nanocomposite is 106 S m^{-1}, good enough for using it in the production of electroconductive ceramics, as shown in Fig. 4d. Hybrid Al_2O_3/ANFCs composite exhibits a huge increase in conductivity, σ, of ~12 orders of magnitude compared to the monolithic sample changing from highly insulating to conductive material (see Fig. 4d and Eq. (1)) because of the uniform ANFCs network percolation. Finally, it should be mentioned that the addition of small amounts of ANFCs also affects other properties. In this way, the nanocomposite of Al_2O_3/10 wt.% ANFCs exhibites non-deteriorated hardness of ~1415 ± 120 HV_5 as compared to the hardness of the reference monolithic alumina (1420 ± 180 HV_5), which was determined by Vickers indentations method (Indentec 5030 SKV).

To sum up, it is worth pointing out that this stimulant behaviour observed here could have potential technological applications because it could allow the use of high-precision electrical discharge machining in these ceramics. These findings undoubtedly could also be extended to other insulating ceramics such as zirconia or silicon nitride-based materials.

4. Conclusions

To conclude, we show the feasibility to generate graphene layers coating on γ-Al_2O_3 nanofiber (ANFC) by a simple one-step catalyst-free CVD method. Graphene encapsulated fibers can be used as nanofillers for enhancing electrical response of ceramic matrices. It has been possible to produce conductive samples by introducing small amount of graphene, lower than 1 wt.%, to create an electrical conductive network within the alumina matrix by means of a hierarchical structure strategy.

Acknowledgments

This work was supported by Institutional research funding IUT 19-29 of the Estonian Ministry of Education and Research.

Archimedes targeted grant AR12133 (NanoCom) and the European Social Fund's Doctoral Studies DoRa, which is carried out by Foundation Archimedes, are also gratefully appreciated for supporting this study. The authors also express their thanks to the MINECO (Spain) projects MAT2013-48009-C4-1-P, MAT2013-48426-C2-1-R and ENE2012-30929 for their financial support. Dr. F. Rubio-Marcos is also indebted to MINECO for a "Juan de la Cierva" contract (ref: JCI-2012-14521), which is co-financed with FEDER funds.

References

[1] X. Huang, X. Qi, F. Boey, H. Zhang, Graphene-based composites, Chem. Soc. Rev. 41 (2012) 666–686.
[2] G. Yamamoto, M. Omori, T. Hashida, H. Kimura, A novel structure for carbon nanotube reinforced alumina composites with improved mechanical properties, Nanotechnology 19 (2008) 315708.
[3] I. Hussainova, M. Drozdova, M. Aghayan, R. Ivanov, D. Pérez-Coll, Graphene covered alumina nanofibers as toughening agent in alumina ceramics, Adv. Sci. Technol. 88 (2014) 49–53.
[4] Y. Fan, L. Wang, J. Li, J. Li, S. Sun, F. Chen, L. Chen, W. Jiang, Preparation and electrical properties of graphene nanosheet/Al2O3 composites, Carbon N. Y. 48 (2010) 1743–1749, http://dx.doi.org/10.1016/j.carbon.2010.01.017
[5] V. Singh, D. Joung, L. Zhai, S. Das, S.I. Khondaker, S. Seal, Graphene based materials: past, present and future, Prog. Mater. Sci. 56 (2011) 1178–1271.
[6] J. Liu, H. Yan, M.J. Reece, K. Jiang, Toughening of zirconia/alumina composites by the addition of graphene platelets, J. Eur. Ceram. Soc. 32 (2012) 4185–4193.
[7] A. Centeno, V.G. Rocha, B. Alonso, A. Fernández, C.F. Gutierrez-Gonzalez, R. Torrecillas, A. Zurutuza, Graphene for tough and electroconductive alumina ceramics, J. Eur. Ceram. Soc. 33 (2013) 3201–3210.
[8] K. Narh a, L. Jallo, K.Y. Rhee, The effect of carbon nanotube agglomeration on the thermal and mechanical properties of polyethylene oxide, Polym. Compos. 29 (2008) 809–817.
[9] Y. Yang, W. Rigdon, X. Huang, X. Li, Enhancing graphene reinforcing potential in composites by hydrogen passivation induced dispersion, Sci. Rep. 3 (2013) 2086.
[10] M. Aghayan, I. Hussainova, M. Gasik, M. Kutuzov, M. Friman, Coupled thermal analysis of novel alumina nanofibers with ultrahigh aspect ratio, Thermochim. Acta (2013) 571.
[11] I. Hussainova, R. Ivanov, S.N. Stamatin, I.V. Anoshkin, E.M. Skou, A.G. Nasibulin, A few-layered graphene on alumina nanofibers for electrochemical energy conversion, Carbon 88 (2015) 157–164.
[12] M. Aghayan, N. Voltsihhin, M.A. Rodríguez, F. Rubio-Marcos, M. Dong, I. Hussainova, Functionalization of gamma-alumina nanofibers by alpha-alumina via solution combustion synthesis, Ceram. Int. 40 (2014) 12603–12607.
[13] A. Mahajan, A. Kingon, Á. Kukovecz, Z. Konya, P.M. Vilarinho, Studies on the thermal decomposition of multiwall carbon nanotubes under different atmospheres, Mater. Lett. 90 (2013) 165–168.
[14] A.C. Ferrari, J.C. Meyer, V. Scardaci, C. Casiraghi, M. Lazzeri, F. Mauri, S. Piscanec, D. Jiang, K.S. Novoselov, S. Roth, A.K. Geim, Raman spectrum of graphene and graphene layers, Phys. Rev. Lett. 97 (2006) 187401.
[15] A.C. Ferrari, D.M. Basko, Raman spectroscopy as a versatile tool for studying the properties of graphene, Nat. Nanotechnol. 8 (2013) 235–246.
[16] L. Bokobza, J.-L. Bruneel, M. Couzi, Raman spectroscopic investigation of carbon-based materials and their composites. Comparison between carbon nanotubes and carbon black, Chem. Phys. Lett. 590 (2013) 153–159.
[17] C. Casiraghi, A. Hartschuh, H. Qian, S. Pliscanec, C. Georgia, A. Fasoli, K.S. Novoselov, D.M. Basko, A.C. Ferrari, Raman spectroscopy of graphene edges, Nano Lett. 9 (2009) 1433–1441.

PUBLICATION V

Kazantseva, J., **Ivanov, R.**, Gasik, M., Neuman, T., Hussainova, I., Graphene-augmented nanofiber scaffolds demonstrate new features in cells behaviour. — *Scientific Reports*, 2016, 6, 30150, doi:10.1038/srep30150

www.nature.com/scientificreports

SCIENTIFIC REPORTS

OPEN

Graphene-augmented nanofiber scaffolds demonstrate new features in cells behaviour

Received: 23 May 2016
Accepted: 27 June 2016
Published: 22 July 2016

Jekaterina Kazantseva[1], Roman Ivanov[2], Michael Gasik[3], Toomas Neuman[1,4] & Irina Hussainova[2,5]

Three-dimensional (3D) customized scaffolds capable to mimic a native extracellular matrix open new frontiers in cells manipulation and advanced therapy. The major challenge is in a proper substrate for *in vitro* models on engineered scaffolds, capable to modulate cells differentiation. Here for the first time we demonstrate novel design and functionality of the 3D porous scaffolds of aligned, self-assembled ceramic nanofibers of ultra-high anisotropy ratio (~10^7), augmented into graphene shells. This unique hybrid nano-network allows an exceptional combination of selective guidance stimuli of stem cells differentiation, immune reactions variations, and local immobilization of cancer cells, which was not available before. The scaffolds were shown to be able to direct human mesenchymal stem cells (important for stimulation of neuronal and muscle cells) preferential orientation, to suppress major inflammatory factors, and to localize cancer cells; all without additions of specific culture media. The selective downregulation of specific cytokines is anticipated as a new tool for understanding of human immune system and ways of treatment of associated diseases. The effects observed are self-regulated by cells only, without side effects, usually arising from use of external factors. New scaffolds may open new horizons for stem cells fate control such as towards axons and neurites regeneration (Alzheimer's disease) as well as cancer therapy development.

Regenerative medicine and tissue engineering as well as cell therapy represent a breakthrough change in paradigm in healthcare compared to traditional pharmacology and implantology[1]. The role of proper *in vitro* protocols and systems for cells and drugs research is vital in creation of cost-effective and scientifically validated treatment methods, at the same time implementing expensive and scattered animal studies (known as "refinement, reduction, replacement" – the "3R"), and long, even more expensive clinical trials. For realization of efficient cells adhesion, proliferation, morphogenesis and differentiation, scaffolds should properly mimic natural *in vivo* microenvironments and signals, and offer correct local conditions needed for the regulation of vital cellular functions[1–4]. Besides biochemical factors, the surface and topography of a scaffold affects greatly stem cell fate[3] (for example, a fibrous scaffold was found to increase neural stem cell oligodendrocyte differentiation as well as greatly improve neurite extension and gene expression for neural markers[4]). As another example, scaffolds with conductive surfaces can promote human mesenchymal stem cells (hMSC) differentiation towards electro-active lineages[3–5], opening new scenarios for regeneration of neural, cardiac and similar tissues, capable to assist drug research *in vitro*.

Recently graphene became an important material in cellular studies and tissue engineering applications due to its extraordinary properties[6–11]. However, non-modified graphene materials have shown increased cellular toxicity and a high degree of agglomeration in aqueous medium[12], which limits their direct practical applications in scaffolds. To overcome these limitations, graphene is usually subjected to a substantial chemical modification (introduction of oxy- and hydroxyl groups and probably grafting of some organic molecules) to be combined with desired properties and bio-functionality[13].

For the first time, we report here graphene-augmented inorganic nanofibres (GAIN) scaffolds with tailored mechanical anisotropy, fibres size, orientation and porosity. These 3D hybrid GAIN scaffolds are shown to be

[1]Cellin Technologies LLC, Tallinn, Estonia. [2]Department of materials engineering, Tallinn University of Technology, Tallinn, Estonia. [3]School of Chemistry Technology, Aalto University Foundation, Espoo, Finland. [4]Protobios LLC, Tallinn, Estonia. [5]ITMO University, St. Petersburg, Russian Federation. Correspondence and requests for materials should be addressed to M.G. (email: michael.gasik@aalto.fi)

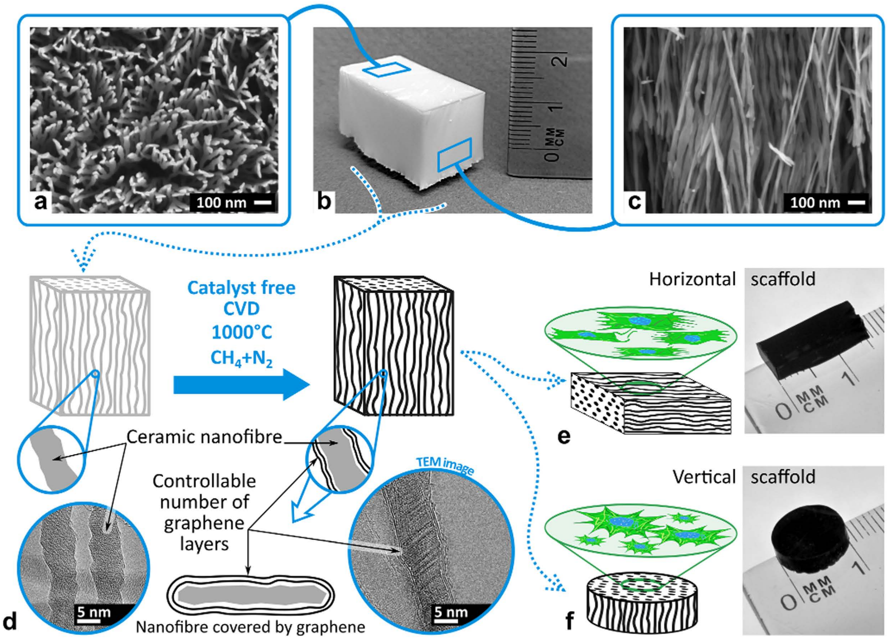

Figure 1. (**a**–**c**) The images of the graphene-augmented inorganic nanofibres (GAIN) network: (**a**) the top view (SEM) of GAIN revealing high porosity; (**b**) the network of the highly oriented nanofibres held together by weak hydrogen bonding; (**c**) the side view (SEM) of GAIN showing alignment of the fibres. (**d**) The schematic of the process of a single-step catalyst-free CVD of controllable number of "*in-situ*" self-assembly of graphene layers onto the surface of fibres using CH_4 gas as a source of carbon. (**e**) The GAIN scaffold with horizontally oriented fibres allowing directional orientation (estimated tangential compressive elastic modulus 200–400 GPa along the fibres and ~1–5 kPa across the nanofibres network) and altering morphology of different types of cells. (**f**) The GAIN scaffold with vertically oriented fibres allowing development of mixed tumour *in vitro* models 2D/3D configurations for inductive and conductive features, accomplish the selective propagation of tumour cells.

biocompatible and robust, well suitable for evaluation of cell studies, allowing previously unavailable features in the cell culture environments due to controlled ultra-high 3D anisotropy and surface variations.

Scaffolds for cells cultures

The unique self-assembled metal oxide fibres network with an average single-fiber diameter of ~40 nm (TEM, HRSEM) and length of 2–10 cm with 85–95% oriented porosity (BET; mercury porosimetry) was produced using bottom-up approach of controlled liquid phase oxidation[14] and employed as the substrate for graphene shells growth in a single-step process of novel catalyst-free chemical vapor deposition (CVD) at 1000 °C and atmospheric pressure using a mixture of nitrogen (N_2) and methane (CH_4) gases, Fig. 1. Recently, for the first time we demonstrated that alumina nanofibers can successfully serve as a substrate for the direct growth of few-layered graphene close shells around the dielectric fibre[15]. On the contrary to many other studies, graphene on the nanofibres was not functionalized in any way and became augmented to the underlying oxide fiber surface during the manufacturing process.

For cells behavior analysis (stem cells proliferation and fate; cancer cells attachment and growth; gene expressions variations, etc.), many properties of 3D scaffolds are essential. For example, substrate stiffness and topology are well known to modulate primary cells shape and morphology with conditions required for further specific differentiation. However, their explicit interactions of material single features with cells and ECM system are usually too complex to allow separation of specific parameters contribution to a reliable extent.

Stem cells evolution

Firstly, we explored potential use of GAIN scaffolds for tissue engineering applications by studying *in vitro* the growth, proliferation and especially orientation of adipose-derived hMSC. The morphology, adhesion and distribution of viable hMSC after 3 days of culture on horizontally oriented GAIN scaffolds and on control are demonstrated in Fig. 2. GAIN scaffolds were seen clearly guiding cells to line up along the fibres with a spindle-like shape and more than usually elongated cytoplasmic lamellipodia extensions. High aspect ratio cellular orientations are developed throughout the GAIN scaffold (Fig. 2b) allowing directional connection between individual cells and formation of cells network. Thus non-modified, augmented graphene on GAIN scaffolds does not impede the

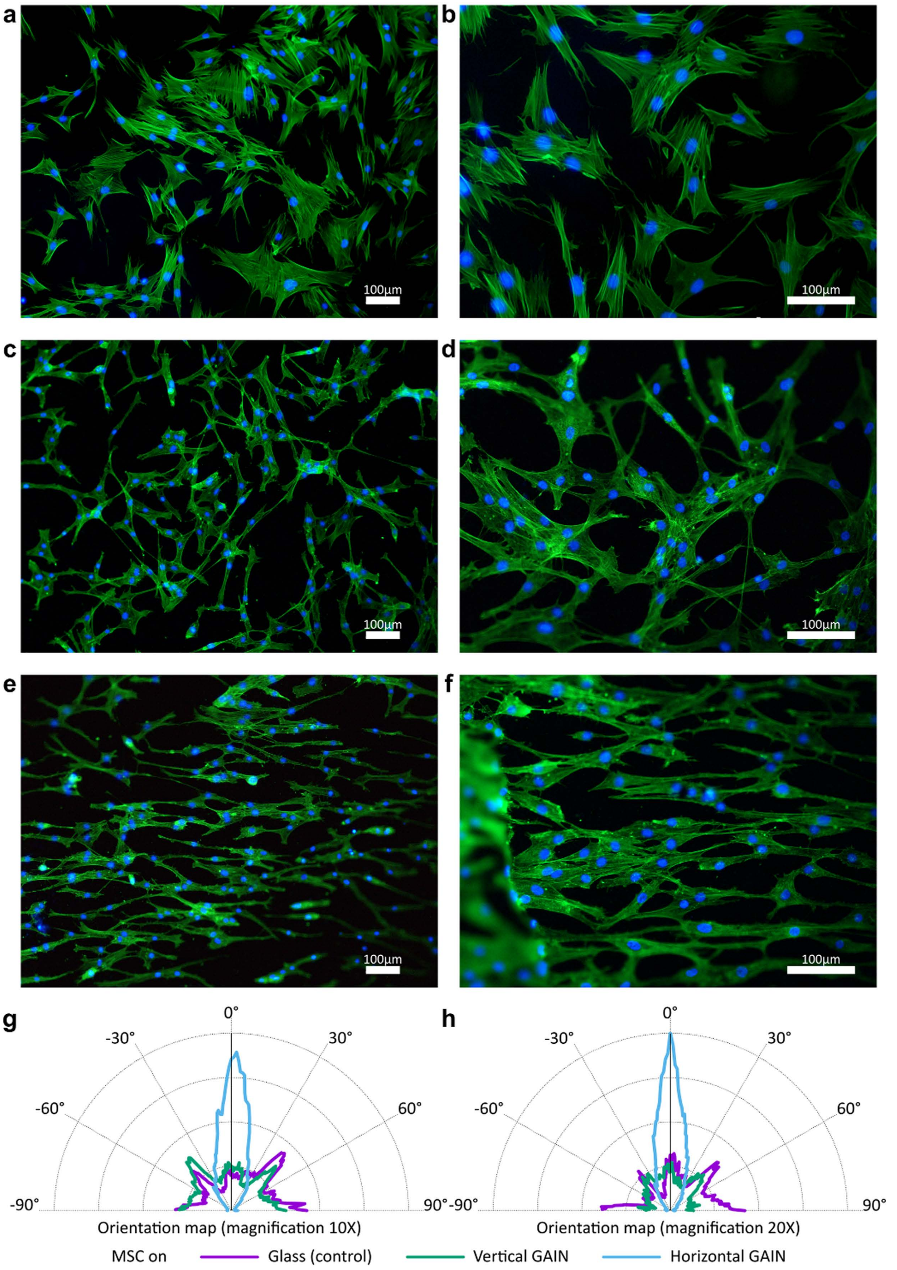

Figure 2. Fluorescence microscopy images (two different magnifications) of hMSC on control (glass, **a**,**b**), GAIN vertical (**c**,**d**) and GAIN horizontal (**e**,**f**) scaffolds. The preferential orientation comparison (**g**,**h**) indicates several times higher anisotropy for GAIN-seeded hMSC.

normal growth of stem cells. Furthermore, elongated morphology of hMSC and its high polarization (Fig. 2c) create pre-requisites for preferential specific (e. g. neuronal or myogenic) lineage differentiation.

Elastic properties of the scaffold substrate (stiffness and viscoelasticity) play a definitive role in stem cells behaviour[16]. For example, elastic modulus range of ~1 kPa is known to promote differentiation especially into neural cells and their growth[17], as it is close to the neural and brain tissue stiffness. For GAIN scaffolds, the tangential elastic modulus anisotropy (Fig. 1) is about 400 GPa/5 kPa = $80 \cdot 10^6$, which variation range covers elasticity

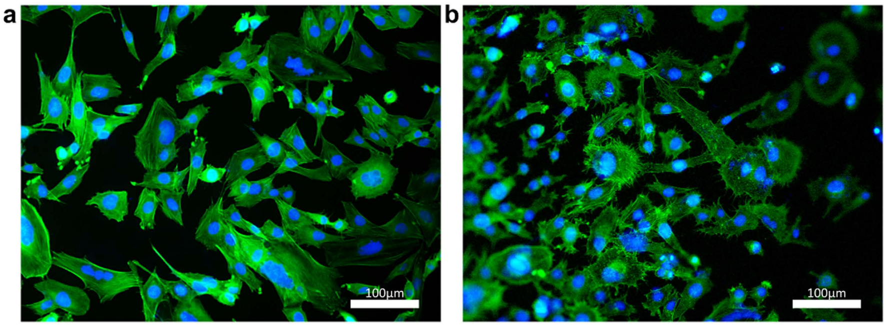

Figure 3. Fluorescent images of breast cancer cell line MDA-MB 231 showing the morphological changes of cells grown on control glass (**a**) and horizontal GAIN scaffolds (**b**), with evident increased number of microspikes and initial stages of cytoplasm infiltration into the scaffolds supposing high membrane activity.

of actin filaments involved in cells adhesion and taxis (the elastic modulus of F-actin was reported[14] to be close to 2 GPa). At the same time, diameter of the nanofibres in GAIN scaffolds (Fig. 1) is ~40 nm (500–1000 times smaller than average cell size), but compatible to the size[14] of actin filaments spacing (20–30 nm). Thus, one cell filament can be bound to exactly one nanofiber in orthogonal direction, but many filaments can attach to one nanofiber along its longer length. In terms of adhesion process, cell membrane compliance and elasticity would cause substantially larger displacement of nanofibres in perpendicular direction whereas in parallel to nanofibres the cell membrane would face substantially larger stress and therefore undergo much higher deformation.

Whereas response of stem cells to different substrate stiffness was studied earlier, to our best knowledge, the effect of such ultra-high local modulus anisotropy in 3D nanofibers was not previously reported. One of the reasons is that most of nanofibre-based scaffolds are randomly oriented or loosely packed, making a 3D nanostructure with not such stiffness anisotropy. Many aligned fibrous scaffolds are made of polymer fibres, which intrinsic elastic modulus is less than oxide ceramics by few orders of magnitude. The effect observed at GAIN scaffolds differs also substantially from known nanotopology studies, where nano-grooves or other patterns are known to support cell alignment, but without huge local differences in substrate stiffness anisotropy.

We suggest that "durotaxis" effect[16–18] drives hMSC along the stiffer scaffold direction, whereas orthogonally it leads to local confining of parallel nanofibres due to traction force expressed by the cell membrane. Dynamically crawling cell may create periodic contraction and expansion of nanofibres across the cell main direction. Such "nanopump" in GAIN scaffolds allows more intensive local media flow ensuring better nutrients and oxygen supply thus supporting the cell own metabolic processes.

Tumour models

The second application of GAIN scaffolds was demonstrated for cancer cells growth. Breast cancer cell line MDA-MB231 was seeded on the vertical and horizontal fibres of the GAIN scaffolds (Fig. 1). Cancer cells cultured on GAIN possess extended microspikes and actin-rich filopodia protrusions suggesting high level of membrane activity and malignant migratory cancer phenotype (Fig. 3). The initial signs of cancer cell infiltration (and hence local immobilization of the cells) were detected on vertical fibres allowing suggestion of 3D cancer model. Observed cancer cell infiltration, their clearly reduced mobility and extended filopodia formation, GAIN scaffold creates more representative phenotype to obtain 3D *in vitro* cancer model, mimicking tumour genesis more accurately.

The unique composition and structure of GAIN scaffolds creates a microenvironment, which fundamentally contrasts with such for tumour cells grown on 2D morphology. These effects assertively cause different expression of oncogenes and tumour suppressor genes[19]. In general, the behaviour of cancer cells on GAIN scaffolds differs from 2D culture and can be used as a tool for anti-cancer drug development or in cancer stem cell (CSC) studies, as the proportion of CSC has been shown significantly greater for 3D system[20].

Inflammatory response

In the third challenge, the inflammatory response of GAIN scaffolds was considered. Immunological profiling of any material under the influence of *in vivo* or *in vitro* environment is an important content of biocompatibility evaluation and has a critical value for future clinical translation. In addition to hMSC, this was also assessed with peripheral blood mononuclear cells (PBMCs) as they are an important part of the human peripheral immune system, responsible for transforming of the multitude of external stimuli to generate an adaptive immune response.

Observed unimpaired nuclei morphology of hMSC (Fig. 2) indicates no cytotoxicity for GAIN scaffolds. Then, hMSC and PBMC were grown on the GAIN scaffolds and tissue culture plastic (control) *in vitro,* and their inflammatory signatures were compared (Fig. 4). We analyzed the mRNA expression of genes involved in the immune reaction and a secretion of cytokines (IL1ß, TNFα, IFNγ, IL6, IL8, IL2, IL4, IL12ß, and CCL2).

For PBMC, clear downregulation of pro-inflammatory *TNF, IL1B, IL12B, IL6, CCL2* and *COX2* cytokines was detected, demonstrating the strong GAIN ability to modulate immune response. Among the upregulated inflammatory genes in GAIN microenvironment *CCL18, IL1RN, IDO1* and *TGFß1* factors were observed. These

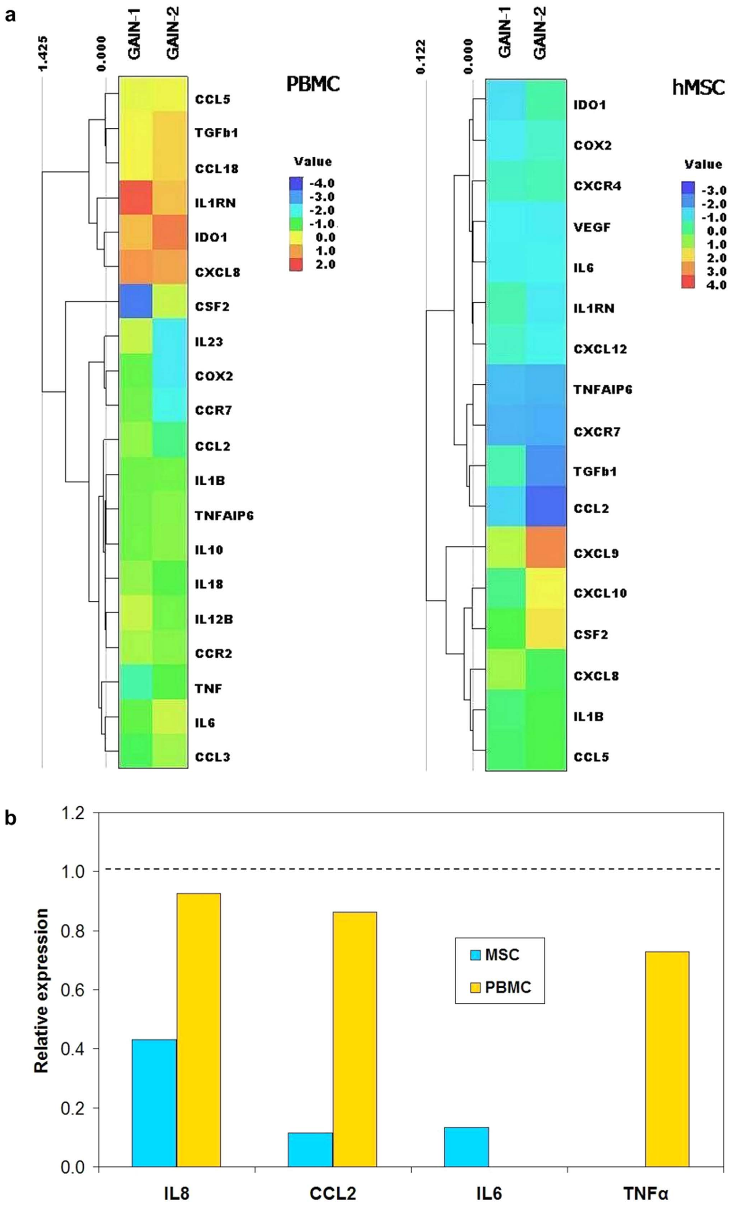

Figure 4. The immunologic profile impact on GAIN scaffolds for hMSCs and PBMCs (incubated for 24 h) with the inflammatory signature compared to the cells without the scaffold (control). (**a**) mRNA expression of genes responsible for immune reaction (quantitative real-time polymerase chain reaction, RT-qPCR). The results are represented as a heat map for two independent set of measurements on separate GAIN scaffolds, revealing simultaneously row hierarchical cluster structure in a data matrix with the location of the respective tiles near each other telling about similarity in the respective gene expression groups. (**b**) Secretion of some important cytokines (enzyme-linked immunosorbent assay, ELISA), normalized to the control cells expression and displayed as a histogram, where dashed line corresponds to the expression level of cytokines in the control cells.

factors commonly participate in anti-inflammatory response, pointing out to the possible immunomodulating effect of the GAIN scaffolds. For hMSCs, the promoted mRNA expression of *CXCL8, CXCL9, CXCL10* and *CSF2*, the chemokines participating in neutrophil, monocyte or leukocyte trafficking, were observed, indicating the possible changes in chemotaxis in response to the GAIN. Additionally, reduced expression of *COX2, CCL2* and *IL6* cytokines indicates a good immune tolerance of the GAIN material.

Analysis of cytokines secretion by ELISA (Fig. 4b) also demonstrated the reduced levels of TNFα, IL6, IL8/CXCL8, and CCL2 expression and total absence of secretion of pro-inflammatory IL1ß, IFNγ, IL2, IL4 and IL12 cytokines by both cell types assuming immuno-indifferent impact of the materials.

The main transcript induced in response to scaffold microenvironment for both cell types was *CXCL8*, but the secretion of this cytokine in medium was reduced comparing the control. Although *CXCL8* can be involved into the initiation of acute inflammatory processes, the global immunologic signature was undoubtedly immuno-tolerant. The heightened expression of IL1RN and IDO1 together with the elevated levels of CCL18 and TGFß1 in PBMCs (Fig. 4a) also has confirmed the immunoregulatory function of the GAIN.

Conclusions

Unique properties of GAIN scaffolds provide an improved capacity in enhancing hMSC alignment without additional manipulations. GAIN provides a suitable engineering microenvironment of nanotopological features, transducting physical cues with a high positive impact on a possible cell differentiation fate, which is of a paramount importance for cell therapy. Moreover, GAIN scaffolds positively affect immunological behaviour of hMSC and PBMC, with specific regulation of cytokines, revealing immuno-tolerant nature of the materials. The unique behaviour of studied breast cancer cells on GAIN scaffolds and their immobilization *in loco* open new frontiers in advanced materials for 3D tumour growth modelling systems and anticancer therapy development.

Methods

Cell cultures. Human MSCs were obtained from freshly isolated subcutaneous adipose tissue and characterized as previously reported[21]. Human breast cancer cell line MDA-MB 231 was purchased from ATCC. Cells were grown in DMEM with 10% FBS, 1 mg/ml penicillin and 0.1 mg/ml streptomycin at 37 °C in 5% CO_2. GAIN scaffolds were pre-treated for three days before the cells seeding by complete medium with changing the medium for fresh every 24 hours to saturate them by active components adsorbed from liquid phase.

Cells staining and visualisation. For visualisation of adipose-derived hMSCs and MDA-MB 231 on GAIN scaffold, we used specific to filamentous actin (F-actin) phalloidin tagged by FITC (Sigma). For hMSCs, pooled cells from three individuals with passage number below 5 were seeded on the scaffolds in 12-well plate (4×10^4 cells per well). For MDA-MB 231, 5×10^4 cells were added to the each well with scaffolds. Similar cells grown on a flat glass at the same density and cell culture conditions were considered as the controls. The cells were fixed by 4% PFA at 48 h after seeding, washed by PBS and permeabilized by 0.3% TRITON X-100 in PBS for 5 minutes. Phalloidin-FITC (1:100) staining lasted for 18 h at 4 °C for GAIN scaffolds and 2 h at RT for controls. To stain the cells nucleus, cells were incubated for 10 minutes with Hoechst 33342 (Invitrogen, 1 μg/ml). After a final wash, the phalloidin-stained cells were analysed by Nikon Eclipse 80i microscope.

Cells orientation analysis. Since hMSC are capable of self-renewal and differentiation *in vitro* into multiple cell lineages depending on growth factors, microenvironment, and availability of substrates with different topography and rigidity[22], the orientation of the cells is an important property to achieve efficient differentiation while eliminating the potential variable side effects from external growth factors and inducers in the culture media. Calculation of the orientations of hMSC seeded on control and GAIN scaffolds was used with "ImageJ" software (version 1.50g, National Institute of Health, USA) and Orientation-J Distribution plug-in. Original microscope images (Fig. 5a) were converted into 8-bit colour images and the pixels/distance ratio was calibrated based on the microscope camera bar. The images were threshold first by HSV colour and then by brightness into binary images using Li algorithm (Fig. 5b). The orientation parameters were calculated with 5 pixel Gaussian window size and approximation with a cubic spline gradient. The resulting orientation texture maps are shown in Fig. 5c, and respective rotation angle span plots in Fig. 5d. Finally, these data were treated with SigmaPlot software (Systat GmbH, Germany) into polar form as shown in Fig. 2.

Immunological analysis. PBMCs from healthy donors were isolated using Ficoll-Paque gradient fractionation. In total $2 \cdot 10^6$ cells were used for each analysis. RNAs were extracted directly from scaffolds by TRIzol® (Ambion) reagent following 24 h cells growth on GAIN scaffold, according to the manufacturer's recommendations. cDNAs were synthesised from DNase-treated (Ambion) RNA by RevertAid Reverse Transcriptase (Thermo Fisher Scientific) with addition of RiboLock (Thermo Fisher Scientific) according to the manufacturer's recommendations. cDNA quality was verified by RT-PCR by using GAPDH primers and HOT FIREpol® Master Mix (Solis Biodyne, Estonia). RT-qPCR was performed in triplicates using EvaGreen qPCR mix plus no Rox (Solis Biodyne, Estonia) and the LightCycler® 480 Real-Time PCR System (Roche Applied Science). The fold of change was calculated relatively to the control (cells grown without scaffolds) after normalisation to GAPDH expression, using 2-$\Delta\Delta$Ct method (double difference of Ct). The values are respectively ΔCt = Ct(gene of interest) − Ct(GAPDH), and $\Delta\Delta$Ct = ΔCt(treated) − ΔCt(control). For visualization, the data were normalized to the cells grown without scaffold materials (control), converted to log scale and represented as a heat map (Fig. 4a; LionSolver 2.1, Reactive Search s.r.l., Italy). The represented data show values of two independent analyses normalized to the levels of cytokine expression for cells grown without GAIN scaffolds. Each tile is shaded on a colour scale to represent the value of the corresponding element of the data matrix. The rows of the data matrix are ordered such that similar rows are near each other, through hierarchical clustering using Euclidean distance (the distance between the two vectors in the feature space). The minimal mapping error is achieved by minimizing sum of coordinates normalized with respect to the maximum and minimum along each dimension (in this case, decimal logarithm of relative expressions).

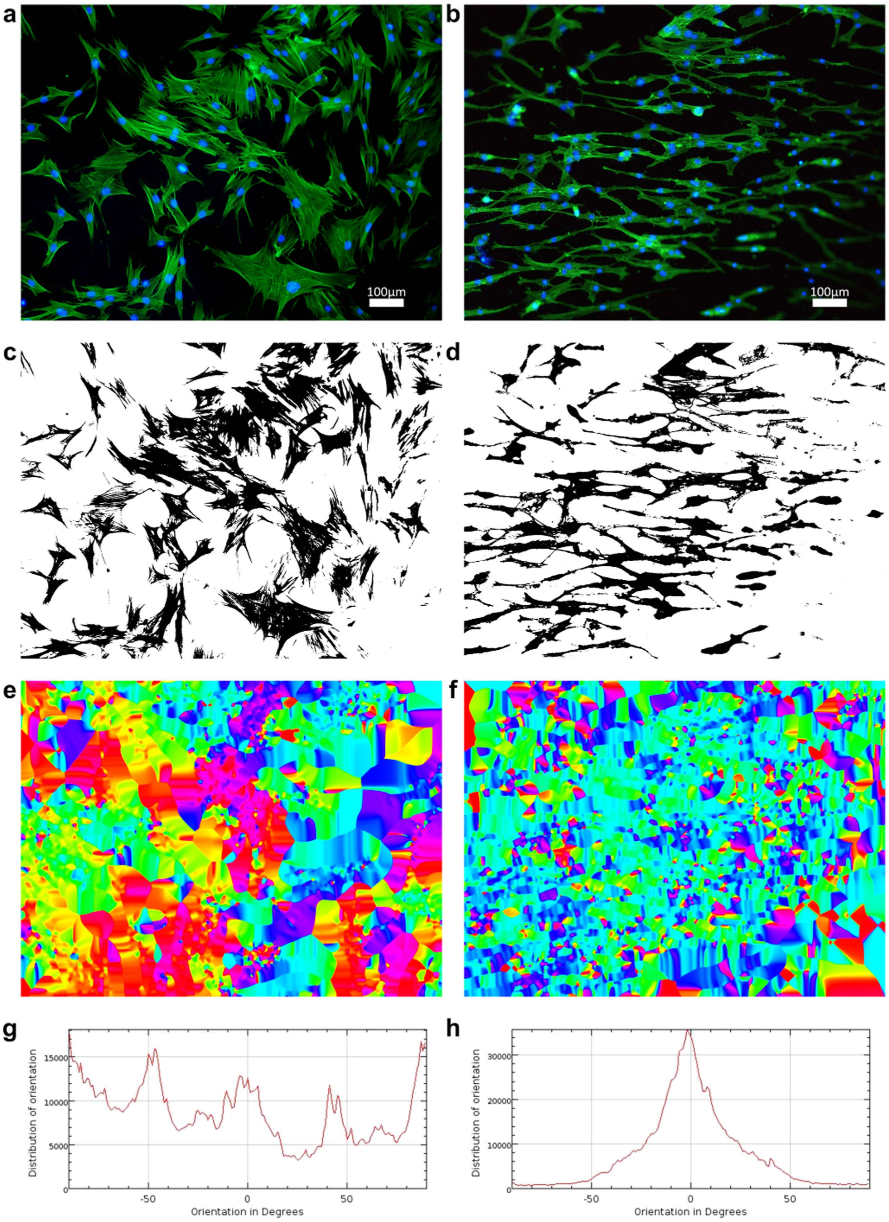

Figure 5. Original fluorescent microscopy pictures (**a**,**b**), processed binary images (**c**,**d**), orientation texture maps (**e**,**f**) with colour differences (rainbow spectrum from red to violet) indicate preferential orientation and these orientation distribution summaries (sum of distances in μm) plots (**g**,**h**) from −90 to 90° (clockwise). Images made on control (**a**,**c**,**e**,**g**) and horizontal GAIN (**b**,**d**,**f**,**h**) scaffolds.

Secretome ELISA analysis. Cell culture media was collected and soluble factors expression was analysed 24 h after initiation of cell culture. The levels of IL6, IL8/CXCL8, CCL2, IL1B, IL2, IL4, IL12, TNFα and IFNγ secreted into the growth medium were measured using Human IL-6 DuoSet ELISA Development Kit (R&D System, Wiesbaden, Germany), Human IL-8 Standard ABTS ELISA Development Kit (Peprotech, Rock Hill, NJ, USA), Human CCL2/MCP-1 DuoSet (R&D System), Human IL-1β/IL-1F2 DuoSet ELISA Development Kit (R&D System, Wiesbaden, Germany), Human IL-2 ELISA Development Kit (Peprotech, Rock Hill, NJ, USA), Human IL-4 Standard ABTS (PeproTech, Rock Hill, NJ, USA), Human IL-12 ELISA Development Kit (Peprotech, Rock Hill, NJ, USA), Human TNFα ELISA Development Kit (Peprotech, Rock Hill, NJ, USA), Human IFN-γ ELISA Development Kit (Peprotech, Rock Hill, NJ, USA), and Human Standard ABTS ELISA Development Kit (Peprotech), respectively. The ELISA analysis was performed using high binding ELISA plates (Greiner BioOne) at RT according to the manufacturer's instructions. Optical density was measured using photospectrometer Spectramax 340 PC (Molecular Devices) at the wavelength 450 nm.

The represented data show values of two independent analyses normalized to the levels of cytokine expression for cells grown without GAIN scaffolds.

Ethical issues. Use of all human biological materials for the study was approved by the ethical committee at the National Institute for Health Development, Tallinn, Estonia (permission No. 2234 from December 09, 2010). Written informed consent was obtained from all participants prior to the study. All experiments were performed in accordance with national relevant ethical guidelines and GLP regulations.

References

1. Lee, J., Cuddihy, M. J. & Kotov, N. A. Three-dimensional cell culture matrices: state of the art. *Tissue Eng Part B Rev* **14,** 61–86 (2008).
2. Bressan, E. *et al.* Graphene based scaffolds effects on stem cells commitment. *J Translational Med.* **12,** 296 (2014).
3. Jin, G. & Li, K. The electrically conductive scaffold as the skeleton of stem cell niche in regenerative medicine. *Mater. Sci. Eng. C* **45,** 671–681 (2014).
4. Smith, L.A. *et al.* Directed differentiation and neurite extension of mouse embryonic stem cell on aligned poly(lactide) nanofibers functionalized with YIGSR peptide. *Biomaterials* **34,** 9089–9095 (2013).
5. Talukdar, Y. *et al.* The effects of graphene nanostructures on mesenchymal stem cells. *Biomaterials* **35,** 4863–4877 (2014).
6. Zhang, Y., Nayak, T. R., Hong, H. & Cai, W. Graphene: a versatile nanoplatform for biomedical applications. *Nanoscale* **4,** 3833–3842 (2012).
7. Goenka, S., Sant, V. & Sant, S. Graphene-based nanomaterials for drug delivery and tissue engineering. *J Control Release* **173,** 75–88 (2014).
8. Lu, C.-H. *et al.* Using graphene to protect DNA from cleavage during cellular delivery. *Chem Commun* (*Camb*) **46,** 3116–3118 (2010).
9. Titov, A. V., Král, P. & Pearson, R. Sandwiched graphene–membrane superstructures. *ACS Nano* **4,** 229–234 (2010).
10. Sanchez, V. C., Jachak, A., Hurt, R. H. & Kane, A. B. Biological interactions of graphene-family nanomaterials: an interdisciplinary review. *Chem Res Toxicol* **25,** 15–34 (2012).
11. Li, Y. *et al.* Graphene microsheets enter cells through spontaneous membrane penetration at edge asperities and corner sites. *Proc Natl Acad Sci USA* **110,** 12295–12300 (2013).
12. Georgakilas, V. *et al.* Functionalization of graphene: covalent and non-covalent approaches, derivatives and applications. *Chem Rev* **112,** 6156–6214 (2012).
13. Yang, K., Chen, B. & Zhu, L. Graphene-coated materials using silica particles as a framework for highly efficient removal of aromatic pollutants in water. *Sci Rep* **5,** 11641 (2015).
14. Aghayan, M., Hussainova, I., Gasik, M., Kutuzov, M. & Friman, M. Coupled thermal analysis of novel alumina nanofibers with ultrahigh aspect ratio. *Thermochim Acta* **574,** 140–144 (2013).
15. Ivanov, R. *et al.* Graphene encapsulated oxide nanofibers as a novel type of nanofillers for electroconductive ceramics. *J. Europ Ceramic Soc*, **35,** 4017–4021 (2015).
16. Discher, D. E., Janmey, P. & Wang, Y.-L. Tissue cells feel and respond to the stiffness of their substrate. *Science* **310,** 1139–1143 (2005).
17. Saha, K. *et al.* Substrate modulus directs neural stem cell behavior. *Biophys J* **95,** 4426–4438 (2008).
18. Coulombe, P. A. & Wong, P. Cytoplasmic intermediate filaments revealed as dynamic and multipurpose scaffolds. *Nat Cell Biol* **6,** 699–706 (2004).
19. Kenny, P. A. *et al.* The morphologies of breast cancer cell lines in three-dimensional assays correlate with their profiles of gene expression. *Mol Oncol* **1,** 84–96 (2007).
20. Feng, S. *et al.* Expansion of breast cancer stem cells with fibrous scaffolds. *Integr Biol* (*Camb*) **5,** 768–777 (2013).
21. Kazantseva, J. *et al.* Alternative splicing targeting the hTAF4-TAFH domain of TAF4 represses proliferation and accelerates chondrogenic differentiation of human mesenchymal stem cells. *PLos One* **8(10),** e74799 (2013).
22. Griffin, M. F., Butler, P. E., Seifalian, A. M. & Kalaskar, D. M. Control of stem cell fate by engineering their micro and nanoenvironment. *World J Stem Cells* **7,** 37–50 (2015).

Acknowledgements

This research was supported by the Estonian Research Council under the personal research grant PUT1093 (I.H.) and a grant from PROTOTRON foundation (Estonia) under project ULTRINIA to Tallinn University of Technology. The authors acknowledge Ave Laas (CellIn Technologies LLC, Estonia) for assistance in performing ELISA tests.

Author Contributions

J.K., R.I., M.G., T.N. and I.H. have written the main manuscript text. R.I. and I.H. were preparing the GAIN scaffolds, J.K. and R.I. have performed cell analytics and images acquisition, M.G. has made image orientation and statistical data analysis. R.I. and M.G. have finalized manuscript figures. J.K. made also detailed description of the cell analytics methods. All authors have reviewed the manuscript.

Additional Information

Competing financial interests: The authors declare no competing financial interests.

How to cite this article: Kazantseva, J. *et al.* Graphene-augmented nanofiber scaffolds demonstrate new features in cells behaviour. *Sci. Rep.* **6**, 30150; doi: 10.1038/srep30150 (2016).

DISSERTATIONS DEFENDED AT TALLINN UNIVERSITY OF TECHNOLOGY ON *MECHANICAL ENGINEERING*

1. **Jakob Kübarsepp**. Steel-Bonded Hardmetals. 1992.

2. **Jakub Kõo**. Determination of Residual Stresses in Coatings &Coated Parts. 1994.

3. **Mart Tamre**. Tribocharacteristics of Journal Bearings Unlocated Axis. 1995.

4. **Paul Kallas**. Abrasive Erosion of Powder Materials. 1996.

5. **Jüri Pirso**. Titanium and Chromium Carbide Based Cermets. 1996.

6. **Heinrich Reshetnyak**. Hard Metals Serviceability in Sheet Metal Forming Operations. 1996.

7. **Arvi Kruusing**. Magnetic Microdevices and Their Fabrication methods. 1997.

8. **Roberto Carmona Davila**. Some Contributions to the Quality Control in Motor Car Industry. 1999.

9. **Harri Annuka**. Characterization and Application of TiC-Based Iron Alloys Bonded Cermets. 1999.

10. **Irina Hussainova**. Investigation of Particle-Wall Collision and Erosion Prediction. 1999.

11. **Edi Kulderknup**. Reliability and Uncertainty of Quality Measurement. 2000.

12. **Vitali Podgurski**. Laser Ablation and Thermal Evaporation of Thin Films and Structures. 2001.

13. **Igor Penkov**. Strength Investigation of Threaded Joints Under Static and Dynamic Loading. 2001.

14. **Martin Eerme**. Structural Modelling of Engineering Products and Realisation of Computer-Based Environment for Product Development. 2001.

15. **Toivo Tähemaa**. Assurance of Synergy and Competitive Dependability at Non-Safety-Critical Mechatronics Systems design. 2002.

16. **Jüri Resev**. Virtual Differential as Torque Distribution Control Unit in Automotive Propulsion Systems. 2002.

17. **Toomas Pihl**. Powder Coatings for Abrasive Wear. 2002.

18. **Sergei Letunovitš**. Tribology of Fine-Grained Cermets. 2003.

19. **Tatyana Karaulova**. Development of the Modelling Tool for the Analysis of the Production Process and its Entities for the SME. 2004.

20. **Grigori Nekrassov**. Development of an Intelligent Integrated Environment for Computer. 2004.

21. **Sergei Zimakov**. Novel Wear Resistant WC-Based Thermal Sprayed Coatings. 2004.

22. **Irina Preis**. Fatigue Performance and Mechanical Reliability of Cemented Carbides. 2004.

23. **Medhat Hussainov**. Effect of Solid Particles on Turbulence of Gas in Two-Phase Flows. 2005.

24. **Frid Kaljas**. Synergy-Based Approach to Design of the Interdisciplinary Systems. 2005.

25. **Dmitri Neshumayev**. Experimental and Numerical Investigation of Combined Heat Transfer Enhancement Technique in Gas-Heated Channels. 2005.

26. **Renno Veinthal**. Characterization and Modelling of Erosion Wear of Powder Composite Materials and Coatings. 2005.

27. **Sergei Tisler**. Deposition of Solid Particles from Aerosol Flow in Laminar Flat-Plate Boundary Layer. 2006.

28. **Tauno Otto**. Models for Monitoring of Technological Processes and Production Systems. 2006.

29. **Maksim Antonov**. Assessment of Cermets Performance in Aggressive Media. 2006.

30. **Tatjana Barashkova**. Research of the Effect of Correlation at the Measurement of Alternating Voltage. 2006.

31. **Jaan Kers**. Recycling of Composite Plastics. 2006.

32. **Raivo Sell**. Model Based Mechatronic Systems Modeling Methodology in Conceptual Design Stage. 2007.

33. **Hans Rämmal**. Experimental Methods for Sound Propagation Studies in Automotive Duct Systems. 2007.

34. **Meelis Pohlak**. Rapid Prototyping of Sheet Metal Components with Incremental Sheet Forming Technology. 2007.

35. **Priidu Peetsalu**. Microstructural Aspects of Thermal Sprayed WC-Co Coatings and Ni-Cr Coated Steels. 2007.

36. **Lauri Kollo**. Sinter/HIP Technology of TiC-Based Cermets. 2007.

37. **Andrei Dedov**. Assessment of Metal Condition and Remaining Life of In-service Power Plant Components Operating at High Temperature. 2007.

38. **Fjodor Sergejev**. Investigation of the Fatigue Mechanics Aspects of PM Hardmetals and Cermets. 2007.

39. **Eduard Ševtšenko**. Intelligent Decision Support System for the Network of Collaborative SME-s. 2007.

40. **Rünno Lumiste**. Networks and Innovation in Machinery and Electronics Industry and Enterprises (Estonian Case Studies). 2008.

41. **Kristo Karjust**. Integrated Product Development and Production Technology of Large Composite Plastic Products. 2008.

42. **Mart Saarna**. Fatigue Characteristics of PM Steels. 2008.

43. **Eduard Kimmari**. Exothermically Synthesized B_4C-Al Composites for Dry Sliding. 2008.

44. **Indrek Abiline**. Calibration Methods of Coating Thickness Gauges. 2008.

45. **Tiit Hindreus**. Synergy-Based Approach to Quality Assurance. 2009.

46. **Karl Raba**. Uncertainty Focused Product Improvement Models. 2009.

47. **Riho Tarbe**. Abrasive Impact Wear: Tester, Wear and Grindability Studies. 2009.

48. **Kristjan Juhani**. Reactive Sintered Chromium and Titanium Carbide-Based Cermets. 2009.

49. **Nadežda Dementjeva**. Energy Planning Model Analysis and Their Adaptability for Estonian Energy Sector. 2009.

50. **Igor Krupenski**. Numerical Simulation of Two-Phase Turbulent Flows in Ash Circulating Fluidized Bed. 2010.

51. **Aleksandr Hlebnikov**. The Analysis of Efficiency and Optimization of District Heating Networks in Estonia. 2010.

52. **Andres Petritšenko**. Vibration of Ladder Frames. 2010.

53. **Renee Joost**. Novel Methods for Hardmetal Production and Recycling. 2010.

54. **Andre Gregor**. Hard PVD Coatings for Tooling. 2010.

55. **Tõnu Roosaar**. Wear Performance of WC- and TiC-Based Ceramic-Metallic Composites. 2010.

56. **Alina Sivitski**. Sliding Wear of PVD Hard Coatings: Fatigue and Measurement Aspects. 2010.

57. **Sergei Kramanenko**. Fractal Approach for Multiple Project Management in Manufacturing Enterprises. 2010.

58. **Eduard Latõsov**. Model for the Analysis of Combined Heat and Power Production. 2011.

59. **Jürgen Riim**. Calibration Methods of Coating Thickness Standards. 2011.

60. **Andrei Surzhenkov**. Duplex Treatment of Steel Surface. 2011.

61. **Steffen Dahms**. Diffusion Welding of Different Materials. 2011.

62. **Birthe Matsi**. Research of Innovation Capasity Monitoring Methodology for Engineering Industry. 2011.

63. **Peeter Ross**. Data Sharing and Shared Workflow in Medical Imaging. 2011.

64. **Siim Link**. Reactivity of Woody and Herbaceous Biomass Chars. 2011.

65. **Kristjan Plamus**. The Impact of Oil Shale Calorific Value on CFB Boiler Thermal Efficiency and Environment. 2012.

66. **Aleksei Tšinjan**. Performance of Tool Materials in Blanking. 2012.

67. **Martinš Sarkans**. Synergy Deployment at Early Evaluation of Modularity of the Multi-Agent Production Systems. 2012.

68. **Sven Seiler**. Laboratory as a Service – A Holistic Framework for Remote and Virtual Labs. 2012.

69. **Tarmo Velsker**. Design Optimization of Steel and Glass Structures. 2012.

70. **Madis Tiik**. Access Rights and Organizational Management in Implementation of Estonian Electronic Health Record System. 2012.

71. **Marina Kostina**. Reliability Management of Manufacturing Processes in Machinery Enterprises. 2012.

72. **Robert Hudjakov**. Long-Range Navigation for Unmanned Off-Road Ground Vehicle. 2012.

73. **Arkadi Zikin**. Advanced Multiphase Tribo-Functional PTA Hardfacings. 2013.

74. **Alar Konist**. Environmental Aspects of Oil Shale Power Production. 2013.

75. **Inge Roos**. Methodology for Calculating CO_2 Emissions from Estonian Shale Oil Industry. 2013.

76. **Dmitri Shvarts**. Global 3D Map Merging Methods for Robot Navigation. 2013.

77. **Kaia Lõun**. Company's Strategy Based Formation of e-Workplace Performance in the Engineering Industry. 2013.

78. **Maido Hiiemaa**. Motion Planner for Skid-Steer Unmanned Ground Vehicle. 2013.

79. **Dmitri Goljandin**. Disintegrator Milling System Development and Milling Technologies of Different Materials. 2013.

80. **Dmitri Aleksandrov**. Light-Weight Multicopter Structural Design for Energy Saving. 2013.

81. **Henrik Herranen**. Design Optimization of Smart Composite Structures with Embedded Devices. 2014.

82. **Heiki Tiikoja**. Experimental Acoustic Characterization of Automotive Inlet and Exhaust System. 2014.

83. **Jelena Priss**. High Temperature Corrosion and Abrasive Wear of Boiler Steels. 2014.

84. **Aare Aruniit**. Thermoreactive Polymer Composite with High Particulate Filler Content. 2014.

85. **Dmitri Gornostajev**. Development of the Calculation Method for Barge Hull. 2014.

86. **Liina Lind**. Wear of PVD Coatings on Fineblanking Punches. 2014.

87. **Nikolai Voltšihhin**. Design and Technology of Oxides-Containing Ceramic-Based Composites. 2014.

88. **Aleksander Šablinski**. RANS Numerical Modelling of Turbulent Polydispersed Flows in CFB Freeboard. 2015.

89. **Tanel Aruväli**. Wireless Real-time Monitoring of Machining Processes. 2015.

90. **Andrei Bogatov**. Morphological Changes on Diamond and DLC Films During Sliding Wear. 2015.

91. **Raimo Kabral**. Aero-Acoustic Studies and Innovative Noise Control with Application to Modern Automotive Gas Exchange System. 2015.

92. **Jevgeni Sahno**. Dynamic Management Framework for Continuous Improvement of Production Processes. 2015.

93. **Ott Pabut**. Optimal Design of Slotless Permanent Magnet Generators. 2015.

94. **Merili Kukuškin**. Value Centric Business Development for Estonian Manufacturing Small and Medium Sized Enterprises. 2015.

95. **Kaimo Sonk**. Development of Additive Manufacturing Based on Functional Requirements. 2015.

96. **Marina Aghayan**. Functionalization of Alumina Nanofibers with Metal Oxides. 2016.

97. **Marek Jõeleht**. Titanium Carbide Cermet as Ballistic Protection Material. 2016.

98. **Heikki Sarjas**. Novel Synthesized and Milled Carbide-based Composite Powders for HVOF Spray. 2016.

99. **Klodian Dhoska**. Measurement Methods with 3D Coordinate Measuring Machine and Improved Characterization Setup for Detector Performance. 2016.

100. **Aleksei Snatkin**. Development and Optimisation of Production Monitoring System. 2016.

101. **Igor Poljantšikov**. Partners Selection Tool for Virtual Enterprise in SMEs Network. 2016.

102. **Sergei Žigailov**. Experimental and Analytical Modelling of Pelvic Motion. 2016.

103. **Rommi Källo**. Synergy-Based Chaos Control in the Multi-Agent Hierarchical Systems. 2016.

104. **Der-Liang Yung**. ZrC-based and ZrC-doped Composites for High-Temperature and Wear Applications. 2016.

105. **Viive Pille**. Development of a Model for the Prevention of Work-Related Musculoskeletal Disorders in the Upper Extremities. 2016.

106. **Agus Pramono**. Investigation of Severe Plastic Deformation Processes for Aluminum Based Composites. 2016.

107. **Zorjana Mural**. Technology and Properties of Fine-grained Nd-Fe-B Magnets. 2017.

108. **Eero Väljaots**. Energy Efficiency Evaluation Method for Mobile Robot Platform Design. 2017.

109. **Viktoria Baškite**. Decision-Making Tool Development for Used Industrial Equipment Life Cycle Evaluation and Improvement. 2017.